KILOMETER-SPACED GNSS ARRAY FOR IONOSPHERIC IRREGULARITY MONITORING

BY

YANG SU

Submitted in partial fulfillment of the
requirements for the degree of
Doctor of Philosophy in Mechanical and Aerospace Engineering
in the Graduate College of the
Illinois Institute of Technology

Approved 
Advisor

Chicago, Illinois
May 2017

ACKNOWLEDGMENT

This dissertation could not have been written without Dr. Seebany Datta-Barua who not only served as my research adviser but also encouraged and challenged me throughout my academic program. Thanks to committee members Dr. Boris Pervan, Dr. Sudhakar Nair, Dr. Geoffrey Williamson for their precious time on the review of my dissertation. Thanks to Armour College of Engineering and to Daniel, Uriel, Roohollah and Ningchao at Space Weather Lab for their constructive academic and research support. Special thanks to my parents and my girlfriend for making this effort possible.

I would like to thank in particular Dr. Gary Bust of JHUAPL for leading the proposal and project that got this research started and for invaluable theoretical guidance. Thanks to Dr. Kshitija Deshpande of Embry–Riddle Aeronautical University for providing high-rate GPS data post-processing routines. Thanks to Dr. Emanoel Costa for helpful technical discussions. Thanks to Dr. Geoffrey Crowley of ASTRA for technical support with the receivers, and for providing supplementary data from another CASES receiver on-site. Thanks to Dr. Michael Nicolls, Dr. Stephen Kaeppler and Dr. Roger Varney of SRI for PFISR data made available. Thanks to Dr. Donald Hampton of University of Alaska at Fairbanks for on-site technical assistance and all-sky camera data. Thanks to Dr. Cesar Valladares of UT Dallas for proving equatorial GPS data and to Dr. Marco Milla and Dr. Danny Scipion of JRO for discussions on radar instruments. Geomagnetic index data are available from the World Data Center for Geomagnetism and the Space Weather Prediction Center.

This work is supported by National Science Foundation under grants No. AGS-1261369. Any opinions, findings, and conclusions or recommendations expressed in this material are those of the author(s) and do not necessarily reflect the views of NSF.

TABLE OF CONTENTS

Page

ACKNOWLEDGEMENT iii

LIST OF TABLES vi

LIST OF FIGURES xi

LIST OF SYMBOLS xii

ABSTRACT xv

CHAPTER

1. INTRODUCTION 1

   1.1. Ionosphere 1
   1.2. Previous Work 3
   1.3. Contributions 7

2. IONOSPHERIC SCINTILLATION AND IRREGULARITIES . . 10

   2.1. Ionospheric Irregularities 10
   2.2. Jicamarca Radio Observatory 12
   2.3. Poker Flat Research Range Instruments 14
   2.4. Scintillation Auroral GPS Array 17
   2.5. Challenges 22
   2.6. Summary 23

3. AUTOMATED SCINTILLATION MONITORING 27

   3.1. Scintillation Statistics Survey 27
   3.2. Automated Scintillation Detection Routine 30
   3.3. Scintillation Events Discussed in This Dissertation 36
   3.4. Summary 38

4. ESTIMATION OF PLASMA DRIFTS AND ANISOTROPY . . 41

   4.1. One-Dimensional Spaced Receiver Technique 43
   4.2. Application of One-Dimensional Case 47
   4.3. Two-Dimensional Spaced Receiver Technique 49
   4.4. Application to Single-Satellite Event B1,B2 54
   4.5. Automated Drift and Anisotropy Estimation 59

4.6. Summary 60

5. ERROR ANALYSIS OF IRREGULARITY ESTIMATES 63

5.1. Error Analysis of SAGA Estimates 63
5.2. Application to Single-Satellite Event A2 68
5.3. Application to Single-Satellite Event A1 73
5.4. Application to Single-Satellite Event B1 76
5.5. Summary 77

6. MULTI-INSTRUMENT STUDY OF THE IONOSPHERE . . . 82

6.1. Propagation of PFISR Uncertainties 82
6.2. Application to Multi-Satellite Event A3 85
6.3. Application to Multi-Satellite Event C1 91
6.4. Summary 94

7. CONCLUSION 95

7.1. Summary and Discussions 95
7.2. Future Work 97

APPENDIX 100

A. DERIVATION OF SATELLITE MOTION 100

BIBLIOGRAPHY 102

LIST OF TABLES

Table Page

3.1 Top 10 active days of year (DOY) from December 2013 to 2014 sorted chronologically (day 342 is in 2013). K_p measures the global geomagnetic activity. AE measures the auroral geomagnetic activity. . . . 35

3.2 Scintillation periods generated and sorted by the average σ_Φ in rad with start time t_0 and end time t_f, duration Δt,and average number of samples/receiver. 37

3.3 Multi-satellite scintillation periods generated and sorted by start time t_0, end time t_f and number of simultaneously scintillating satellites. 40

3.4 Events to be examined in this dissertation. 40

4.1 Top 20 active days December 2013 to December 2014, and SAGA estimates of horizontal drift velocity, characteristic velocity, and correlation ellipse shape and orientation. For each day, only the PRN with most significant scintillation is shown. 61

5.1 ϵ_n for PRN23 during event A1 : 0343-0417 UT on December 8, 2013 with $0 < v_c < v, v_c \in \mathbb{R}$ 75

5.2 ϵ_n for PRN29 during event B1 : 1120-1157 UT on February 20, 2014 with $0 < v_c < v, v_c \in \mathbb{R}$ 76

6.1 ϵ_{pn} during events A3, B1 and C1 84

6.2 ϵ_{sn} with $0 < v_c < v, v_c \in \mathbb{R}$, compared to 66 ° N, for event A3. . . . 91

6.3 ϵ_{sn} with $0 < v_c < v, v_c \in \mathbb{R}$, compared to 66 ° N, for event C1. . . . 94

LIST OF FIGURES

Figure Page

1.1 A signal transmitted from a satellite and received on the ground undergoes amplitude and phase shift as it passes through irregularities in the ionosphere. 2

1.2 Correlation among three received signals originating from the same satellite. 5

2.1 (a) Ionospheric irregularities, adapted from [37] and (b) scintillation occurrences observed at different latitudes, taken from [38]. 11

2.2 (a)Earth's magnetic field lines at various latitudes, taken from[39]. Declination angle is defined as that from geographic north to magnetic north. Inclination, or dip, angle is defined as that from the horizontal plane to the field line, positive in the northern hemisphere. (b)Gyration and $E \times B$ drift motion of a positively charged particle caused by the Earth's electromagnetic field, adapted from [40]. 12

2.3 Trihourly Kp bar plots over the course of 3 days. Values in red indicate severe disturbances in the geomagnetic field. Values in green or yellow suggest quiet periods or minor disturbance. Courtesy of Space Weather Prediction Center [41]. 13

2.4 Auroral electrojet during a geomagnetic storm, derived from the difference of the upper limit AU and the lower limit AL. Courtesy of World Data Center for Geomagnetism, Kyoto [42]. 14

2.5 The radar array at Jicamarca Radio Observatory, Peru at 11.95° S, 76.87° W with inclination 1.145° and declination 0.367°. The magnetic field line is nearly horizontal. The receiver pair O,E is also shown as tiny red pins, whose baseline points in the geomagnetic east-west direction nearly parallel to the local field line in white. Courtesy of Google Maps. 15

2.6 Color scaled S_4 time series as trajectories of all visible GPS satellites in the sky. Concentric circles indicate contours of satellite elevations while spokes indicate satellite azimuths. 16

2.7 A daily observation of night time ESF by JULIA. Signal-to-noise of the radar echoes as a function of range depicts the developing shape of the structure over local time. Adapted from Jicarma Radio Observatory database [43]. 17

2.8 Sky plot of PFISR beams represented by blue dots. Spokes represents azimuth angle of the beams while concentric circles indicates elevation angles. The closed shape in black indicates radar sky coverage. Taken from SRI International ISR Database [44]. 18

2.9 Map of scintillation aurora GPS array (SAGA) location (courtesy of Google Maps). Annotations show true north (TN) and magnetic north (MN). The declination angle (between TN and MN) $\approx 23.5°$ and the inclination angle $\approx 77.5°$. Courtesy of Google Maps. . . . 19

2.10 Scintillation auroral GPS array (SAGA) architecture. 21

2.11 S_4 measurements by receiver from SAGA. 22

2.12 σ_ϕ measurements by receiver from SAGA. 23

2.13 σ_ϕ measurements by satellite from SAGA. 24

2.14 Estimated data size for SAGA data of different lengths and in different formats. 25

2.15 A scintillation event with intense phase/power variations during a geomagnetic storm. Signal (a)power and (b) phase are possessed, filtered from 100Hz IQ data for color-coded SAGA receivers. . . . 26

2.16 Contribution road map. 26

3.1 Seasonal distribution of phase scintillation index σ_Φ throughout year 2014. 28

3.2 Daily distribution of phase scintillation index σ_Φ through year 2014 with solar terminators. 29

3.3 Daily occurrences of amplitude scintillation events recorded by the receiver pair. Histogram in white represents weak scintillation while histogram in black for moderate scintillation. 31

3.4 Hourly occurrences of amplitude scintillation events recorded by the receiver pair. Histogram in white represents weak scintillation while histogram in black for moderate scintillation. 32

3.5 Flowchart for automated scintillation detection routine. 33

3.6 σ_ϕ measurements by receiver from SAGA. Grey lines indicate triggers th_{dyn} and th_{stat}. 34

3.7 The method to distinguish continuous scintillation times for each receiver and identify common time intervals across receivers. For example, there are scintillation discontinuities for receiver 1 during $(t_{1,1}, t_{2,1})$ and $(t_{3,1}, t_{4,1})$ since 2 or more σ_Φ values stay below the threshold consecutively within these intervals. 36

3.8 Detected multi-satellite events for 12/08/2013. 38

3.9 Detected multi-satellite events for 03/17/2015. 39

4.1 A radio signal transmitted from a satellite arrives at the ionosphere as a plane wave (arriving from zenith in this illustration). Due to the random sizes and distributions of irregularities, the plane wave emerges from the scattering layer as a distorted wave front. However, it is spatially and temporally correlated, having originated as a plane wave, and passed through a random scattering medium. These correlations are detectable by multiple receivers on the ground. 42

4.2 Ellipses of constant levels of $R(x, \tau)$ with $R(0, 0) = 1$. ρ_{ii}, the auto-correlation curve, is the intersection of R with $x = 0$. ρ_{ij}, the cross-correlation curve for receivers i and j separated by distance ξ_c, is the intersection of R with $x = \xi_c$. Both ρ_{ii}, ρ_{ij} are slices of R that intersect the ellipse $R = \rho_m$, the cross-correlation maximum. . 45

4.3 A projected view of Figure 4.2 along x-axis. In practice, $\rho_{ii}, \rho_{jj}, \rho_{ij}$ are normalized by the same factor $\sqrt{\max(\rho_{ii}) \max(\rho_{jj})}$ to ensure that $\rho_{ii}(0) = R(0, 0) = 1$. $\rho_{ij} = \rho_{ii} = \rho_m$ gives time delays τ_{cm}, τ_{am}. 46

4.4 A projected view of Figure 4.2 along R axis. Only $R = \rho_m$ is shown. 47

4.5 Top: 46 s time series of 50 Hz processed and filtered signal power for receiver pair E (blue) and O (red). Bottom: cross-correlation of the two signals in red. Auto-correlation of E is also plotted in cyan for reference. Note that the correlations are normalized to ensure $R\{\mathbf{0}\} = 1$. 48

4.6 Ellipsoid in 2D space and time. The ellipsoid represents a surface of constant correlation value. 50

4.7 The projection of several ellipsoids, each corresponding to a different correlation value, onto the spatial dimensions gives concentric ellipses of constant correlation. The ellipses all have same axial ratio AR and orientation Ψ_a. 51

4.8 Cross-correlation ρ_{ij} and auto-correlation ρ_{ii} and corresponding time delays τ_c, τ_a at a given value $\rho_c = \rho_{ij}(\tau_c) = \rho_{ii}(\tau_a)$. 53

4.9 100 Hz detrended and filtered (a) power and (b) phase for PRN 29 during 1120-1157 UT, 20 Feb 2014 (event B1). Signal data from operational receivers are color scaled according to Figure 2.9. . . . 55

4.10 100 Hz detrended and filtered (a) power and (b) phase for PRN 29 during 2685-2729 s after 1100UT, 20 Feb 2014 (event B2) 56

4.11 Pairwise cross-correlations in phase from PRN 29 during 2685-2729 s after 1100 UT, 20 Feb 2014 (event B2). 57

4.12 SAGA estimates as function of ρ_{cutoff} for event B2. 58

5.1 Measurements of σ_ϕ from the array of 5 operational SAGA receivers, organized by satellite number, vs. UT hour on 8 December 2013. . 68

5.2 Original and noise-added phase observations during 2615-2660 s after 0300 UT, 8 Dec 2013. 69

5.3 Pairwise cross-correlations ρ_{ij} in phase from PRN 23 during event A2, 2615-2660 s after 0300 UT, 8 Dec 2013. 70

5.4 Map of active SAGA locations and example ellipses with the estimated $AR = 2.78$ and $\Psi_a = 34.51°$, assuming the functional form of R in Eq. (4.10) were a 2D Gaussian, for illustrative purposes. . 71

5.5 Obtaining $\tilde{\tau_a}, \tau_c$ with $\tilde{\rho}_{ij} \approx \tilde{\rho}_{ii}$. 72

5.6 Observation array $\mathbf{y}$ defined in Eq. (4.24) based on the original phase data (black) and 1000 simulations $\tilde{\mathbf{Y}}$ of noise-added phase data (green). 73

5.7 Simulated random noise ν on observation array $\mathbf{y}$ using Monte Carlo method. 74

5.8 Estimates vs time as measured by SAGA from PRN 23 for $T = 30$ s., after subtracting off satellite motion. Light magenta points satisfy $v_c/v < 1, v_c \in \mathbb{R}$, and dark magenta estimates do not. 78

5.9 Estimates vs time as measured by SAGA from PRN 23 for $T = 10$ s, after subtracting off satellite motion. Light magenta points satisfy $v_c/v < 1, v_c \in \mathbb{R}$, and dark magenta estimates do not. 79

5.10 Estimates vs time as measured by SAGA from PRN 29 for $T = 30$ s., after subtracting off satellite motion. Light magenta points satisfy $v_c/v < 1, v_c \in \mathbb{R}$, and dark magenta estimates do not. 80

5.11 Estimates vs time as measured by SAGA from PRN 29 for $T = 10$ s., after subtracting off satellite motion. Light magenta points satisfy $v_c/v < 1, v_c \in \mathbb{R}$, and dark magenta estimates do not. 81

6.1 100 Hz detrended and filtered power phase for (a) PRN 10 at 0403-0417 UT on 8 Dec 2013. 85

6.2 100 Hz detrended and filtered power phase for (b) PRN 13 at 0403-0417 UT on 8 Dec 2013. 86

6.3 100 Hz detrended and filtered power phase for (c) PRN 23 at 0403-0417 UT on 8 Dec 2013. 87

6.4 Skyplot of satellite locations and PFISR radar beams (cyan) at 0403–0417 UT for PRNs 10, 13, and 23. 88

6.5 Estimates of drift speed and direction vs time as measured by signals from PRNs 10, 13, and 23, after subtracting off satellite motion. Estimates are made over periods longer than $T = 30$ s. Each color curve corresponds to one PRN. PFISR measurements during this interval are also shown. 90

6.6 Estimates of drift speed and direction vs time as measured by signals from PRNs 18, 22, and 27, after subtracting off satellite motion. Estimates are made over periods longer than $T = 30$ s. Each color curve corresponds to one PRN. PFISR measurements during this interval are also shown. 92

6.7 Sky plot of PFISR beams and GPS PRN 18 & 22 & 27 location during 1300-1330 UT, March 17 2015. 93

A.1 Satellite motion related to the ground measured at the ionospheric pierce point (IPP) also contributes to the irregularity drift of the ground pattern. 102

LIST OF SYMBOLS

Symbol	Definition
AE	Auroral Electrojet index
AR	axial ratio of the ellipse
$\mathbf{D}$	differencing matrix
$\mathbf{G}$	element selection matrix
$\mathbf{H}$	mapping matrix
I, Q	in-phase and quadrature-phase signal component
$\mathbf{J}$	Jacobian
K_p	Planetary-K index
L	thickness of the irregularity layer
N_{stat}/N_{dyn}	average number of data points exceeding the thresholds for each operational receiver
P_f	post-processed signal power
R	decreasing function
S_4	amplitude scintillation index
SI	signal intensity
T	length of time interval
$\mathbf{W}$	weighting matrix
WSN	weighted scintillation number
$\tilde{\mathbf{X}}$	noisy state array
$\tilde{\mathbf{Y}}$	observation matrix for all ensembles
$\hat{\mathbf{Y}}$	valid observation matrix

a, b, h, f, g, c	quadratic parameters
d_F	Fresnel scale
f_c	cut-off frequency for post-processing
k	decorrelation in time
$s_i(t), s_j(t)$	received trans-ionospheric signals
$\tilde{s}_i(t), \tilde{s}_j(t)$	noisy signals
$t_0, t_f, \Delta t$	start time, end time and duration of a scintillation event
th_{stat}/th_{dyn}	static/dynamic threshold value
v'	apparent drift speed of the diffraction pattern
v	true drift speed of the diffraction pattern
v_c	characteristic velocity of the drift pattern
$w(t)$	simulated white Gaussian noise
x	one-dimensional separation of a receiver pair
x_{ij}, y_{ij}	two-dimensional separation of a receiver pair
$\mathbf{x}$	state vector
$\hat{\mathbf{x}}$	valid state vector
$\mathbf{y}$	observation array
z	height of the irregularity layer
z_p, σ_p	any of the PFISR drift estimates and its error
z_s, σ_s	any of the SAGA estimates and its error
ϵ_n	normalized root-mean-squared variations of any of the SAGA estimates over a certain period

ϵ_{pn}	normalized root mean squared variations of PFISR drift estimates over a certain period
ϵ_{sn}	normalized root mean squared errors on SAGA drift estimates compared to PFISR
Φ_f	post-processed signal phase
$\lambda_{ipp}, \phi_{ipp}$	latitude, longitude of the ionospheric pierce point
λ	signal wavelength
ν	observation error
$\rho_{ij}(\tau), \rho_{ii}(\tau)$	cross-correlation/auto-correlation of receiver signals
ρ_{cutoff}	cross-correlation cut-off
Ψ_a	orientation angle of the semi-major axis of the ellipse
σ_Φ	phase scintillation index
σ_v, σ_θ	uncertainties in drift speed and direction
τ	time difference between two observations
θ	true drift orientation angle of the diffraction pattern

ABSTRACT

This dissertation presents automated, systematic data collection, processing, and analysis methods for studying the spatial-temporal properties of Global Navigation Satellite Systems (GNSS) scintillations produced by ionospheric irregularities at high latitudes using a closely spaced multi-receiver array deployed in the northern auroral zone. The main contributions include 1) automated scintillation monitoring, 2) estimation of drift and anisotropy of the irregularities, 3) error analysis of the drift estimates, and 4) multi-instrument study of the ionosphere.

A radio wave propagating through the ionosphere, consisting of ionized plasma, may suffer from rapid signal amplitude and/or phase fluctuations known as scintillation. Caused by non-uniform structures in the ionosphere, intense scintillation can lead to GNSS navigation and high-frequency (HF) communication failures. With specialized GNSS receivers, scintillation can be studied to better understand the structure and dynamics of the ionospheric irregularities, which can be parameterized by altitude, drift motion, anisotropy of the shape, horizontal spatial extent and their time evolution. To study the structuring and motion of ionospheric irregularities at the sub-kilometer scale sizes that produce L-band scintillations, a closely-spaced GNSS array has been established in the auroral zone at Poker Flat Research Range, Alaska to investigate high latitude scintillation and irregularities. Routinely collecting low-rate scintillation statistics, the array database also provides 100 Hz power and phase data for each channel at L1/L2C frequency.

In this work, a survey of seasonal and hourly dependence of L1 scintillation events over the course of a year is discussed. To efficiently and systematically study scintillation events, an automated low-rate scintillation detection routine is established and performed for each day by screening the phase scintillation index. The spaced-receiver technique is applied to cross-correlated phase and power measure-

ments from GNSS receivers. Results of horizontal drift velocities and anisotropy ellipses derived from the parameters are shown for several detected events. Results show the possibility of routinely quantifying ionospheric irregularities by drifts and anisotropy. Error analysis on estimated properties is performed to further evaluate the estimation quality. Uncertainties are quantified by ensemble simulation of noise on the phase signals carried through to the observations of the spaced-receiver linear system. These covariances are then propagated through to uncertainties on drifts. A case study of a single scintillating satellite observed by the array is used to demonstrate the uncertainty estimation process. The distributed array is used in coordination with other measuring techniques such as incoherent scatter radar and optical all-sky imagers. These scintillations are correlated with auroral activity, based on all-sky camera images. Measurements and uncertainty estimates made over a 30-minute period are made and compared to a collocated incoherent scatter radar, and show good agreement in horizontal drift speed and direction during periods of scintillation for cases when the characteristic velocity is less than the drift velocity. The methods demonstrated are extensible to other zones and other GNSS arrays of varying size, number, ground distribution, and transmitter frequency.

CHAPTER 1

INTRODUCTION

1.1 Ionosphere

The ionosphere is a region in the upper atmosphere ionized by solar UV radiation. A radio wave propagating through the ionosphere may suffer from rapid signal fluctuations known as scintillation, illustrated in Figure 1.1. Scintillation is one of the early identified effects of space weather on Global Positioning System (GPS) signals [1]. Its severity is measured by the standard deviation of received signal power and phase over a finite time interval. At low latitudes scintillation is mainly associated with equatorial bubbles known as spread F [2], while at high latitudes it has often been correlated with aurora [3]. Not only varying with latitude, scintillation effects are related to frequency of the transmitted signal, time of day, season, geomagnetic and solar activity [4]. Intense scintillation can cause signal fading or loss of lock, making it difficult for ground users to track Global Navigation Satellite System (GNSS) signals. During severe scintillation, GNSS augmentation systems for aircraft navigation can have reduced continuity of service, i.e., a disruption to the navigation service after an aircraft has initiated a maneuver (e.g., approach and landing) [5]. Scintillation can degrade or interrupt communications operations as well [6].

Ionospheric scintillations are produced by non-uniform plasma density variations in the ionosphere known as irregularities.These irregular structures can be characterized by their scale size, drift velocity, thickness, top altitude and anisotropy in their shape. At high latitudes magnetic field lines connect the ionosphere to the magnetosphere (magnetic-field-dominated plasma above) and the thermosphere (neutral particles intermingled with the ionosphere). Ionospheric plasma transport is governed

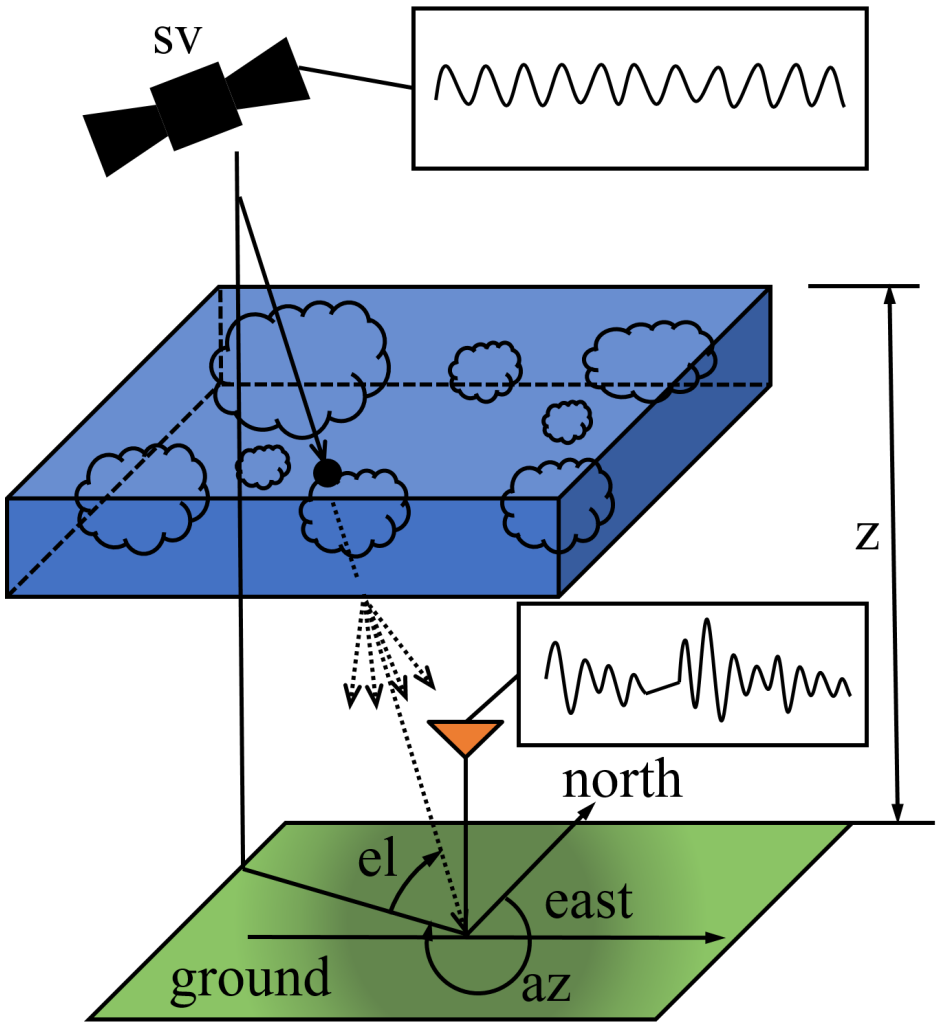

Figure 1.1. A signal transmitted from a satellite and received on the ground undergoes amplitude and phase shift as it passes through irregularities in the ionosphere.

by both electrodynamics and neutral wind interactions. Ionospheric motion can also be affected by turbulence and energy input. At high latitudes these energy inputs give rise to ionospheric irregularities at a range of scale sizes. The irregularities may be transported at a drift velocity that is primarily horizontal given the orientation of the electric and magnetic fields. They may be elongated in one horizontal direction due to field line geometry as well. At the same time irregularities are forming and

dissolving, and this is parameterized by a characteristic velocity.

1.2 Previous Work

1.2.1 Existing Instruments. Different types of measuring instruments have been established at various latitudes to probe the ionosphere, including rocket sounding and satellites that directly measure the ionosphere [7] and backscatter radars consisting a large array of antennas [8]. Here, previously existing radar systems and GNSS networks are summarized.

Known for scientific sounding rocket launches, the Poker Flat Research Range, Alaska offers an auroral zone location and an impressive clustering of scientific instruments that operate stand-alone and in support of sounding experiments, including the advanced modular incoherent scatter radar (AMISR), and optical all-sky imaging cameras. Consisting of a large array of antennas with electronic steering ability, the AMISR at Poker Flat (PFISR) system operates at 450-550 MHz and probes the dynamics and structuring of the auroral and sub-auroral ionosphere near the magnetic zenith. PFISR provides a variety of ionospheric measurements including ion drift velocities and temperature of charged particles.

Jicamarca Radio Observatory near Lima, Peru is one of the largest ionospheric research sites in the equatorial region. Among the variety of large-scale scientific instruments, JULIA is a 50 MHz coherent scatter radar designed to observe equatorial plasma irregularities and neutral atmospheric waves for extended periods of time. JULIA can operate unsupervised for long intervals as it does not use the main high-power transmitters, which are expensive and labor-intensive to operate and maintain. It is uniquely suited for studying the day-to-day and long-term variability of equatorial irregularities. JULIA provides daily east-west field aligned drift measurements at various altitudes from 90 to 900 km.

Large-scale scientific instruments like JULIA or AMISR are either fixed, expensive, or require extensive maintenance. Recently, constellations of GNSS have greatly advanced measurement techniques for the physics of the geophysical environment. Worldwide publicly available GNSS receivers number in the thousands, enabled by low cost due to chip set manufacturing scalability. Organizations such as International GNSS Service (IGS) provide a data network publicly available with inter-receiver spacing as little as a few kilometers in certain regions. For example, such dual-frequency arrays are used for mapping column-integrated plasma density, or total electron content (TEC), over continent-wide scales [9].

1.2.2 Scintillation theory. Scintillation theories and climatological /global models based on wave propagation theories have been established to quantify scintillation and irregularities over the past few decades[10, 11, 12, 13, 14, 15]. Recent studies have included characterizing the scintillations statistics to evaluate their effects on navigation tracking performace [16, 17, 18], relating scintillations to the occurrence of energetic particle precipitation [19, 20], large scale geomagnetic storms [21, 22], the formation of equatorial bubbles [2] , polar cap patches [23, 24], and auroral arcs [3] to better understand the dynamics and structuring of ionospheric irregularities. Most of the studies focus only on particular cases of scintillation due to solar/geomagnetic storms after these events are reported. Routine monitoring of these events is still uncommon.

Trans-ionospheric radio signals have been used to sense plasma motion. One of the sensing methods is the spaced-receiver technique. Well established in the literature [25], it leverages the idea that a pair of closely spaced antennas receiving transmitted signals that interact with the same moving medium (the ionosphere) will receive radio signals that display similar structures with time displacement dependent on the baseline between the receivers and ionospheric drift component along the

baseline [26]. The theory implies that signals received at different ground receivers shown in Figure 1.2 from the same source (satellite) are both temporally and spatially correlated. The correlation is associated with the drifting and changing diffraction pattern of irregularities on the ground.

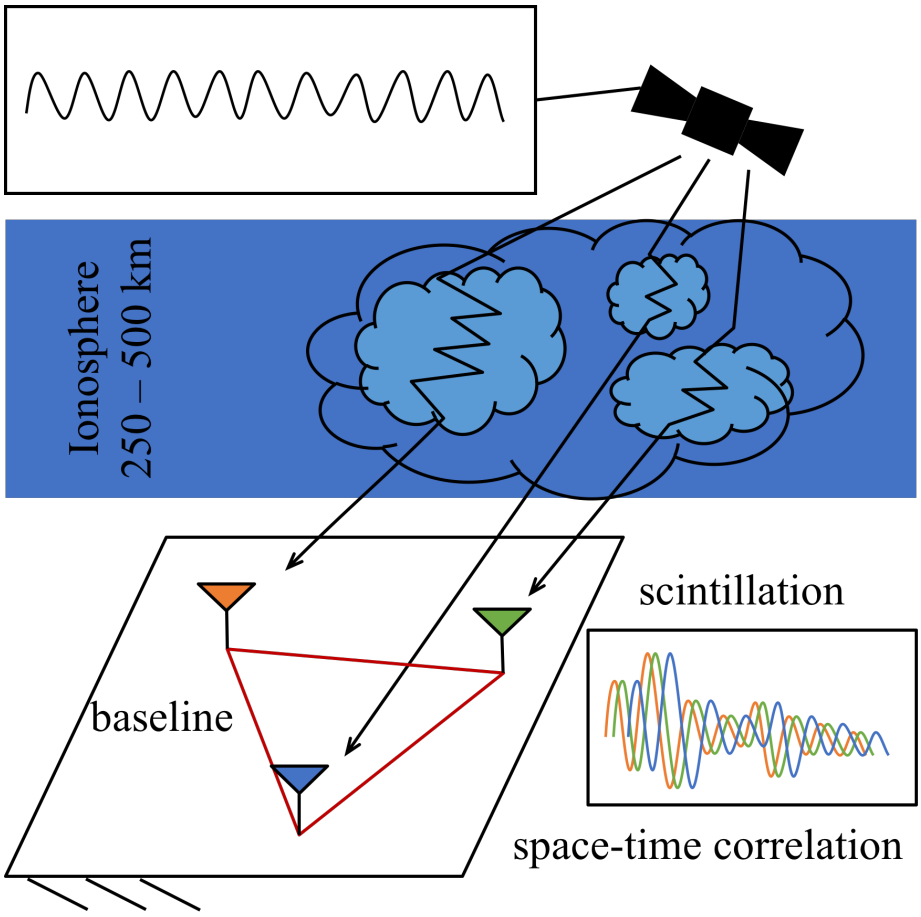

Figure 1.2. Correlation among three received signals originating from the same satellite.

Several high-latitude ionospheric studies have been done in the past to understand the diffraction pattern of ionospheric irregularities. The morphology of the ionosphere was studied in [27] by applying the correlation technique proposed by [28] to a set of spaced-receiver wideband measurements made at the Poker Flat auroral zone. This algorithm was reviewed in [29] with an approach generalized from [30] using different satellite signals. The former considers only the time delays for the

maxima and crossings of the correlation functions. It was first applied to VHF (∼30 to ∼300 MHz) observations for examining the plasma structure and dynamics of the polar cap with [31]. They demonstrated the use with geostationary satellites at high latitudes. The evolution of sub-kilometer scale irregularities created by a high frequency beam was discussed in [32] using the latter method. Recent studies developed different interpretations of the cross-correlation function [33] [34].

However, some of these studies used VHF beacon satellite transmissions. The scale sizes of the irregularities are determined by the Fresnel scale d_F of the radio signal in Eq 1.1, where λ is the wavelength and z the vertical distance from the irregularity layer to the antenna. Therefore VHF signals are diffractively sensitive to irregularities that are larger than those affecting GNSS wavelengths ($\lambda_{L1} \approx 19.0$ cm, $\lambda_{L2} \approx 24.4$ cm).

$$d_F = \sqrt{\lambda z} \tag{1.1}$$

Another difference between GNSS and the past VHF studies is that the GNSS satellite is moving with respect to the ground, and the irregularities may be also. This relative motion must be taken into account. Furthermore, to our knowledge, none of the existing GNSS closely-spaced receiver arrays are currently operating routinely for scintillation monitoring.

Many other previous studies of high latitude scintillation at GNSS frequencies were carried out using a single scintillation receiver or arrays of receivers separated by hundreds of kilometers [19]. At 100 km or even 10 km distances, one may examine TEC variations due to structures of comparable ∼100 km size, to try to estimate horizontal drift speeds. However, there is no guarantee that receivers this far apart necessarily observe the same sub-km scale irregularity. With baselines much larger than the scale size of the irregularity, there is not a way to sense plasma motion from the phase fluctuations.

In order to investigate the two-dimensional (2D) structuring of ionospheric irregularities at kilometer scales in detail, a closely-clustered 2D array of GNSS scintillation receivers is required. When the array is spaced at the scale sizes comparable to the irregularities that produce scintillations at GNSS L-band frequencies, i.e., from the Fresnel scale ($d_F \approx$ 100-300 meters) up to a few kilometers, the 2D array acts as a single spatially distributed instrument sensitive to the spatial and temporal structuring of the 2D phase pattern received on the ground due to ionospheric irregularities at those scale sizes. [2] set up such an array of GPS receivers at low latitudes to analyze equatorial anomaly scintillations. More recently, [35] placed an array at Gakona, Alaska, to sense irregularities with multi-band signals, but the methods used differ from the spaced receiver theory. A suitably spaced distributed array can also be used in coordination with other measuring techniques such as incoherent scatter radar and optical all-sky imagers, allowing for multi-instrument studies of irregularities at different scale sizes.

1.3 Contributions

This dissertation proposes a system of automated data collection, processing, and analysis methods for studying the spatial-temporal properties of Global Navigation Satellite Systems (GNSS) scintillations produced by ionospheric irregularities, demonstrated at high latitudes using a closely-clustered GPS receiver array in the northern auroral zone.

Chapter 2 briefly reviews ionospheric scintillation and irregularities, introduces the array instrument and processing of its database, the basics of estimation methods and a number of existing instruments for comparison discussed in the contributions. The main contributions in subsequent chapters are the following:

1.3.1 Automated Scintillation Monitoring. Chapter 3 presents a system for

automated detection based on scintillation indices from the array. A survey of scintillation data from year 2014 is performed to characterize the statistical occurrence of scintillation. An automated low-rate scintillation detection routine has been established and performed for each day in 2014 by screening the phase scintillation index. Days in question with potentially scintillating periods are selected as candidate times for estimating ionospheric irregularities. High-rate measurements during those scintillating periods are processed for subsequent analyses.

1.3.2 Estimation of Plasma Drifts and Anisotropy. Chapter 4 applies spaced-receiver techniques proposed and reviewed by [25, 36] to the GNSS array for detecting array-wide scintillation and estimating drift velocity, characteristic velocity, and anisotropy magnitude and orientation of the phase received at the ground due to irregularities. A sensitivity study is presented to understand how these estimates vary with cross-correlation parameters such as correlation value cut-off and estimation time interval. The horizontal drifts and anisotropy are estimated for periods during the top active days of scintillation detected over a year spanning December 2013 through November 2014. Results show the possibility of routinely quantifying ionospheric irregularities by drifts and anisotropy.

1.3.3 Error Analysis of Irregularity Estimates. Chapter 5 presents an error analysis on estimated properties to further evaluate the estimation quality. Uncertainties are quantified by ensemble simulation of noise on the phase signals carried through to the observations of the spaced-receiver linear system. These covariances are then propagated through to uncertainties on drifts through linearization about the estimated values of the state. A case study of a single scintillating satellite observed by the array is used to demonstrate the uncertainty estimation process.

1.3.4 Multi-instrument Study. Chapter 6 presents a multi-instrument study of the high-latitude scintillation. Measurements and ionospheric estimates from SAGA

array are compared to other in-situ measuring techniques such as incoherent scatter radar and all sky imagers to understand the dynamics and structuring of the auroral ionosphere on different scales. To quantify the comparison to ISR ion drift measurements, two case studies have been examined by deriving root-mean-squared errors on the array drift estimates.

Chapter 7 contains concluding remarks and future work. The system proposed in this dissertation aims at routine monitoring of scintillation and efficient characterization of irregularities, that may be applied at any latitude. Such an array may be used for irregularity monitoring at multiple scale sizes when multi-instrument studies are used, or for scintillation studies at remote locations where resources and infrastructure may be relatively scarce.

CHAPTER 2

IONOSPHERIC SCINTILLATION AND IRREGULARITIES

In this chapter, background materials on ionospheric scintillation and irregularities will be briefly covered. The sensing instrument used in this dissertation, its database and processing routines will be presented. The basics of estimation methods elaborated in the following chapters and several established instruments for comparison will also be reviewed.

2.1 Ionospheric Irregularities

Ionospheric irregularities have been observed all around the Earth (see Figure 2.1). At low-latitudes, plasma variations are often associated with diurnal (daily) solar radiation. Notable structures include equatorial bubbles that develop due to night time plasma depletion and the equatorial anomaly (plasma density maxima at 15-20° latitude, rather than at the geomagnetic equator), which cause amplitude scintillation. Irregularities are less common at mid-latitudes. High-latitude plasma variations are often driven by energetic particle precipitation along Earth's dipole field lines into the atmosphere, solar winds and disturbed interplanetary magnetic field. Phase scintillation is more common and usually correlated to night time aurora in the auroral and sub-auroral region, while at the geomagnetic poles it is often related to polar cap patches.

Due to the presence of both the Earth's magnetic field and dynamically generated electric fields, charged plasma moving along the field lines in the ionosphere develop motion patterns given the orientation of the two fields. Figure 2.2(a) shows the dipole model of the Earth's magnetic field. At location 1 in the northern hemisphere, the magnetic field line is pointing downward, and anti-sunward electric field

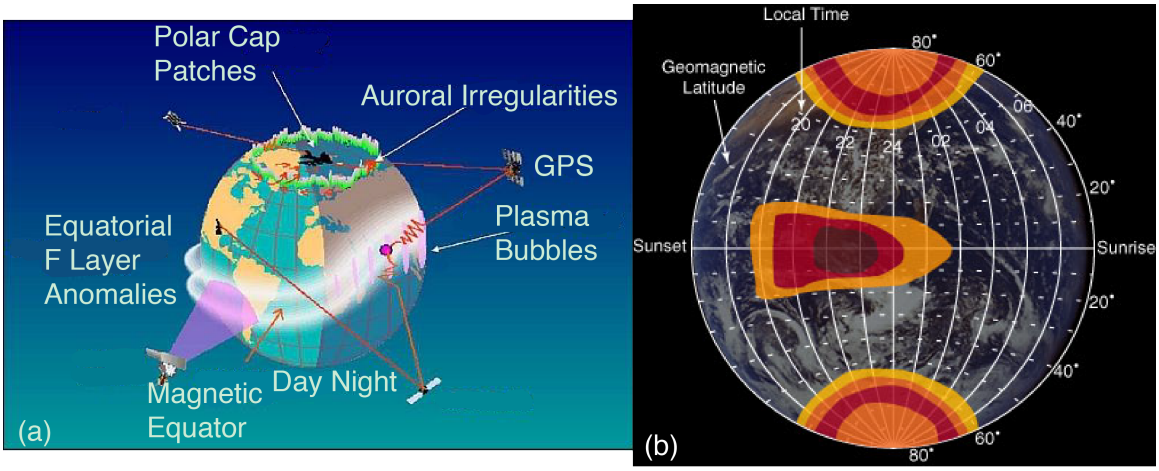

Figure 2.1. (a) Ionospheric irregularities, adapted from [37] and (b) scintillation occurrences observed at different latitudes, taken from [38].

(not shown). The field line is nearly horizontal at location 2 near the equator. Figure 2.2(b) shows an ion drifting under the influences of the Lorentz force. In the presence of only a magnetic field, a charged particle undergoes circular gyration motion (Figure 2.2(b), above). In the presence of orthogonal electric (downward) and magnetic (out of the page) fields, the charge will drift while gyrating. This drift motion of a plasma blob at a certain scale size is the quantity that is measured by the techniques described in this work.

2.1.1 Geomagnetic activity. Currents in the space environment superposed with Earth's internal field produce variations in the magnetic field. A number of measures of the disturbance are used to quantify the level of geomagnetic activity. Since scintillation is often associated with the Earth's disturbed magnetic field, it is useful to reference external indices that measure geomagnetic activity when studying scintillation.

One of these indices is the planetary Kp, a trihourly geomagnetic activity index, which can range from 0 (no activity) to 9 (extreme geomagnetic storm). Figure 2.3 is shown for demonstration.

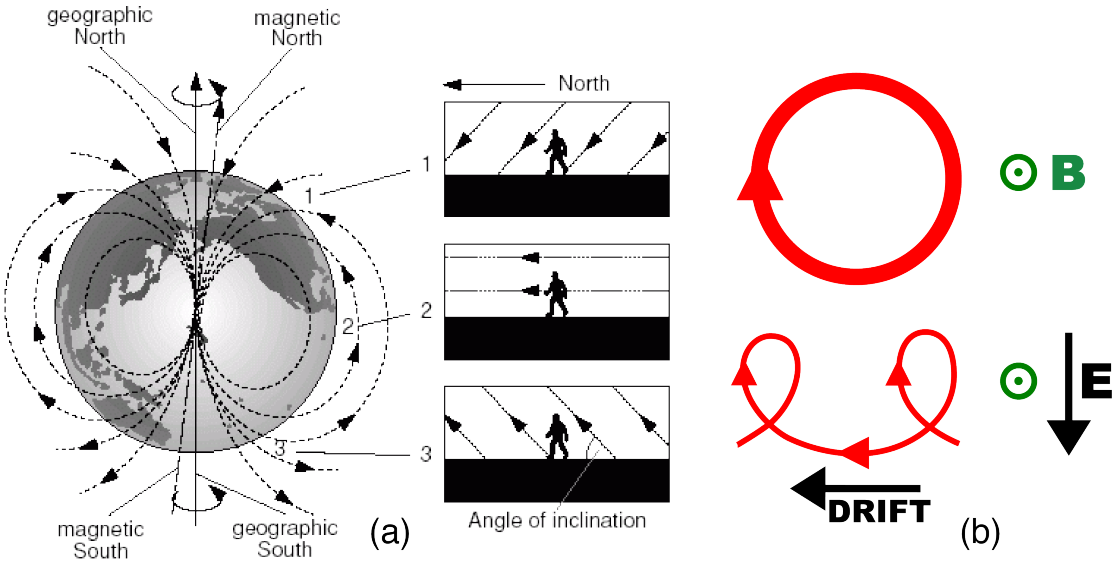

Figure 2.2. (a)Earth's magnetic field lines at various latitudes, taken from[39]. Declination angle is defined as that from geographic north to magnetic north. Inclination, or dip, angle is defined as that from the horizontal plane to the field line, positive in the northern hemisphere. (b)Gyration and $E \times B$ drift motion of a positively charged particle caused by the Earth's electromagnetic field, adapted from [40].

At high latitudes where auroral irregularities are observed, it is also useful to examine the auroral electrojet (AE) hourly index in nT, an example of which is shown in Figure 2.4. The AE index measures the maximum difference in magnetic field variation across worldwide high-latitude magnetometers.

The next two sections describe existing instruments whose data are used in this work. The GNSS receivers are used for analysis of the methods described, and the other instruments are used for comparison.

2.2 Jicamarca Radio Observatory

The Jicamarca, Radio Observatory is located in Peru in the equatorial zone. Jicamarca Unattended Long-term Investigations of the Ionosphere and Atmosphere (JULIA) is a 50 MHz coherent scatter radar designed to observe equatorial plasma

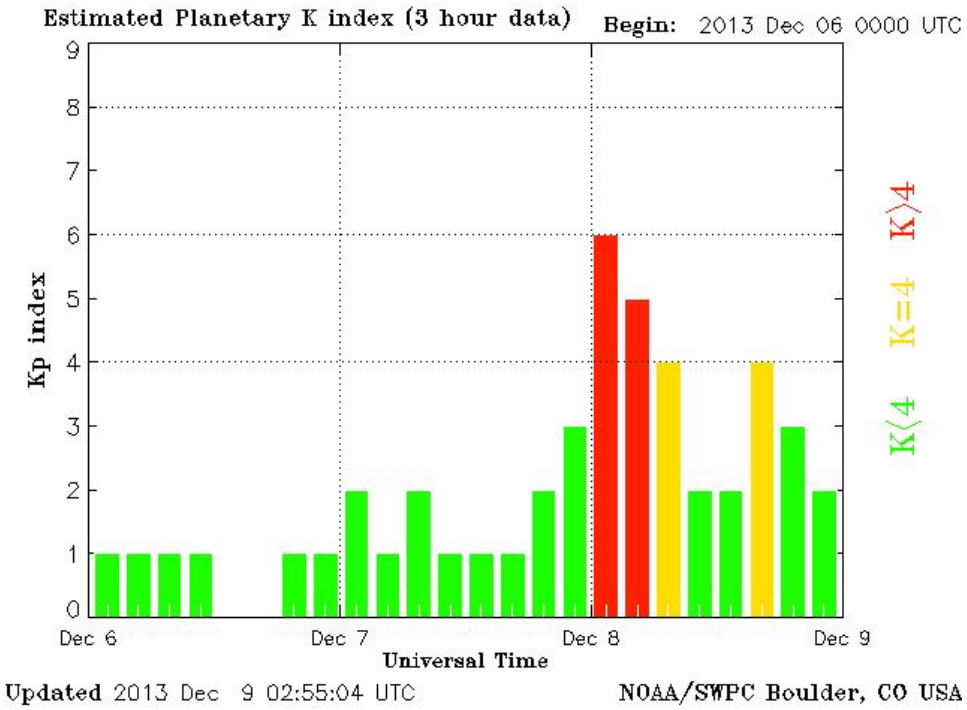

Figure 2.3. Trihourly Kp bar plots over the course of 3 days. Values in red indicate severe disturbances in the geomagnetic field. Values in green or yellow suggest quiet periods or minor disturbance. Courtesy of Space Weather Prediction Center [41].

irregularities and neutral atmospheric waves for extended periods of time. Although this dissertation mainly focuses on high-latitude studies using a GNSS array, it also includes a limited study of equatorial scintillation statistics featured in Chapter 3. The two GNSS instruments used in this study are two Novatel GPS ionospheric scintillation monitors with a separation of around 70 m, the locations of which are shown in Figure 2.5. Its baseline is configured to be aligned with geomagnetic east-west direction and sensitive to field aligned equatorial plasma bubbles.

The receiver pair was operational from early March to early May 2016 and recorded low-resolution (60 s) S_4 indices L1/L2C and high-resolution (50 Hz) at L1 data. Low-rate data includes amplitude scintillation indices and typical GPS observables Receivers have also recorded typical GPS observables such as pseudo-

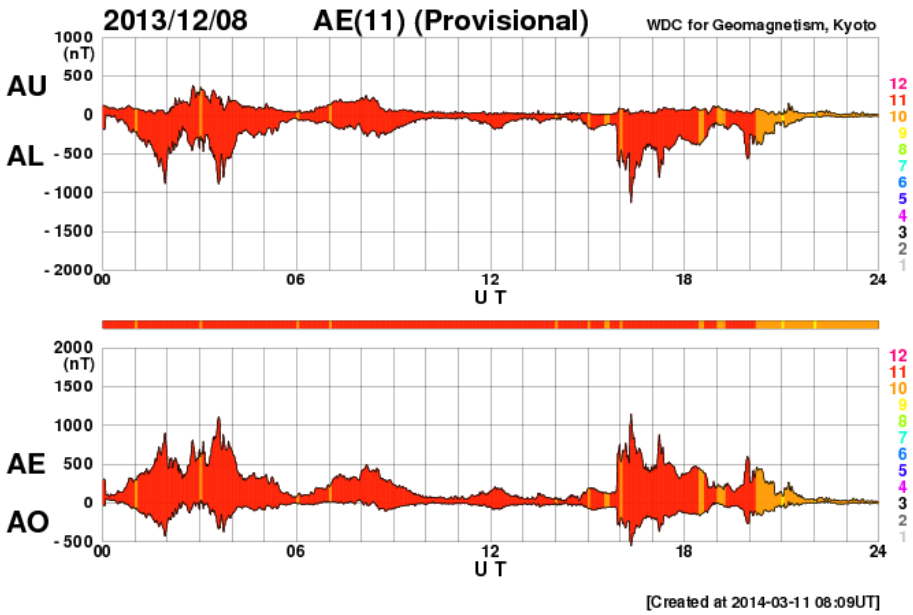

Figure 2.4. Auroral electrojet during a geomagnetic storm, derived from the difference of the upper limit AU and the lower limit AL. Courtesy of World Data Center for Geomagnetism, Kyoto [42].

range and carrier phase, receiver position, satellite IDs (PRNs) tracked, azimuth and elevation angle, and calculated total electron content (TEC) derived from both pseudo-range and carrier phase. High-rate data contains raw signal intensity as well as carrier phase. Phase data is not considered in this study since amplitude scintillation is more common in equatorial regions [1].

For demonstration, Figure 2.6 indicate positions of all available satellites in the sky during an scintillation event. Judging by the color scaled scintillation indices, PRN2 may be scintillating during 2022-2123 LT, although it is in the lower part of the sky. This potential event might be associated with sweeping equatorial bubbles known as equatorial spread F (ESF) developed during night time. An example of the structure is shown in Figure 2.7.

2.3 Poker Flat Research Range Instruments

Located at (57° N and 150° W) geomagnetically in the auroral zone, PFRR

Figure 2.5. The radar array at Jicamarca Radio Observatory, Peru at 11.95° S, 76.87° W with inclination 1.145° and declination 0.367°. The magnetic field line is nearly horizontal. The receiver pair O,E is also shown as tiny red pins, whose baseline points in the geomagnetic east-west direction nearly parallel to the local field line in white. Courtesy of Google Maps.

is home to a variety of instruments capable of investigating the auroral ionosphere. Two of these instruments used in the multi-instrument study discussed in Chapter 6 are briefly introduced here.

2.3.1 Poker Flat Incoherent Scatter Radar. Poker Flat Incoherent Scatter Radar (PFISR) is the site of an advanced modular incoherent scatter radar (AMISR), a phased array consisting of more than 100 antennas with electronic steering ability. Experiments with PFISR are conducted daily with up to 11 beams (transmitters) deployed at various latitudes to probe the dynamics and structuring of the ionosphere. Figure 2.8 is a sky plot that demonstrates PFISR beam configuration of an experiment. PFISR provides estimated values and uncertainties of drift velocities (used in this work), densities, and temperatures in field-aligned coordinates at 65° N to 70° N

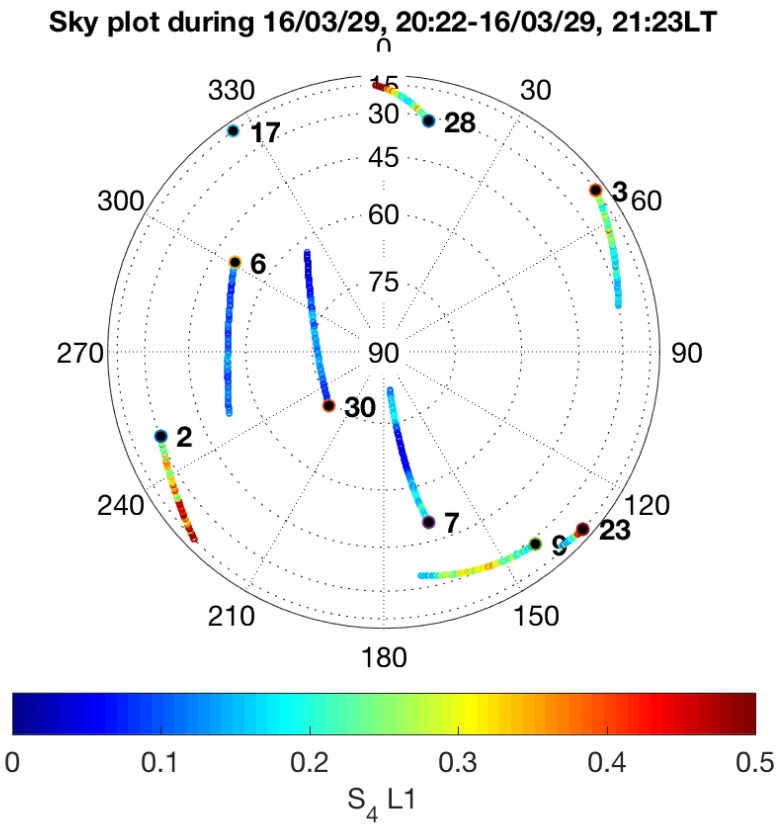

Figure 2.6. Color scaled S_4 time series as trajectories of all visible GPS satellites in the sky. Concentric circles indicate contours of satellite elevations while spokes indicate satellite azimuths.

at 60, 180, 300, or 500 s cadence, depending on the operating mode.

2.3.2 Poker Flat All-Sky Imager. The All-Sky Imager (ASI) provides monochromatic intensity maps of auroral and airglow emission for various lines of interest. Photo-metrically corrected images can provide horizontal context for simultaneous incoherent scatter radar measurements, as well as provide indications for the energy of precipitating electrons, existence of precipitating protons, and spatial extent of metallic layers. The instrument, based on similar telecentric cameras, employs a medium format 180 ° fish-eye lens coupled to a set of five 3-inch narrow-band interference filters. The current filter suite allows operation various wavelengths. The all sky camera in Poker Flat, Alaska provides 630.0 nm atomic oxygen (OI1D) emission

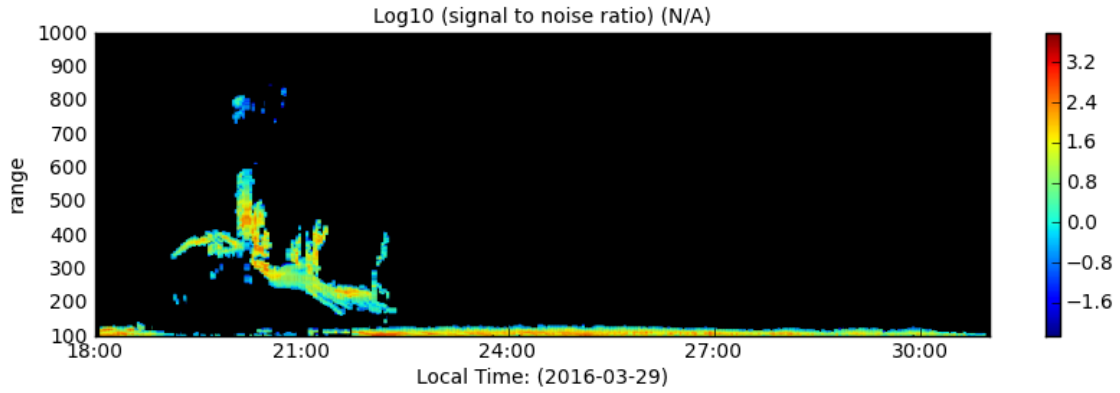

Figure 2.7. A daily observation of night time ESF by JULIA. Signal-to-noise of the radar echoes as a function of range depicts the developing shape of the structure over local time. Adapted from Jicarma Radio Observatory database [43].

data used in this work.

2.4 Scintillation Auroral GPS Array

The Scintillation Auroral GPS Array (SAGA) was established in late 2013 at Poker Flat Research Range (PFRR), Alaska. The array consists of six Connected Autonomous Space Environment Sensors (CASES) GNSS receivers designed by Atmospheric & Space Technology Research Associates (ASTRA) for dedicated space weather monitoring [45, 46].

Figure 2.9 displays the array location, with each site designated "IIT-" followed by a number. The receiver at IIT-13 is owned and operated by ASTRA. Receivers are sited at locations such that the baselines are either approximately aligned or perpendicular to the horizontal component of the Earth's magnetic field, with the longest baseline $\approx$ 2000 m. This configuration allows for detecting intermediate scale field-aligned irregularities.

2.4.1 Scintillation Indices. When scintillation and high-rate amplitude and phase data are collected from a GNSS receiver array, whether in a database or in real-time,

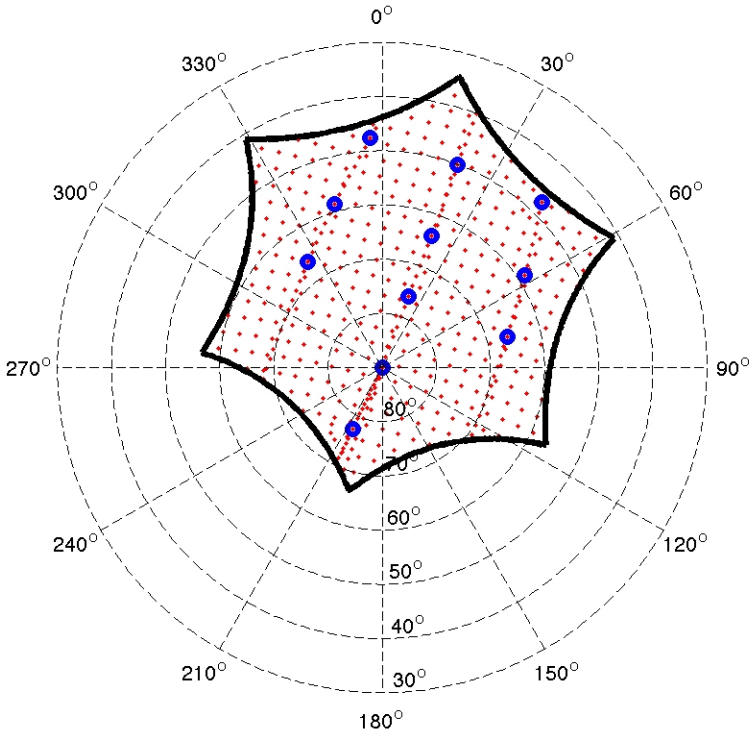

Figure 2.8. Sky plot of PFISR beams represented by blue dots. Spokes represents azimuth angle of the beams while concentric circles indicates elevation angles. The closed shape in black indicates radar sky coverage. Taken from SRI International ISR Database [44].

a typical first step is to detect and focus on periods during which scintillation is occurring. Receivers providing measures of normalized signal amplitude standard deviation S_4 index and/or phase standard deviation σ_Φ index, which are typically at a cadence of $\simeq 60$ s, provide natural metrics for detecting scintillation. If scintillation indices are not provided but high-rate in-phase (I) and quadrature-phase (Q) data are, then it is possible to compute S_4 and σ_Φ oneself [47, 48]:

$$S_4 = \sqrt{\frac{\langle SI^2 \rangle - \langle SI \rangle^2}{\langle SI \rangle^2}} \tag{2.1}$$

$$\sigma_\Phi = \mathrm{std}(\Phi) \tag{2.2}$$

Where SI is signal intensity derived from I and Q samples and $\langle\rangle$ represents time

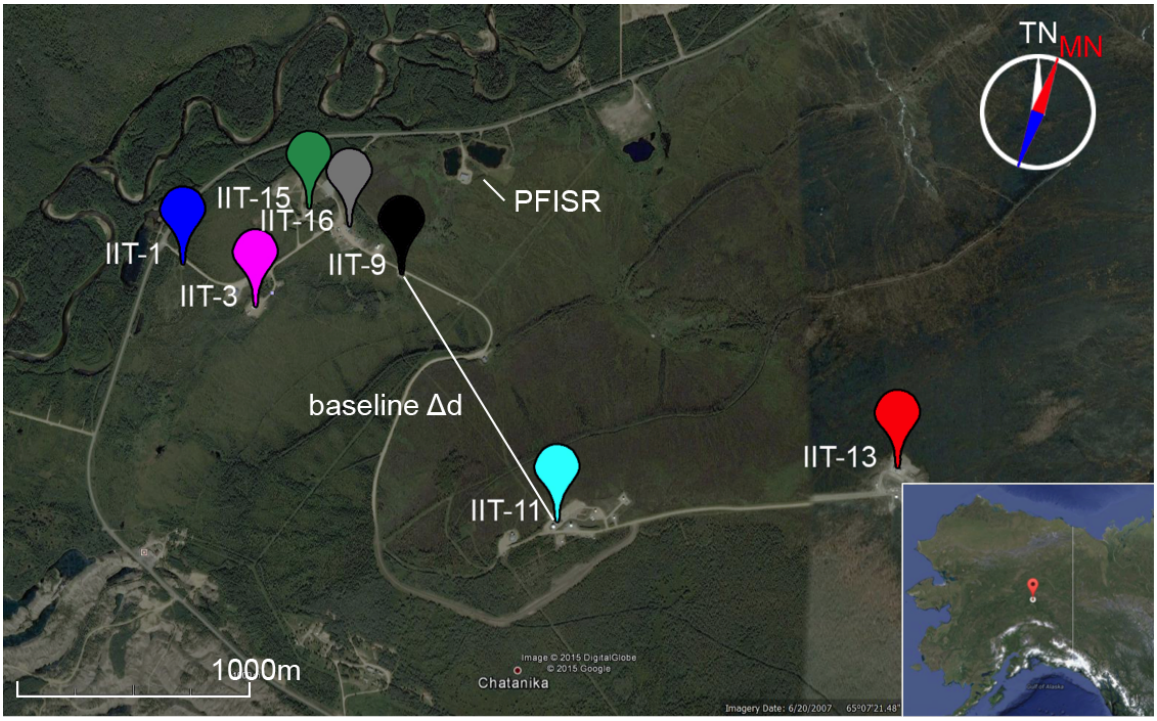

Figure 2.9. Map of scintillation aurora GPS array (SAGA) location (courtesy of Google Maps). Annotations show true north (TN) and magnetic north (MN). The declination angle (between TN and MN) $\approx 23.5°$ and the inclination angle $\approx 77.5°$. Courtesy of Google Maps.

averaging. With SAGA receivers the time interval is 100 s, and so the scintillation index data rate is 0.01 Hz produced by the receivers.

2.4.2 High-rate processed signal power and phase. In addition to scintillation indices each receiver produces 100Hz amplitude and phase data, derived from I and Q accumulations of the CASES software receiver. Detailed analyses with SAGA rely on the high-rate power and phase data typically sampled at 50-100 Hz from commercial scintillation monitors. To obtain detrended and filtered high-rate power/phase observations, processing of receiver-dependent high-resolution I and Q measurements for those time intervals is detailed by [49] following the signal processing procedure in [48, 47]. In effect, the phase measurements of a possibly scintillating channel and non-scintillating channel are differenced to reduce receiver clock effects, and a 6th

order high-pass Butterworth filter with cut-off frequency $f_c = 0.1$ Hz is applied to the differenced phase. For power observations, the raw power is filtered by a low-pass Butterworth filter with $f_c = 0.1$ Hz to produce low-pass-filtered power. Dividing raw power by the filtered product gives final power. While satellite motion, clock error, tropospheric delay, and cycle ambiguity are not explicitly modeled and corrected as would be needed in other applications [50], the detrending and filtering effectively eliminates these as slow variations from the phase. However, note that the phase filtering technique does not detect or correct cycle slips and therefore the final phase value may be more than a complete cycle ($> 2\pi$ rad).

2.4.3 SAGA database. SAGA has been continuously operating at PFRR since December 2013 and provides scintillation data at L1 and L2C frequencies for each visible satellite given by its Pseudo-Random-Number (PRN). Figure 2.10 show the array architecture.

Low-rate (LR) Scintillation indices S_4 and σ_Φ at 0.01 Hz and additional data (e.g., total electron content and XYZ position solutions, azimuth AZ, and elevation EL, pseudoranges ρ and carrier phase Φ) at 1 Hz are streamed in real-time by network to a server; these same data plus 100 Hz amplitude and phase are stored locally at each receiver. The high-rate (HR) power and phase data (represented by "I" and "Q" in the figure) are transferred to the server post-process. The high-rate phase data are detrended and filtered according to [49], in which measurements of a possibly scintillating channel and non-scintillating channel are differenced to reduce receiver clock effects, and 6th order high-pass Butterworth-filtered [47].

If real-time analysis is not needed, detection can be done manually, by generating "Quicklook" plots of amplitude scintillation index S_4 or phase scintillation index σ_ϕ and scanning them visually. Figure 2.11, 2.12 respectively show the power/phase scintillation severity on February 20, 2014 sorted by receiver. The color scale of σ_Φ/S_4

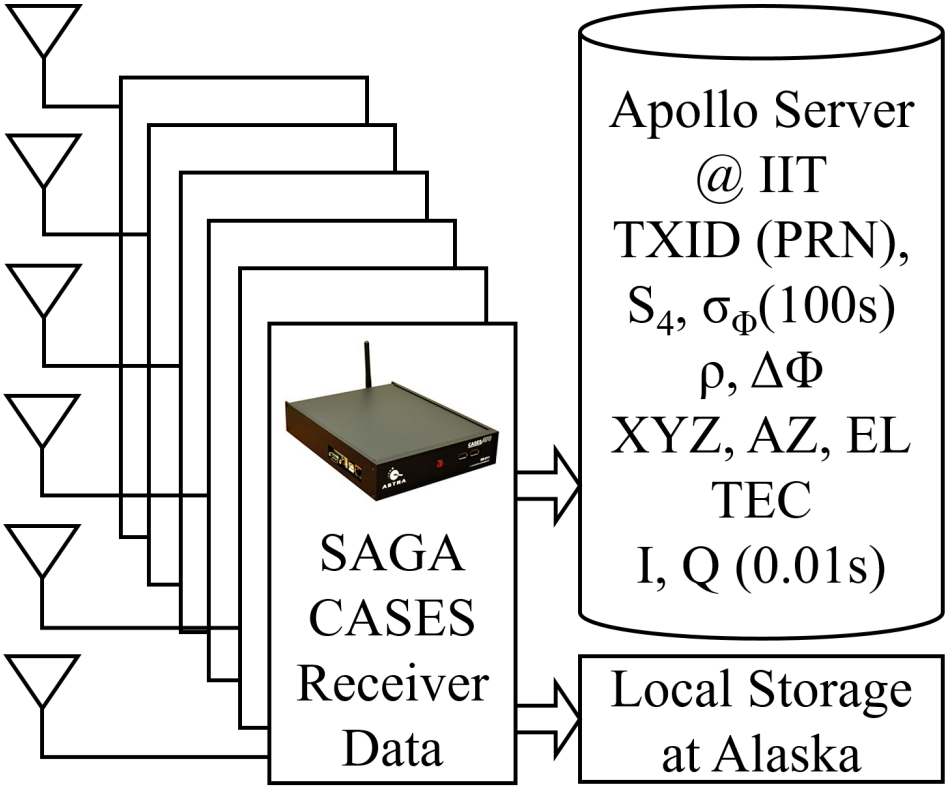

Figure 2.10. Scintillation auroral GPS array (SAGA) architecture.

corresponds to its value to emphasize elevated scintillation. Several time periods of increased phase variance can be observed. Multi-path effects can sometimes inflate signal variation and be mistaken for scintillation. The multi-path pattern tends to repeat daily for a unique receiver-satellite combination and could be avoided by removing data from low elevation satellites $\leq 30°$. Figure 2.12 shows times when all receivers detect scintillation simultaneously. If all receivers indicate elevated index values, individual clock or multipath effects are less likely since those are independent for each receiver. Figure 2.13 shows scintillation levels for individual satellites. One may identify PRN 29 as a scintillating satellite by eye from this figure. Quicklook plots can be useful for individual case studies during particular dates of interest on particular scintillating satellites. SAGA data and daily Quicklook plots are available for viewing and download at `http://apollo.tbc.iit.edu/~spaceweather/` .

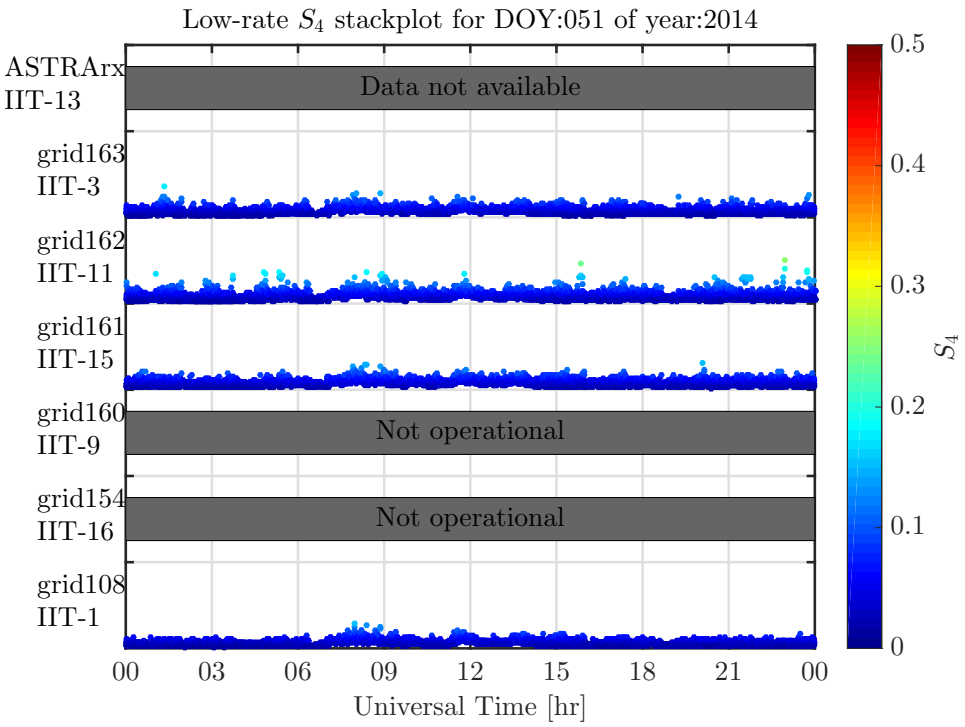

Figure 2.11. S_4 measurements by receiver from SAGA.

2.5 Challenges

One of the challenges SAGA presents is how researchers may efficiently and systematically detect scintillation events from a large amount of data being collected. Figure 2.14 compares the size of data of various duration for different formats. Originally transmitted and stored in binary format, pre-processed data from the receivers have to be unpacked to text log for any further analysis. Firstly, scintillation events last usually several minutes to an hour, an example of which is shown in Figure 2.15 with 100 Hz amplitude and phase data shown over about one *minute*. In other words, only a small amount of binary files from the database is worth unpacking, filtering and analyzing.

Figure 2.16 illustrate how the contributions deal with the presented challenge. To efficiently detect a potential event, a data screening algorithm is required and

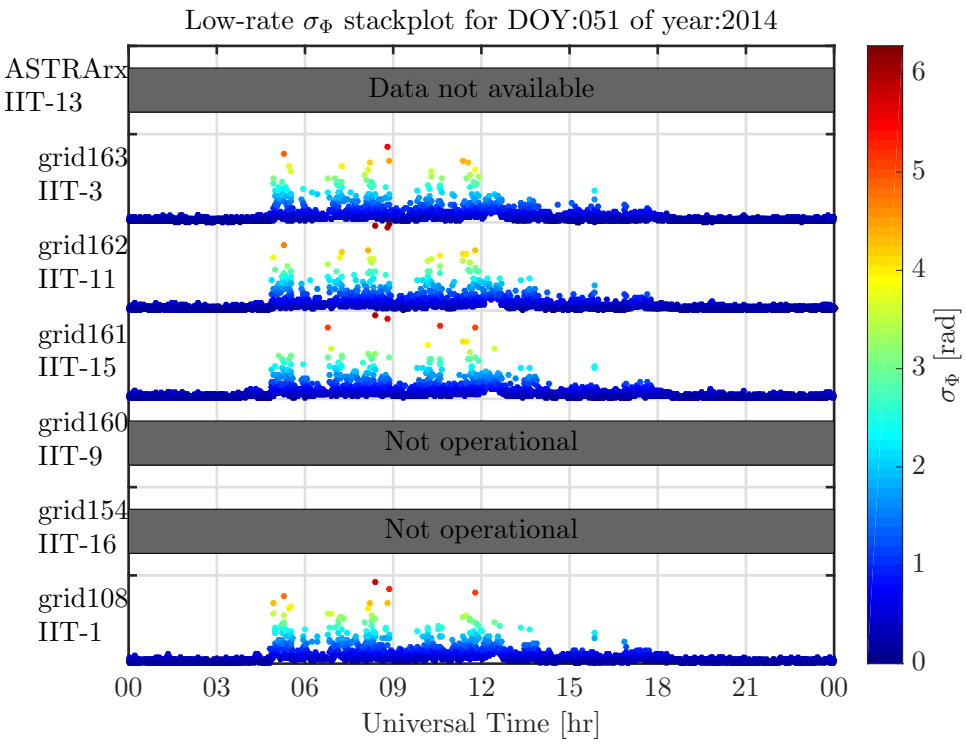

Figure 2.12. σ_ϕ measurements by receiver from SAGA.

developed in Chapter 3. Secondly, while low-rate data require less time to process, high-rate data processing of multiple receivers together is needed to estimate the properties of the received signal on the ground, which are due to the irregularities. The methods will be elaborated in Chapter 4. Thirdly, Chapter 5 derive errors on the estimates for further evaluation. Lastly, Chapter 6 compare the estimates with measurements from a existing collocated instrument.

2.6 Summary This chapter briefly reviewed ionospheric scintillation and irregularities, introduced the array instrument and processing of its database, the basics of estimation methods and a number of existing instruments for comparison discussed in the contributions.

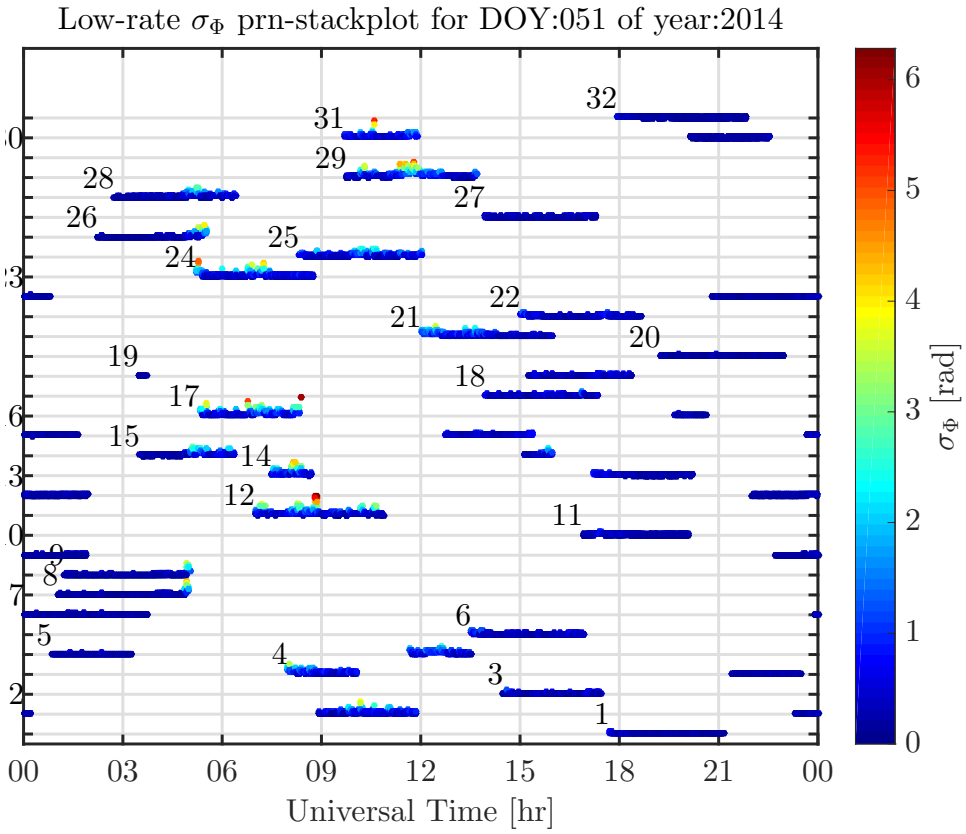

Figure 2.13. σ_ϕ measurements by satellite from SAGA.

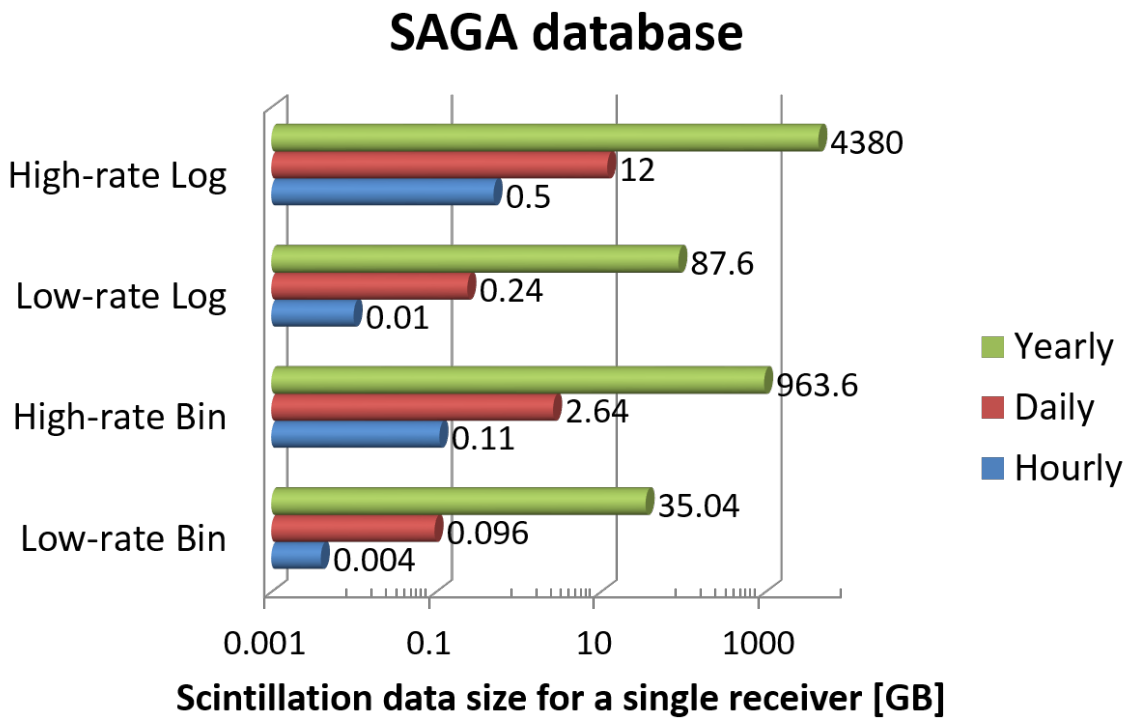

Figure 2.14. Estimated data size for SAGA data of different lengths and in different formats.

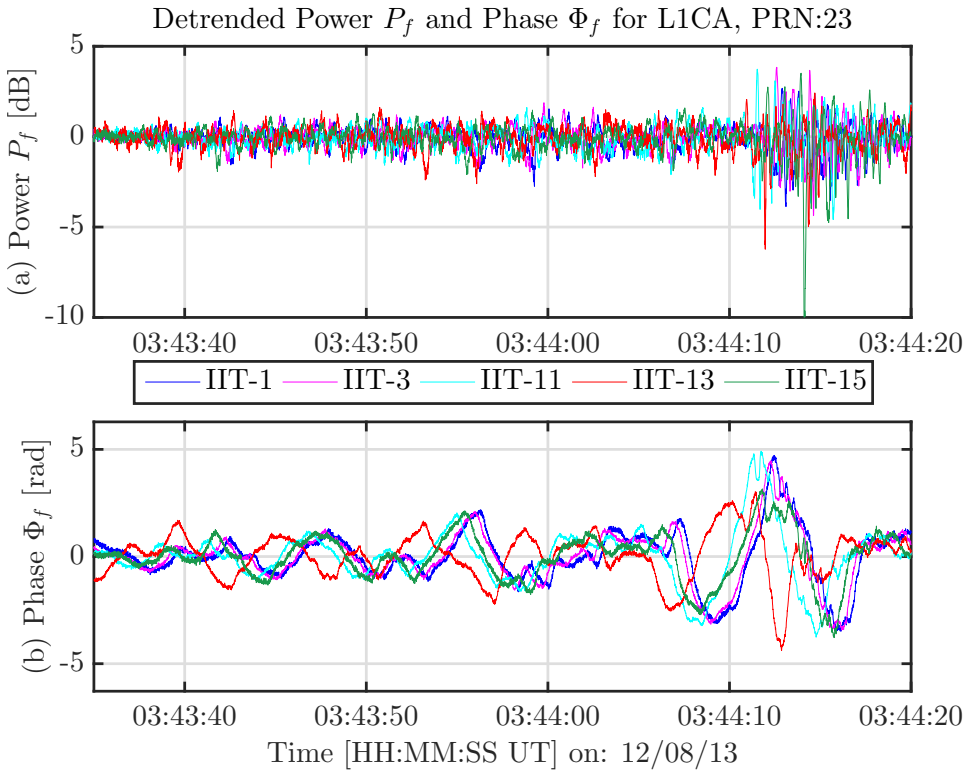

Figure 2.15. A scintillation event with intense phase/power variations during a geomagnetic storm. Signal (a)power and (b) phase are possessed, filtered from 100Hz IQ data for color-coded SAGA receivers.

Instruments	Scintillation Auroral GPS Array (SAGA)			SAGA+ Other colocated instruments
Data	Low-Rate Data	High-Rate Data		
Contribution	1) Automated Scintillation Monitoring	2) Estimation Of Plasma Properties	3)Uncertainties of Irregularity estimates	4) Multi-Instrument Study
Results	Detected Events	Estimates	Error Bars	Comparison

Figure 2.16. Contribution road map.

CHAPTER 3

AUTOMATED SCINTILLATION MONITORING

This chapter presents an automated GPS receiver data collection and processing routine multi-baseline receiver measurements from the array. An overall survey has been conducted to investigate the daily and seasonal characteristics of the phase scintillation events near Poker Flat Alaska in the auroral region. Another survey has been conducted in a similar fashion in Jicamarca Radio Observatory in the equatorial region on amplitude scintillation statistics. A set of routines has been developed for automated scintillation monitoring to select active days of interests and potential scintillation periods for possible satellite channels.

3.1 Scintillation Statistics Survey

Scintillation is known to be correlated with time of the day, season and physical instabilities in the ionosphere. Surveys have been conducted to observe the temporal behavior of scintillation statistics.

3.1.1 Scintillation Statistics near Poker Flat. It is known that at high latitudes, phase scintillations are observed more often than amplitude scintillations due to a variety of physical instability mechanisms in both the E and F regions of the ionosphere [11]. Therefore, phase scintillation indices σ_Φ, are systematically examined to identify hourly, daily or seasonal dependence. These patterns are used for characterizing high-latitude scintillations.

Figure 3.1 shows how σ_Φ measurements are distributed in the four seasons of year 2014. Invalid values computed by the receiver and data from low elevation are thrown out to mitigate multi-path effect. The color scales are mapped to the

vertical axis values to emphasize elevated scintillation. SAGA array is assumed to have local time LT = UT-9. The 15-20 LT interval (00-05 UT) is a generally quiet period throughout the whole year 2014. Phase scintillation then becomes much more severe during local night time 21 LT to 09 LT (06-18 UT), which is mainly associated with the night time aurora phenomenon. Phase fluctuations are generally low again during 10-11 LT (19-20 UT). A large amount of elevated phase scintillation are also observed over 12-14 LT during winter. There are two possible explanations for this observation. It might be a single receiver issue due to multipath or malfunctioning, or cycle slip effects related to physics of the ionosphere such as passage of polar cap patches, localized enhancements in plasma density which originate from solar ionization on the day side.

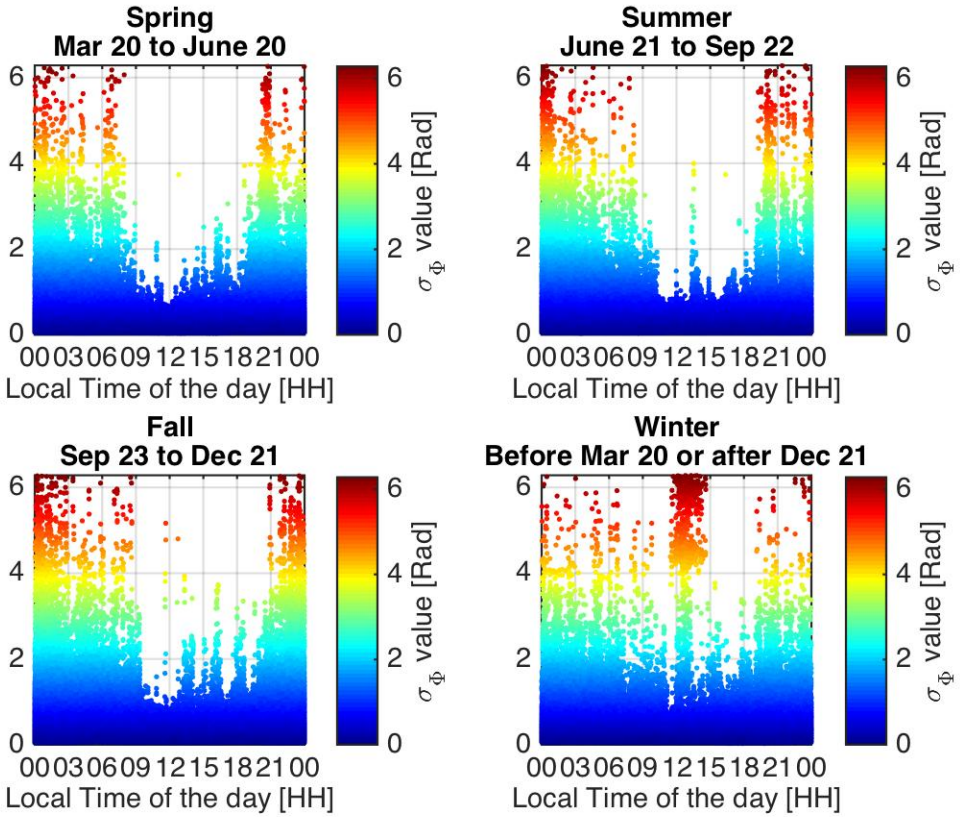

Figure 3.1. Seasonal distribution of phase scintillation index σ_Φ throughout year 2014.

Similarly, Figure 3.2 describes the phase scintillation statistics on a daily basis using the same data set in Figure 3.1. Phase scintillation index values for each day of 2014 are color-scaled in the same fashion as in Figure 3.1. The horizontal axis is the day of year while the vertical axis is the local time of the day. Additionally, sunrise and sunset times for each day of year, are also plotted respectively in red and black solid curves. It can be observed that most of the elevated phase scintillation values are found after sunset and before sunrise. An exception is also observed during winter around noon. One explanation for this particular phenomenon is produced by polar cap patches from the day side ionosphere.

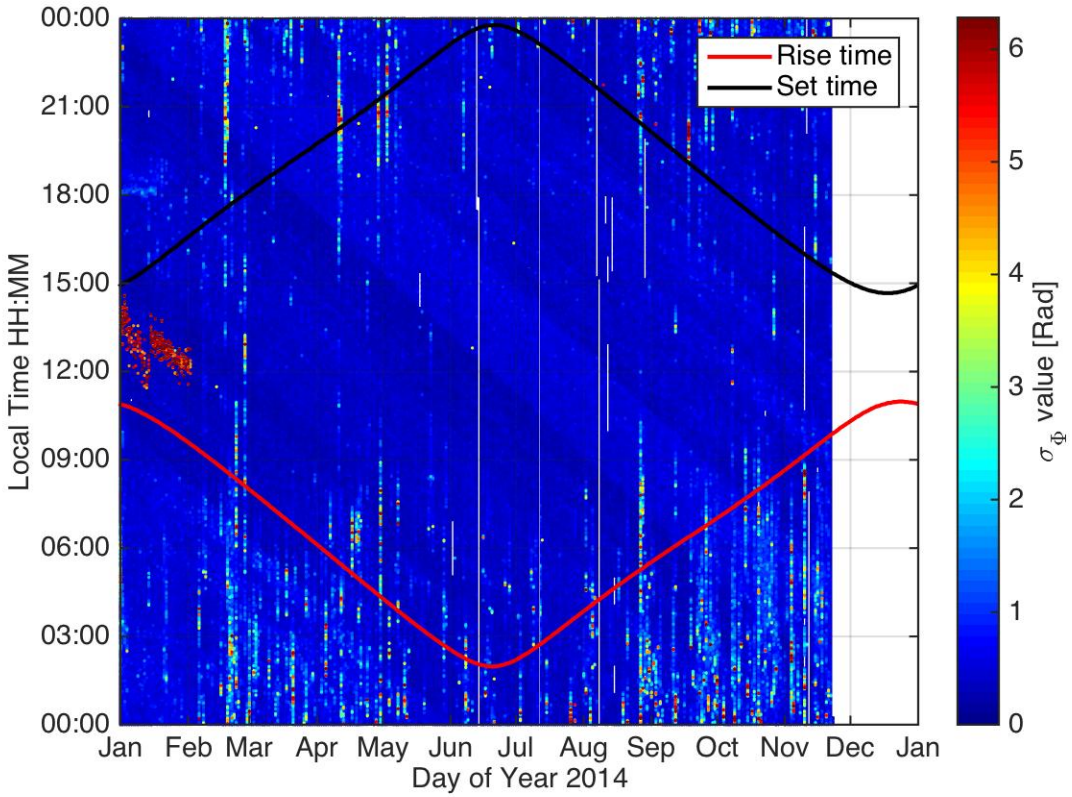

Figure 3.2. Daily distribution of phase scintillation index σ_Φ through year 2014 with solar terminators.

From Figures 3.1 and 3.2, it is reasonable to conclude that in Poker Flat region phase scintillation does not seem to have a seasonal dependence but is associated with

the diurnal cycle.

3.1.2 Scintillation Statistics near Jicamarca. Figure 3.3 shows daily occurrences of amplitude scintillation events from all available data. Data from low elevation $\leq 15^{\circ}$ are thrown out to mitigate multi-path effect, which is unique to each pair of receiver-satellite pattern. Therefore, the intersection of events recorded by both receivers is needed to properly identify scintillation.

Similarly, Figure 3.4 describes hourly occurrences of S_4 statistics with the same data set. The array is assumed to have local time LT = UT-5. Elevated S_4 values can be found scattered throughout the whole day. Compared to day time, amplitude scintillations are more severe during local night time 18 LT to 06 LT, which may be associated with the night time equatorial spread F phenomena.

3.2 Automated Scintillation Detection Routine

The previous section demonstrates the scintillation characteristics collected by the two arrays in different latitudes. It can be roughly observed that scintillation has a daily pattern correlated with the night time ionosphere. For in-depth investigation, however, it is more efficient to have an algorithm that systematically monitors this behavior and detects potential events.

For a continuously operating array, collecting scintillation indices and high-rate power and phase data may result in over 2 GB binary data per day (see Figure 2.14), for an array of 4 to 6 receivers. This makes manually identifying scintillating periods cumbersome. Initial scintillation monitoring and detection are needed to efficiently identify candidate time periods whose data should be unpacked and more closely analyzed for quantifying irregularity structure properties. This section develops an automated routine taking advantage of scintillation indices produced by each receiver in the array. This post-process detection technique consists of two stages, illustrated

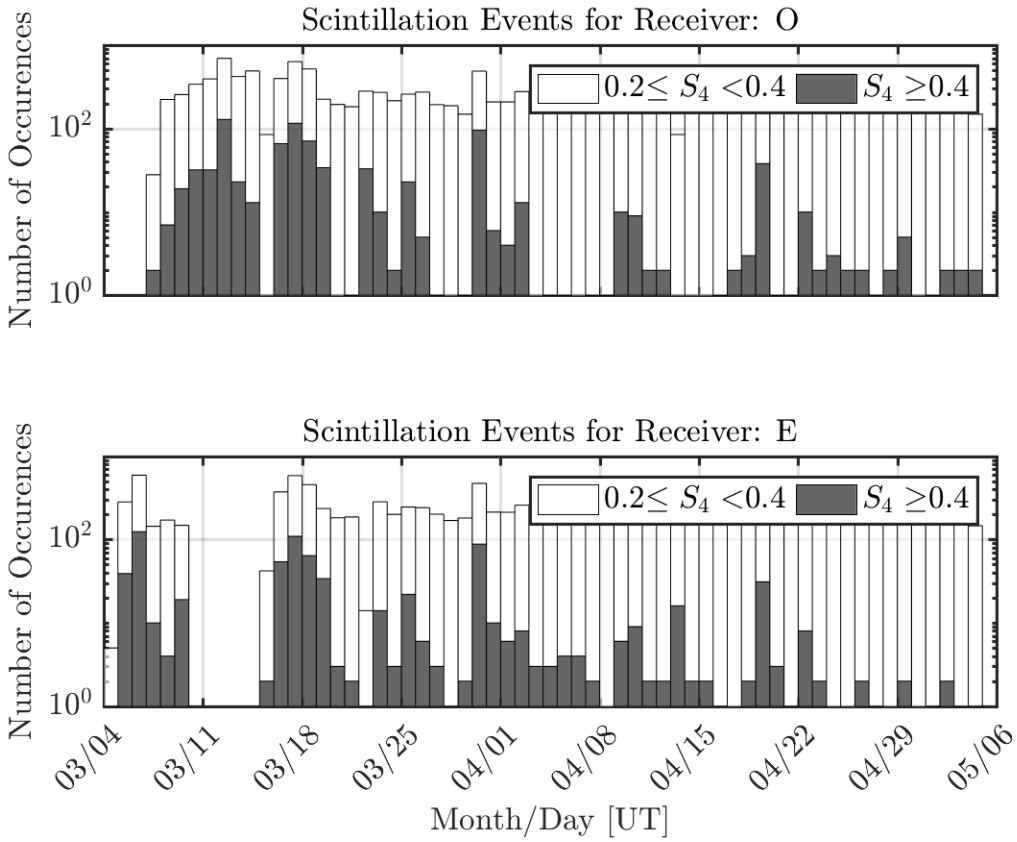

Figure 3.3. Daily occurrences of amplitude scintillation events recorded by the receiver pair. Histogram in white represents weak scintillation while histogram in black for moderate scintillation.

in Figure 3.5.

3.2.1 Stage 1. The first stage ranks multiple days by severity of scintillation, by scanning through the scintillation indices from all available receivers on each day. The scintillation indices from each operational receiver are filtered to eliminate data collected at low elevation ($\leq 30°$), since multipath effects can sometimes artificially inflate the scintillation indices. Days for which there are fewer than a minimum number of receivers operating are discarded; at least three are required for the subsequent analysis described in following chapters. Then a single daily metric, the weighted

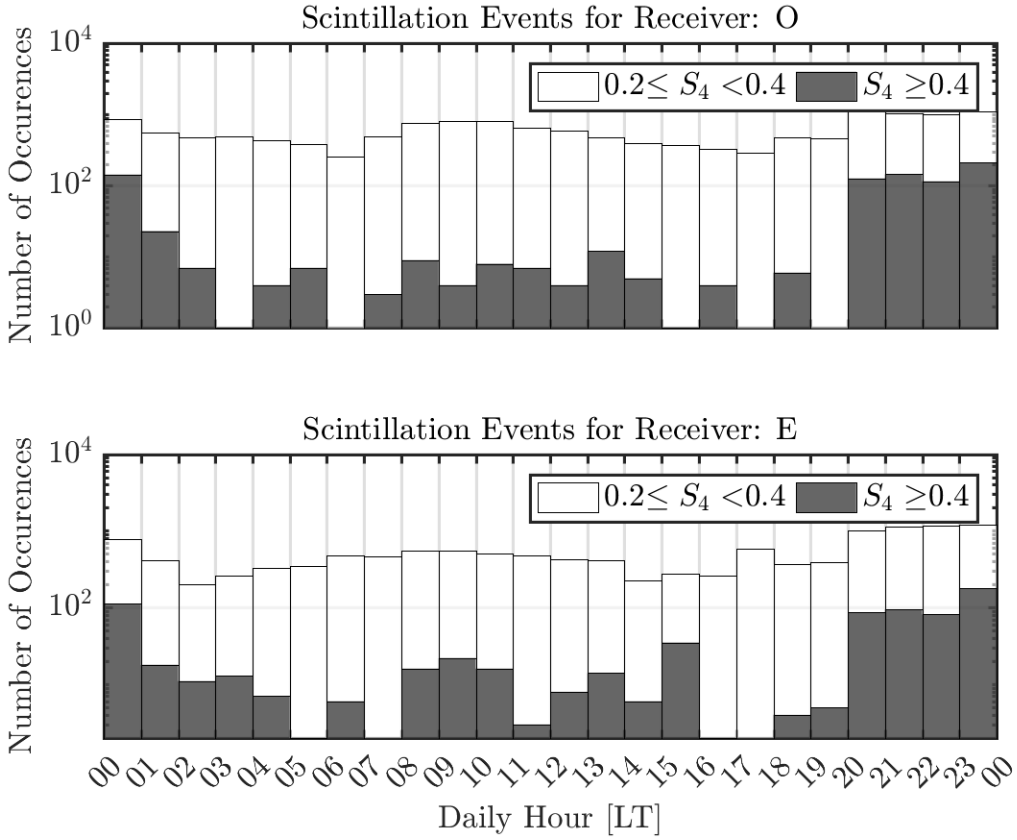

Figure 3.4. Hourly occurrences of amplitude scintillation events recorded by the receiver pair. Histogram in white represents weak scintillation while histogram in black for moderate scintillation.

scintillation number, quantifying the severity of scintillation is computed:

$$WSN = \frac{N_{stat}th_{stat} + N_{dyn}th_{dyn}}{th_{stat} + th_{dyn}} \tag{3.1}$$

The WSN counts the array-wide average number of data points N_i exceeding scintillation index thresholds $th_i, i = \{stat, dyn\}$. Both a constant threshold scintillation value th_{stat} and a dynamic threshold th_{dyn} that is unique to each day but applied to all receivers and all satellites are used to compute WSN. The static value relates to a baseline level of noise on the scintillation indices over all receivers and all days. The dynamic value varies by day to be more selective on active days. WSN effectively counts the number of scintillation index measurements exceeding thresholds, such that more active days have higher WSN. Days sorted by WSN in descending order

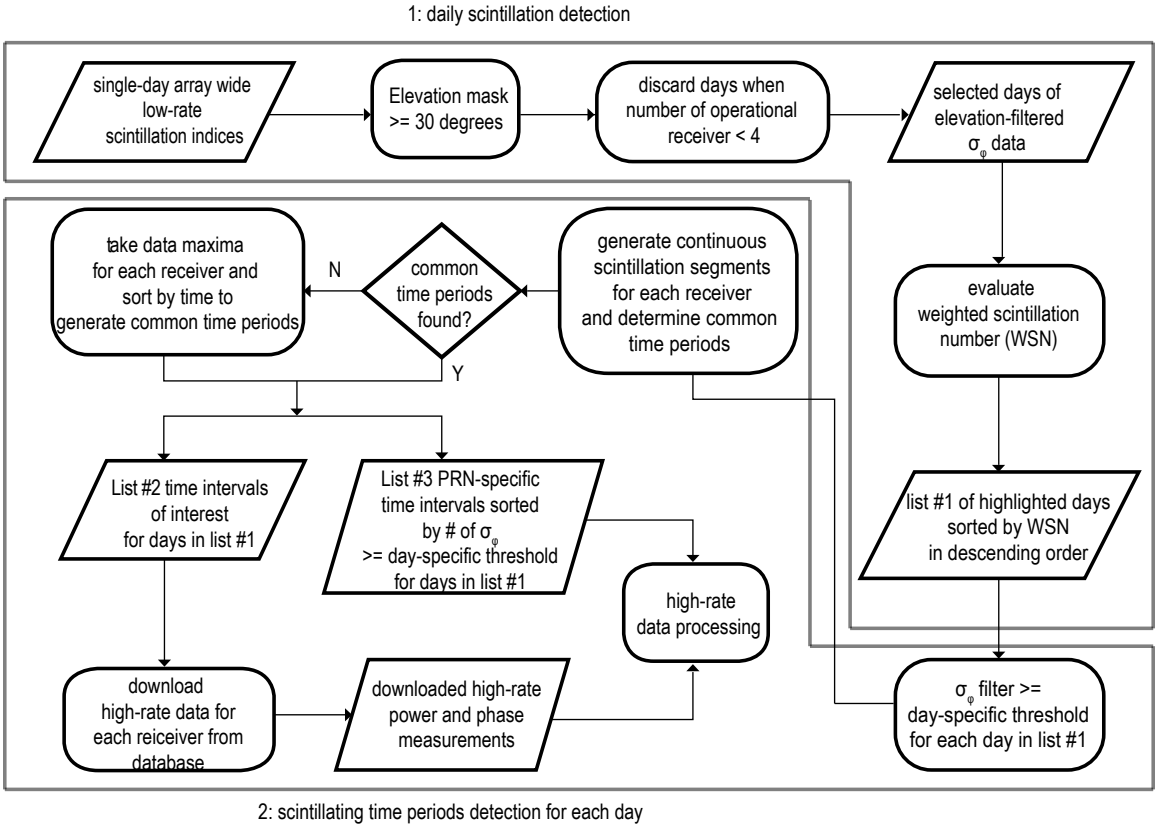

Figure 3.5. Flowchart for automated scintillation detection routine.

are saved into a list; an example is shown in Table 3.1. In this table the mean σ_ϕ is computed over all satellites and all receivers at L1 frequency for that date. Because scintillation may at times be correlated with geomagnetic activity, the sum Planetary K-index (Kp) for each day is also given along with the auroral electrojet (AE) index that measures auroral activity.

3.2.2 Stage 2. For each scintillating day in the table resulting from Stage 1 (e.g., Table 3.1), a second stage of processing identifies the satellites whose signals at all receivers were scintillating, and the time intervals for which that scintillation is common to all receivers. A scintillating satellite is defined such that the daily average scintillation value unique to that satellite in view across all receivers exceeds th_{dyn}. The scintillation indices from all receivers tracking a single satellite are compared to

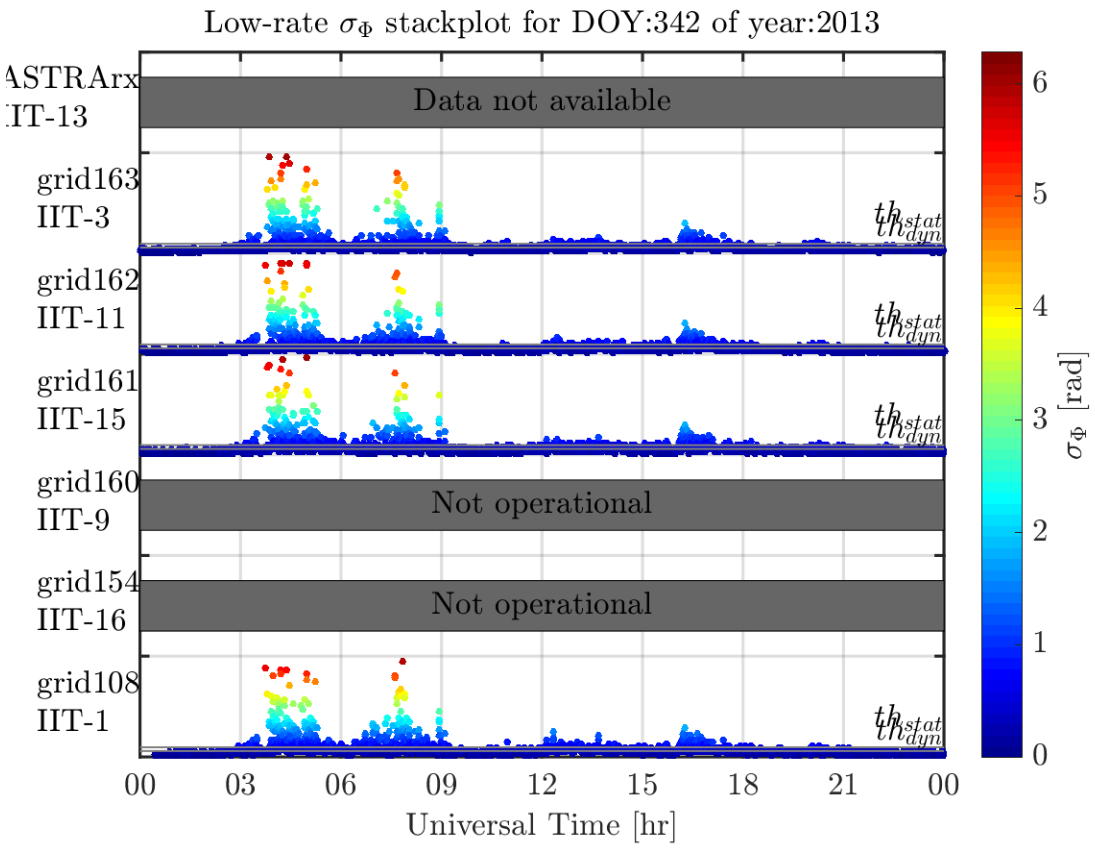

Figure 3.6. σ_ϕ measurements by receiver from SAGA. Grey lines indicate triggers th_{dyn} and th_{stat}.

identify time periods of interest for a scintillating satellite. The cartoon in Figure 3.7 illustrates this technique with two receivers' scintillation indices as a function of time (either S_4 or σ_Φ may be used). A scintillation index threshold defines the period of "scintillation" at each receiver. In addition, a time interval criterion is chosen to help demarcate "continuous" scintillation. For example, in Figure 3.7 between times $t_{1,1}$ and $t_{2,1}$ at least three consecutive scintillation index values below the threshold occur for receiver 1, so are designated in the illustration as separating two different intervals of scintillation. Continuous scintillation intervals for each receiver are compared across receivers to find common time intervals of scintillation over the whole array. Depending on the index threshold, the time interval criterion, and the index data rate (0.01 Hz), common time intervals may be minutes to hours long (illustrated

Table 3.1. Top 10 active days of year (DOY) from December 2013 to 2014 sorted chronologically (day 342 is in 2013). K_p measures the global geomagnetic activity. AE measures the auroral geomagnetic activity.

DOY	WSN	$\bar{\sigma}_\Phi[rad]$	$\sum K_p$	$\max AE[nT]$
342	**755**	**0.3667**	**27**	**736**
050	1070	0.4611	34	1198
051	875	0.4047	32	1236
102	973	0.4307	26	773
120	1118	0.4822	23	1004
239	1118	0.5164	25	1075
282	1012	0.4033	21	645
293	1057	0.4431	30	1271
308	898	0.3875	25	856
314	881	0.4911	27	714

in red at the bottom of Figure 3.7). Stage 2 results in a list of time intervals and satellites (PRNs) for which scintillation was occurring for all receivers operational, for each day of scintillation identified in stage 1. An example of this list is Table 3.2.

Not only can the algorithm shown in Figure 3.7 detect single-satellite events across all receivers in Table 3.2, but it also can detect multiple-satellite events during the same time periods. For instance in Figure 3.8 and 3.9, the detected single-satellite events are re-plotted for each satellite. The intersections of events across all channels in question are computed in the same fashion and plotted from the bottom for groups of $N_{set} \geq 2$ up to 3 satellites. The PRNs are listed for the intervals with three

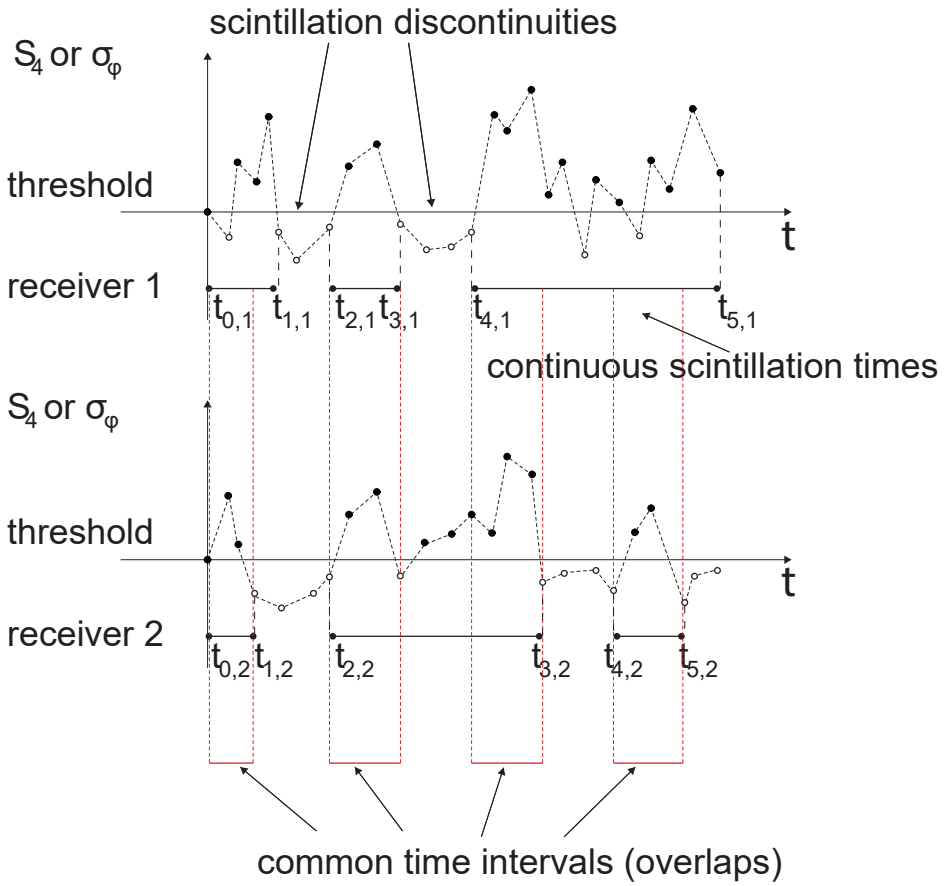

Figure 3.7. The method to distinguish continuous scintillation times for each receiver and identify common time intervals across receivers. For example, there are scintillation discontinuities for receiver 1 during $(t_{1,1}, t_{2,1})$ and $(t_{3,1}, t_{4,1})$ since 2 or more σ_Φ values stay below the threshold consecutively within these intervals.

satellites scintillating. There are no overlaps among any combination of 4 satellites. The obtained multi-satellite events are summarized in Table 3.3.

3.3 Scintillation Events Discussed in This Dissertation

Events in the following list identified in this chapter are revisited in the rest of this dissertation. They are organized into Table 3.4 sorted by start time t_0 for future reference.

A) December 8th 2013 : An active day detected with the routines discussed in this chapter, during which a moderate geomagnetic storm was recorded due to a

Table 3.2. Scintillation periods generated and sorted by the average σ_Φ in rad with start time t_0 and end time t_f, duration Δt,and average number of samples/receiver.

PRN	t_0	t_f	Δt [min]	$\bar{\sigma}_\Phi$[rad]	#
23	0343	0417	34.076	2.5573	64
13	0403	0438	34.354	2.3311	79
13	0448	0517	28.85	1.9666	69
9	0736	0804	28.02	1.9604	63
10	0350	0441	50.783	1.5614	116
8	0731	0804	33.4	1.3195	77
16	0456	0515	19.123	1.175	45
26	0738	0755	16.834	1.131	35
31	1605	1639	34.721	1.0556	82
29	1608	1623	14.304	0.93619	34
25	1613	1631	17.888	0.83252	44

strong co-rotating interaction region (CIR) followed by the coronal hole high speed stream (CH HSS) on December 7th [51].

1) 0343-0417 UT for PRN 23

2) 2615-2660 s after 0300 UT (03:43:15-03:44:20) for PRN 23

3) 0343-0417 UT for PRN 10, 13, 23

B) February 20th 2014 : An active day detected with the routines discussed in this chapter, during which a major storm condition was reported due to coronal mass injection (CME) [52].

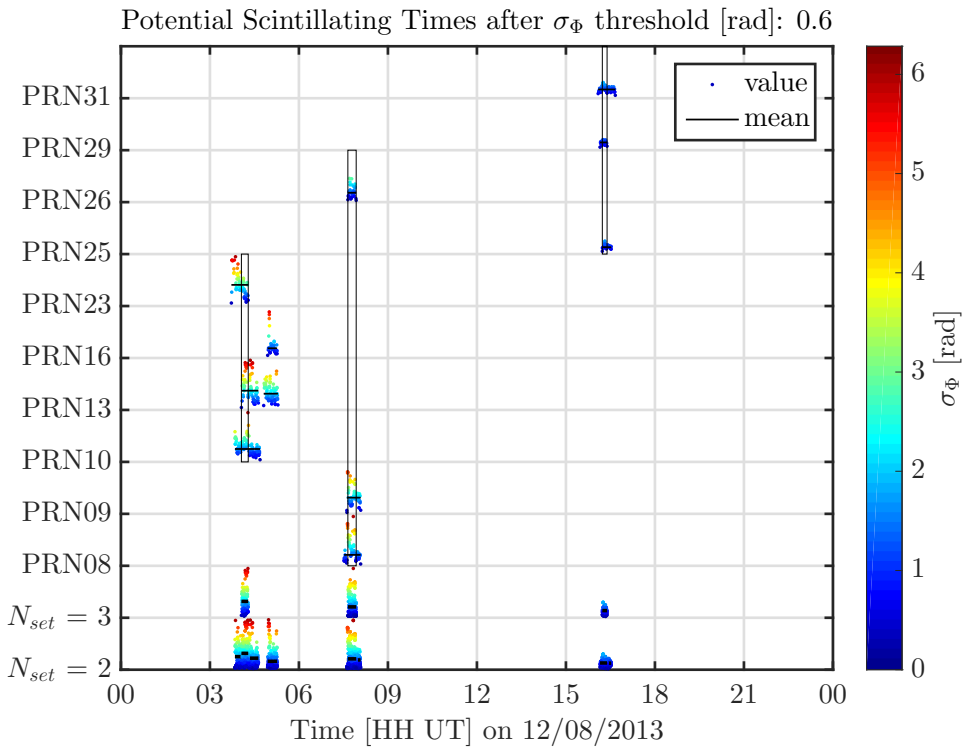

Figure 3.8. Detected multi-satellite events for 12/08/2013.

1) 1120-1157 UT for PRN 29

2) 2685-2729 s after 1100 UT (11:44:25-11:45:29) for PRN 29

C) March 17th 2015 : An active day detected with the routines discussed in this chapter, during which a severe geomagnetic storm condition was observed due to coronal mass ejection effects from March 15th [53].

1) 1302-1325 UT for PRN 18, 22, 27

3.4 Summary

This chapter presents a system for automated detection based on scintillation indices from the array. A survey of scintillation data from SAGA database for year 2014 is performed to characterize the occurrences of the scintillation statistics. It is concluded that phase scintillation observed at Poker Flat in the auroral region

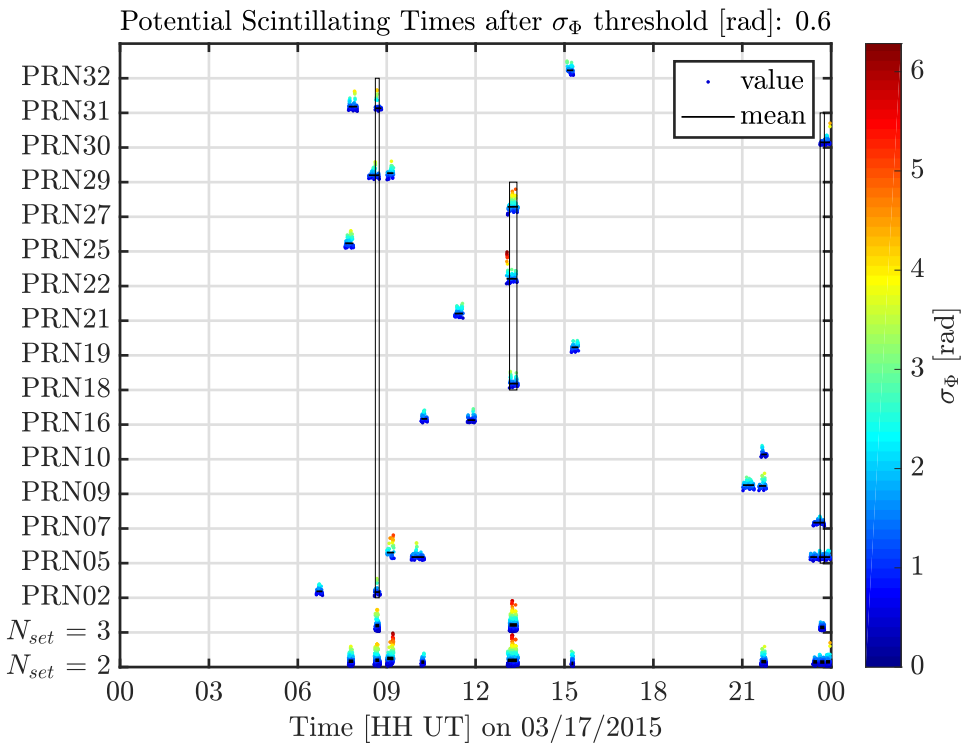

Figure 3.9. Detected multi-satellite events for 03/17/2015.

does not seem to have a seasonal dependence but associated with local nighttime. It is also found that amplitude scintillation at Jicamarca in the equatorial region is mostly observed after local sunset. An automated low-rate scintillation detection routine that consists of two stages has been established and performed for each day in 2014 by screening the phase scintillation index. Days of significant scintillation are selected with the proposed parameter WSN in the first stage. Potentially scintillating periods for every possible satellite are selected in the second stage as candidate times for estimating ionospheric irregularities.

Table 3.3. Multi-satellite scintillation periods generated and sorted by start time t_0, end time t_f and number of simultaneously scintillating satellites.

PRN	t_0	t_f	#
10,13,23	0403	0417	3
18,22,27	1302	1325	3

Table 3.4. Events to be examined in this dissertation.

PRN(s)	YEAR	DOY	t_0 [hh:mm:ss]	t_f [hh:mm:ss]	#
-	2013	342	-	-	A
23	2013	342	03:43:00	04:17:00	A1
23	2013	342	03:43:35	03:44:20	A2
10,13,23	2013	342	04:03:00	04:17:00	A3
-	2014	051	-	-	B
29	2014	051	11:20:00	11:57:00	B1
29	2014	051	11:44:45	11:45:29	B2
-	2015	076	-	-	C
18,22,27	2015	076	13:02:00	13:25:00	C1

CHAPTER 4

ESTIMATION OF PLASMA DRIFTS AND ANISOTROPY

Potential time periods acquired from the automated detection methods described in Chapter 3 are candidate periods for estimating properties of the scintillation-causing irregularities. The specific intervals identified in the tables in Chapter 3 are used in the analysis discussed in this chapter. First, the high-rate signal power and phase data for the time intervals in Table 3.4 are detrended and filtered with a series of post-processing routines summarized in Section 2.4.2. This chapter of the dissertation applies an algorithm of the spaced receiver technique summarized by [54] to cross-correlated receiver phase data from a GNSS array for the first time.

The technique was developed by [25] and was based on the following theoretical assumptions:

1. The region of the ionosphere where electron density irregularities exist can be represented by a thin horizontal slab with thickness L consistent with phase-screen scintillation model [10], as shown in Figure 4.1. The irregularity slab has a drift motion that remains constant, or "frozen in", throughout the slab.

2. The fluctuations in electron density δN within the layer is randomly distributed and produce a diffraction pattern that causes signal fluctuations received on the ground.

3. δN is correlated with random variations in received signal phase on the ground given by geometrical optics. The received trans-ionospheric signals $s_i, s_j, \ldots$ are stationary with zero mean and unit standard deviation [29].

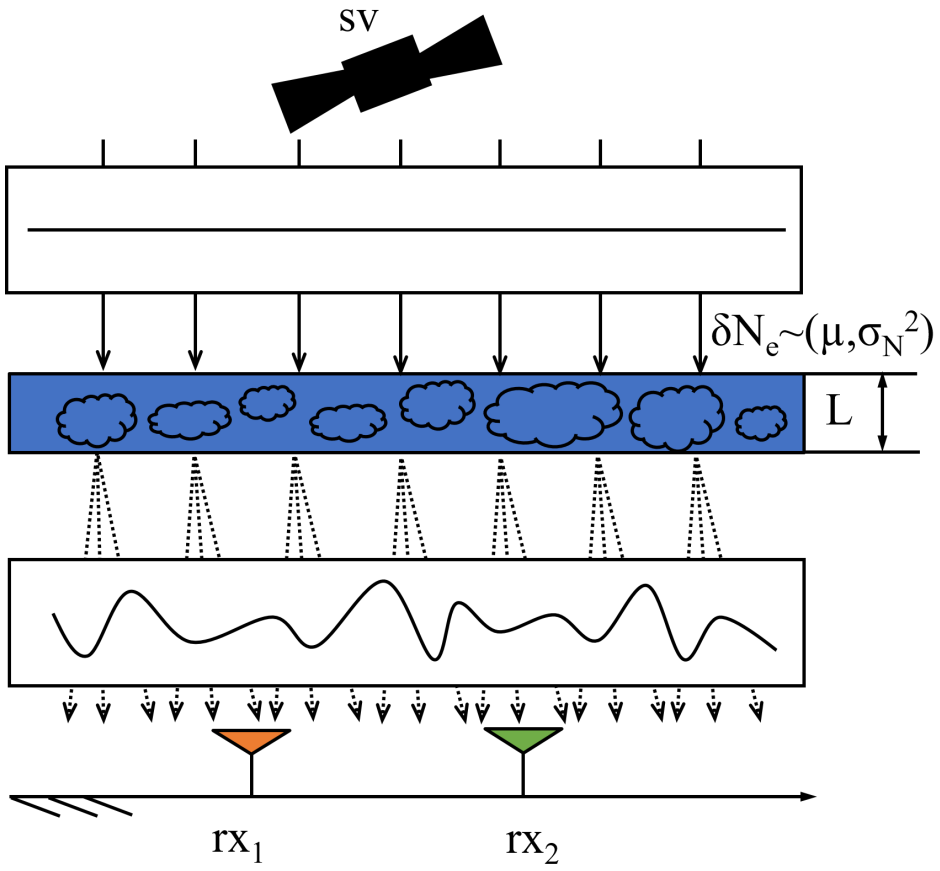

Figure 4.1. A radio signal transmitted from a satellite arrives at the ionosphere as a plane wave (arriving from zenith in this illustration). Due to the random sizes and distributions of irregularities, the plane wave emerges from the scattering layer as a distorted wave front. However, it is spatially and temporally correlated, having originated as a plane wave, and passed through a random scattering medium. These correlations are detectable by multiple receivers on the ground.

4. Cross-correlation functions $\rho_{ij}(\tau) = \langle s_i(t)s_j(t+\tau)\rangle$ for these signal pairs are all special cases of a single function R of spatial variables r_k for the kth spatial dimensions and temporal variable τ.

$$\rho = R\{ar_1^2 + \cdots + br_2^2 + c\tau^2\} \tag{4.1}$$

The argument of R is assumed positive definite to form an ellipse in one spatial dimension. This is supported by the phase screen model of irregularities as a random distribution. An example of this concept is shown for the case of one

spatial dimension in Figure 4.2.

5. R is a decreasing function of its argument normalized with $R\{\mathbf{0}\} = 1$ [29].

The properties of the diffraction pattern can be observed by examining signal correlations. For example, the drift motion of the irregularities can be observed on the ground using correlations of the received signals separated by a distance. However, there are a few subtleties in estimating the velocity. First, the random medium irregularities are evolving in time (e.g., ionizing and recombining). A characteristic velocity v_c quantifies this turbulence. The goodness of the "frozen-in" velocity assumption depends on the magnitude of this characteristic velocity. Secondly, if using only a one-dimensional array, considering peak time lag gives an "apparent velocity," not the true velocity of the drift. Finally, the original spaced-receiver methods consider geostationary satellites, so the motion of the diffraction pattern corresponds to the motion of the irregularities. For GNSS satellites which are moving with respect to the medium and the ground, the apparent velocity based on receiver cross-correlations will differ from the true velocity as well. Each of these will be treated in due time in the following sections.

4.1 One-Dimensional Spaced Receiver Technique

The one-dimensional spatial case of the technique is first introduced and then extended to two-dimensional scenario. Assuming the diffraction pattern is observed by a collinear array (i.e., aligned along one spatial dimension), a simplified interpretation of the spaced antenna technique can be applied. The equations from [2] are repeated here for clarity.

Suppose there are $n = 2$ nearby ground receivers that simultaneously receive signals $s_i(t), i = 1, 2$. According to previous assumptions, their correlations $\rho(\tau)$ are special cases of a surface $R(x, \tau)$ with $R(0, 0) = 1$, whose constant levels will take

shapes of concentric ellipses.

$$\rho = R\{a\,(x - v\tau)^2 + k\tau^2\} \tag{4.2}$$

$$= R\{ax^2 + 2hx\tau + b\tau^2\} \tag{4.3}$$

where

- x : 1D separation between the receiver pair
- τ : the time difference between two observations
- v : 1D true drift speed of the diffraction pattern
- a, h, b : parameters of the ellipse
- k : related to h, b

Figure 4.2 illustrates the surface posited for R as a function of x and τ. R is a decreasing function whose constant levels are the form of ellipses in the x-τ plane. An auto-correlation curve ρ_{ii} is the intersection of R with the plane $x = 0$. A cross-correlation curve ρ_{ij} for receivers i and j separated by distance ξ_c is the intersection of R with the plane $x = \xi_c$.

Figure 4.3 is a side view of Figure 4.2, looking down the x-axis at the $\tau - R$ plane. Figure 4.4 is a top view of Figure 4.2, looking down the R axis at the $x - \tau$ plane, showing only one ellipse.

As seen in Figure 4.3, the value of the cross-correlation peak $\rho_{ij} = \rho_m$ occurs at time τ_{cm}. A level curve ellipse of $R = \rho_m$ corresponds to this peak value, and can be seen in Figures 4.2 and 4.4. This ellipse also intersects the auto-correlation ρ_{ii} curve, at a time τ_{am}.

The time difference between two observations (receivers) is determined from the time shift τ_{cm} of the cross-correlation peak. Dividing the receiver separation

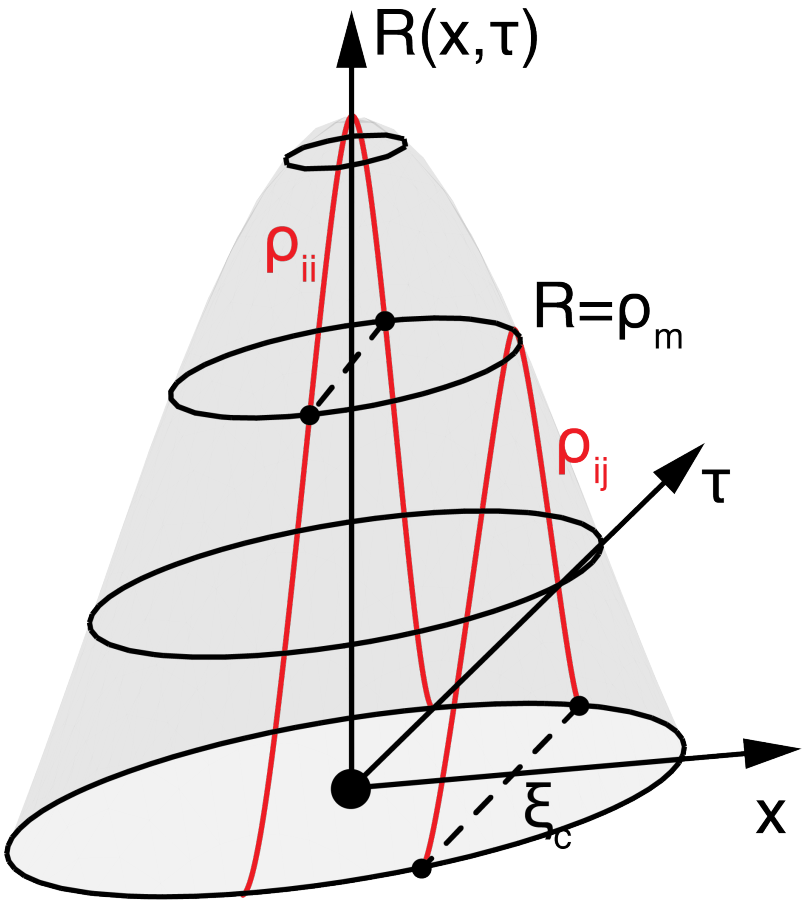

Figure 4.2. Ellipses of constant levels of $R(x,\tau)$ with $R(0,0) = 1$. ρ_{ii}, the auto-correlation curve, is the intersection of R with $x = 0$. ρ_{ij}, the cross-correlation curve for receivers i and j separated by distance ξ_c, is the intersection of R with $x = \xi_c$. Both ρ_{ii}, ρ_{ij} are slices of R that intersect the ellipse $R = \rho_m$, the cross-correlation maximum.

distance ξ_c by this time τ_{cm} gives an "apparent velocity" of the diffraction pattern as seen by the receiver pair. The point (ξ_c, τ_{cm}) is plotted on the ellipse in Figure 4.4. The apparent velocity v' is given by the inverse slope of the line to the point (ξ_c, τ_{cm}).

However, this apparent velocity is a function of the baseline distance (or more generally the geometry of the receiver spacing). For example, the ellipse intersects the x axis at some non-zero distance, but if one's receiver pair happened to have such a spacing, the time lag would appear to be 0, giving an apparent infinite velocity. This is non-physical of course. So the "true velocity" is defined as the speed at which

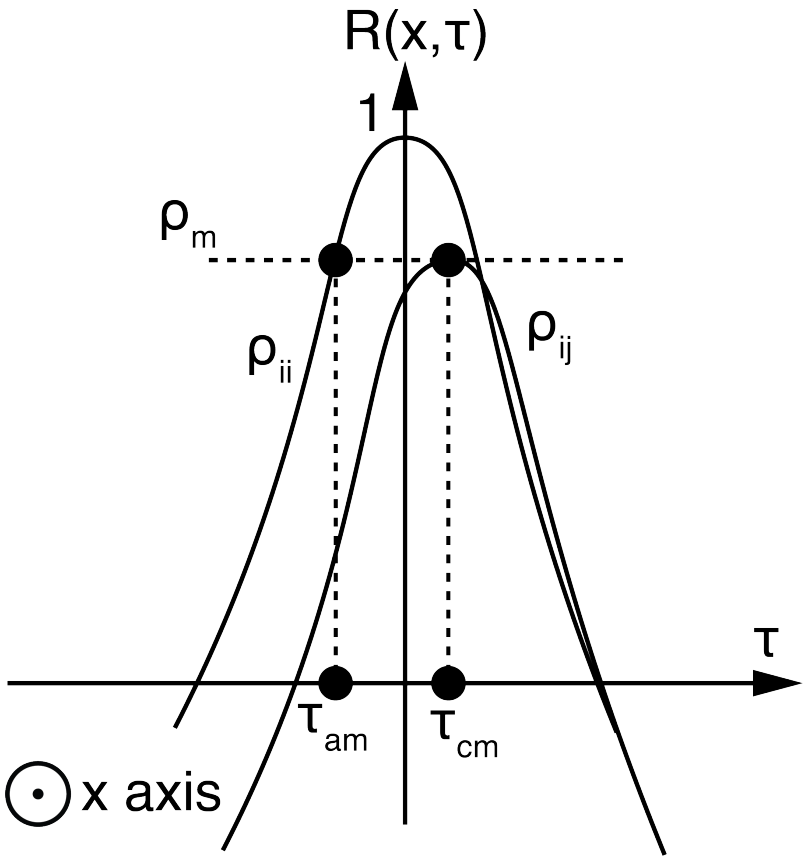

Figure 4.3. A projected view of Figure 4.2 along x-axis. In practice, $\rho_{ii}, \rho_{jj}, \rho_{ij}$ are normalized by the same factor $\sqrt{\max(\rho_{ii})\max(\rho_{jj})}$ to ensure that $\rho_{ii}(0) = R(0,0) = 1$. $\rho_{ij} = \rho_{ii} = \rho_m$ gives time delays τ_{cm}, τ_{am}.

the scintillation fading pattern evolves most slowly in time, i.e. is most nearly "frozen in".

Figure 4.4 illustrates the difference between the true and apparent velocities with the correlation surface $R = \rho_m$ only shown. Following along the contour $R = \rho_m$ from (ξ_c, τ_{cm}) to the point with the steepest slope (maximum τ for this ρ_m) gives the point (ξ_1, τ_1). The true velocity v is then given by the inverse slope of the line from the origin to (ξ_1, τ_1).

With straightforward geometrical arguments, these estimates are derived by [2] and summarized as follows:

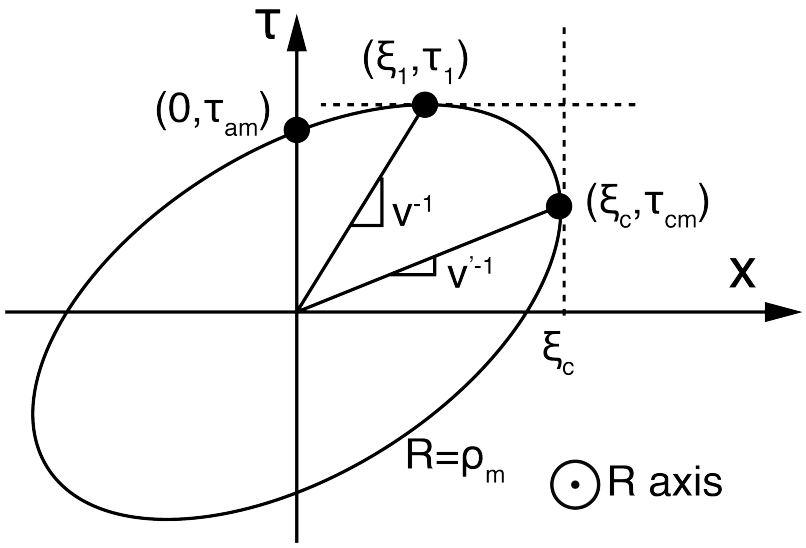

Figure 4.4. A projected view of Figure 4.2 along R axis. Only $R = \rho_m$ is shown.

$$v' = \xi_c/\tau_{cm} \tag{4.4}$$

$$v = \xi_1/\tau_1 = \frac{v'}{(1 + \tau_{am}/\tau_{cm})^2} \tag{4.5}$$

$$v_c = \sqrt{v(v' - v)} \tag{4.6}$$

where

- v' : apparent velocity of the drift pattern.
- v : true velocity with minimum rate of change in the pattern.
- v_c : rate of change of the drift pattern, or turbulent motion.

4.2 Application of One-Dimensional Case

To demonstrate the one-dimensional spaced receiver technique, an scintillation event during 01:22:12-01:22:58 on March 30, 2016 is identified with established routines in Chapter 3 and examined here using data collected from receivers E(east)

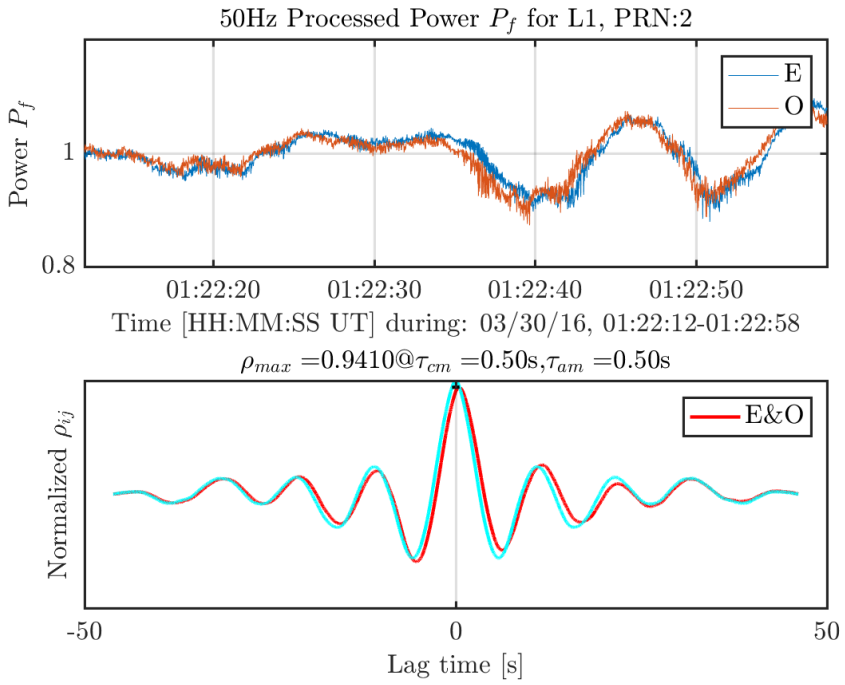

Figure 4.5. Top: 46 s time series of 50 Hz processed and filtered signal power for receiver pair E (blue) and O (red). Bottom: cross-correlation of the two signals in red. Auto-correlation of E is also plotted in cyan for reference. Note that the correlations are normalized to ensure $R\{\mathbf{0}\} = 1$.

and O(west) placed in Jicamarca Radio Observatory instead of SAGA. Figure 4.5 shows the processed power time series (top) and the corresponding cross-correlation of the two signals versus time lags (bottom). It further demonstrates that E is lagging while O is leading, implying that the diffraction pattern assumed to be moving eastwards along the baseline. If the baseline $\xi_c \approx 70$ m, the drift properties of the ground pattern can be roughly determined:

$$v' = \xi_c/\tau_{cm} \approx 70/0.5 \approx 140\,\mathrm{m/s} \tag{4.7}$$

$$v = \frac{v'}{1+(\tau_{am}/\tau_{cm})^2} \approx \frac{140}{1+(0.5/0.5)^2} \approx 70\,\mathrm{m/s} \tag{4.8}$$

$$v_c = \sqrt{v(v'-v)} \approx \sqrt{70(140-70)} \approx 70\,\mathrm{m/s} \tag{4.9}$$

4.3 Two-Dimensional Spaced Receiver Technique

This section reviews the general spaced receiver method in two dimensions, which is similarly derived from the same assumption and principle described in Section 4.1. For the 2D case, an illustrative R surface cannot be drawn, but the same concept applies. The constant level ellipses become concentric ellipsoids, as we will see. The equations from [31, 29] are provided here.

Suppose there are $n \geq 3$ nearby ground receivers that simultaneously receive trans-ionospheric phase signals $s_i(t), i = 1, 2, ..., n$ from a single GNSS satellite at a single frequency. Cross-correlation functions $\rho_{ij}(\tau) = \langle s_i(t) s_j(t+\tau) \rangle$ for receivers i and j are assumed to be special cases of a space-time correlation surface R. Its constant levels $\rho = R(x_{ij}, y_{ij}, \tau)$ are concentric ellipsoids, functions of a quadratic in one temporal τ and two spatial variables:

$$\rho_{ij} = R\{[a\,(x_{ij} - v_x\tau)^2 + 2h\,(x_{ij} - v_x\tau)\,(y_{ij} - v_y\tau) + b\,(y_{ij} - v_y\tau)^2] + k\tau^2\} \quad (4.10)$$

where

- R: normalized decreasing function with $R(0, 0, 0) = 1$
- x_{ij}, y_{ij}: horizontal baseline components between receiver i, j in local coordinates (e.g., east and north, respectively)
- τ : the time delay between two observations
- v_x, v_y: horizontal components of true drift $\vec{v} = v_x\hat{x} + v_y\hat{y}$
- a, h, b : second-degree-equation coefficients.

The terms in square brackets represent frozen-in motion of the irregularities and k describes the decorrelation in time due to turbulent motion. Rearranging Eq.

(4.10) we see that constant correlation levels take the shape of concentric ellipsoids in horizontal space and time (see Figure 4.6), provided $ab - h^2 > 0, a > 0, b > 0$:

$$\rho_{ij}(x_{ij}, y_{ij}, \tau) = R\{[ax_{ij}^2 + 2hx_{ij}y_{ij} + by_{ij}^2 + 2fx_{ij}\tau + 2gy_{ij}\tau + c\tau^2]\} \quad (4.11)$$

$$f = -(av_x + hv_y) \quad (4.12)$$

$$g = -(bv_y + hv_x) \quad (4.13)$$

$$c = av_x^2 + bv_y^2 + k + 2hv_xv_y \quad (4.14)$$

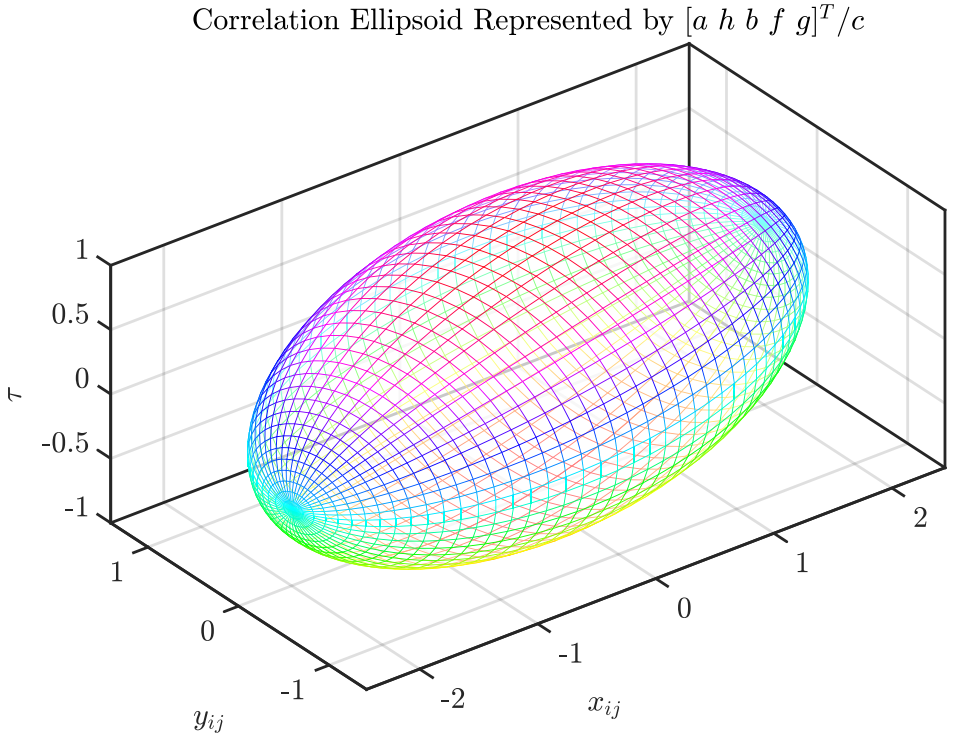

Figure 4.6. Ellipsoid in 2D space and time. The ellipsoid represents a surface of constant correlation value.

Putting $\tau = 0$ in Eq. (4.10) gives the ground projection of the constant-correlation ellipsoid , an ellipse whose shape and orientation are related to a, h, b (see Figure 4.7). The ellipse can be described by the axial ratio AR of its semi-major axis to semi-minor axis and the orientation angle of the semi-major axis Ψ_a measured

counter-clockwise from local east:

$$AR = \sqrt{\frac{1+(1-\alpha^2)^{1/2}}{1-(1-\alpha^2)^{1/2}}} \text{ with } \alpha = \frac{2\sqrt{ab-h^2}}{a+b} \tag{4.15}$$

$$\Psi_a = \frac{1}{2}\arctan\left(\frac{2h}{a-b}\right) \tag{4.16}$$

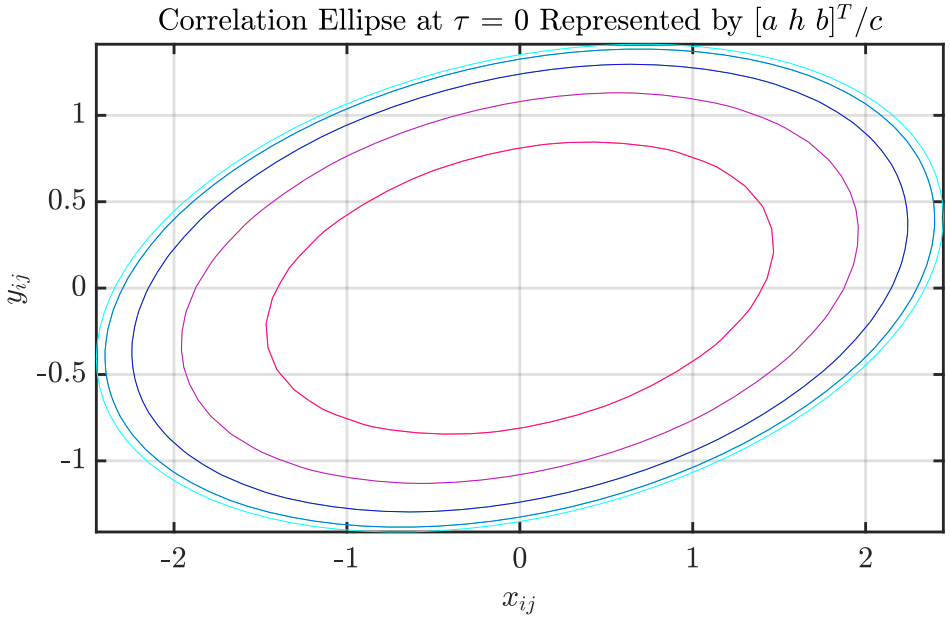

Figure 4.7. The projection of several ellipsoids, each corresponding to a different correlation value, onto the spatial dimensions gives concentric ellipses of constant correlation. The ellipses all have same axial ratio AR and orientation Ψ_a.

Magnitude ${}^d v^g = \sqrt{v_x^2 + v_y^2}$ and direction ${}^d\theta^g$ of the drift velocity of the phase screen with respect to the ground (indicated by the superscripts) are given by:

$${}^d v^g = \frac{\sqrt{(gh-fb)^2+(fh-ga)^2}}{ab-h^2} \tag{4.17}$$

$${}^d\theta^g = \arctan\left(\frac{fh-ga}{gh-fb}\right) \tag{4.18}$$

This chapter does not make distinctions between v, θ and ${}^d v^g, {}^d\theta^g$. In the following chapters, the satellite motion which also contributes to ground drifts will be considered such that v, θ and ${}^d v^g, {}^d\theta^g$ are no longer interchangeable.

The drift velocity represents the bulk movement of the diffraction pattern due to "frozen-in" irregularities. Temporal variation due to internal turbulent motion is described by a characteristic velocity v_c, given by [55] for conditions in which axial ratio is not large:

$$\left(\frac{v_c}{{}_d v^g}\right)^2 = \frac{c(a^3 + 2ah^2 + bh^2)}{(hg + af)^2} - 1 \tag{4.19}$$

In effect, estimates of a, h, b, f, g yield the properties in Eqs. (4.15)-(4.19) of the resulting phase received at the ground due to ionospheric irregularities. To make estimates from Eq. (4.10), the correlation between the receiver pair i, j at time delay τ_c has value $\rho_{ij}(\tau_c)$. For auto-correlation ρ_{ii}, the x_{ij} and y_{ij} in Eq. (4.10) vanish, leaving:

$$\rho_{ii}(\tau) = R\{[c\tau^2]\} \tag{4.20}$$

Then equating the auto-correlation and cross-correlation curves in Eqs. (4.20) and (4.10) for receivers i and j gives a function of the ellipsoid parameters $[a, h, b, f, g]/c$ that can be solved:

$$\rho_{ii}(\tau_a) = \rho_{ij}(\tau_c) \tag{4.21}$$

$$\tau_a^2 - \tau_c^2 = \left[ax_{ij}^2 + 2hx_{ij}y_{ij} + by_{ij}^2 + 2fx_{ij}\tau_c + 2gy_{ij}\tau_c\right]/c \tag{4.22}$$

The values τ_a, τ_c come from the auto-correlation ρ_{ii} and cross-correlation ρ_{ij} curves respectively. According to Figure 4.8, for a given τ_c on the cross-correlation curve between receivers i and j, the corresponding τ_a is found as:

$$\tau_a = \arg\min_{\tau_a} \left(|\rho_{ij}(\tau_c) - \rho_{ii}(\tau_a)|\right) \tag{4.23}$$

One other difference between the 1-D and 2-D cases is that the 2D algorithm makes use of multiple correlation values and corresponding time delays on the main

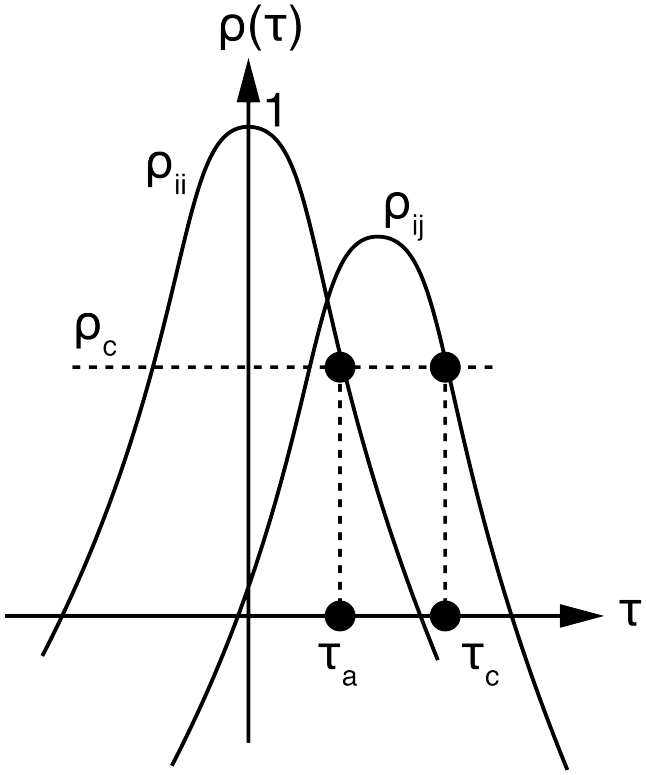

Figure 4.8. Cross-correlation ρ_{ij} and auto-correlation ρ_{ii} and corresponding time delays τ_c, τ_a at a given value $\rho_c = \rho_{ij}(\tau_c) = \rho_{ii}(\tau_a)$.

lobe (down to some cutoff value, usually about $\rho_{\text{cutoff}} = 0.65$), while the 1-D case takes only the correlation maximum.

A set of observations $\mathbf{y}$ can be assembled from the auto- and cross-correlation curves of all possible pairs of receivers as:

$$\mathbf{y} = \begin{bmatrix} y_1 \\ y_2 \\ \vdots \\ y_M \end{bmatrix} = \begin{bmatrix} \tau_a(1)^2 - \tau_c(1)^2 \\ \tau_a(2)^2 - \tau_c(2)^2 \\ \vdots \\ \tau_a(m)^2 - \tau_c(m)^2 \\ \vdots \\ \tau_a(M)^2 - \tau_c(M)^2 \end{bmatrix} \tag{4.24}$$

The M elements of $\mathbf{y}$ for all pairs i, j of receivers counts all τ_c whose $\rho_{ij}(\tau_c) > \rho_{\text{cutoff}}$, on the right half of the main lobe (typically $\rho_{\text{cutoff}} = 0.65$).

These observations $\mathbf{y}$ are a linear function of state $\mathbf{x} = (1/c)[a, h, b, f, g]^T$ whose solution can be found from linear inversion:

$$\mathbf{y} = \mathbf{H}\mathbf{x} + \nu \tag{4.25}$$

$$\mathbf{x} = (\mathbf{H^T W H})^{-1}\mathbf{H^T W y} \tag{4.26}$$

The mapping matrix $\mathbf{H}$ is given by Eq. (4.22), ν is unknown noise, and $\mathbf{W}$ is a weighting matrix (the identity in this work). After solving for the unknown state $\mathbf{x}$ with the least squares method, the anisotropy AR, Ψ_a of the ground phase screen, horizontal drift velocity ${}^d v^g$, and characteristic velocity v_c of the ionospheric irregularity layer can be estimated using the nonlinear relationships in Eqs. (4.15)-(4.19).

4.4 Application to Single-Satellite Event B1,B2

This section presents a case study applying the two-dimensional spaced-receiver method to correlated SAGA 100Hz scintillating receiver signals for a single satellite. Properties of the ionospheric diffraction ground pattern ${}^d v^g, {}^d \theta^g, v_c, AR, \Psi_a$ are estimated with methods reviewed in Section 4.3.

This date is chosen because there is a 37 minute interval found by automated detection (refer to Table 3.1 and 3.4), and it was one of the more geomagnetically active days. The whole time series of signal phase in question has been undergone post-processing routines reviewed in Section 2.4.2 and is shown in Figure 4.9.

It should be realized that neither the power or phase is continuous throughout the whole period for any operational receiver. Prior to cross-correlation analysis, time discontinuities are identified to determine time-continuous overlaps $\vec{t_i} = (t_{0i}, t_{fi})$ across all receiver data by the algorithm developed in in Figure 3.7. Another routine

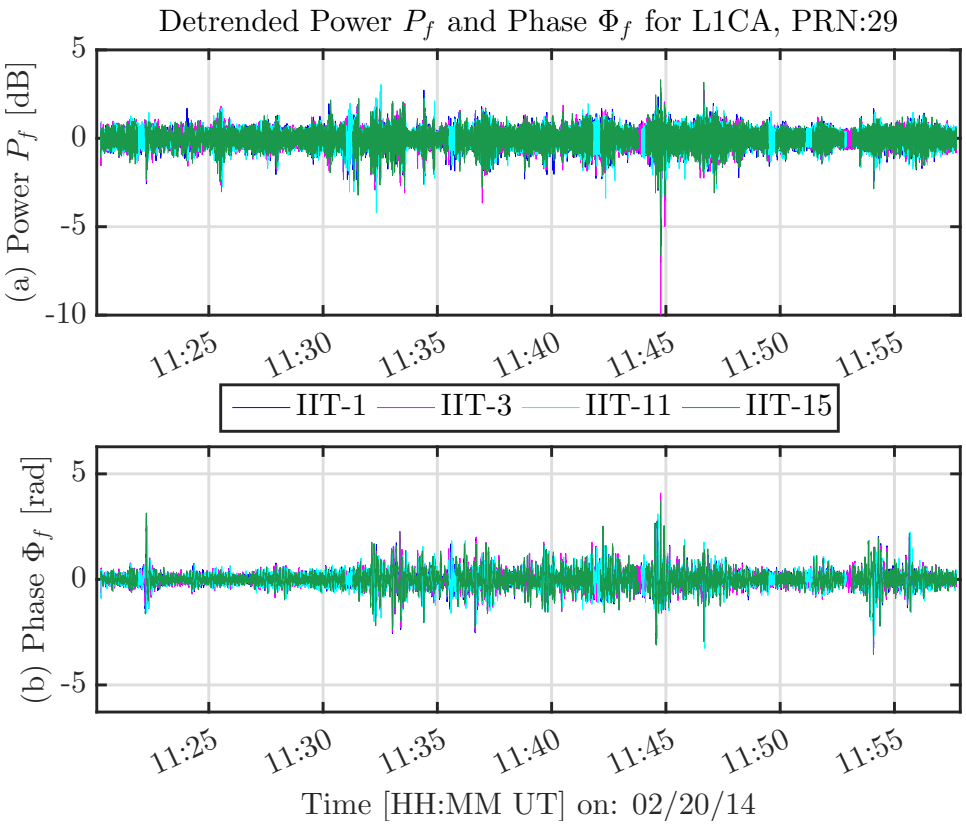

Figure 4.9. 100 Hz detrended and filtered (a) power and (b) phase for PRN 29 during 1120-1157 UT, 20 Feb 2014 (event B1). Signal data from operational receivers are color scaled according to Figure 2.9.

refines the resulting periods $\vec{t_i}$ to segments with a user-defined trigger T (10 s or 30 s in this dissertation). Shorter estimation time might sense the temporal variation in two consecutive estimations, but a longer one might yield more precise estimates with more observations. The sensitivity to signal length T of resulting estimates is examined in Section 5.2. Such routine is described as follows:

$$\vec{t_i} = \begin{cases} (0,0), & \text{if } |\vec{t_i}| < T \\ \vec{t_i}, & \text{if } T \leq |\vec{t_i}| < 60s \\ \vec{t_{i1}} + \vec{t_{i2}} + \ldots + \vec{t_{in}}, |\vec{t_{i1}}| = |\vec{t_{i2}}| = \ldots = |\vec{t_{in}}|, & \text{if } |\vec{t_i}| \geq 60s \end{cases} \tag{4.27}$$

To effectively demonstrate the spaced-receiver method, a single time segment of 100 Hz power and phase data derived from the above routine is chosen, corre-

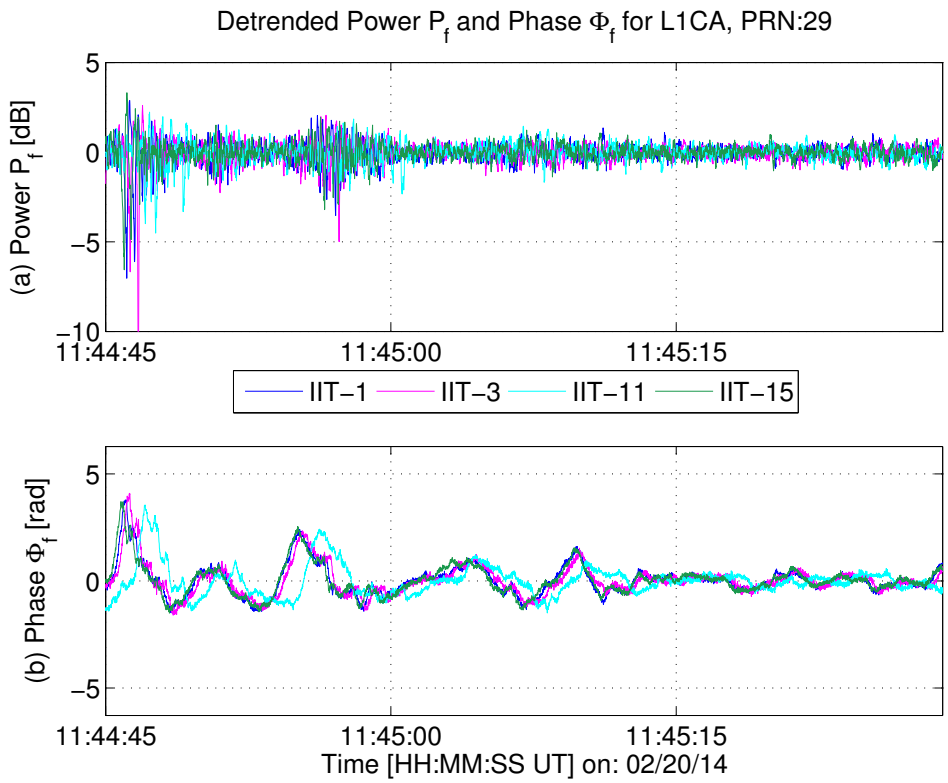

Figure 4.10. 100 Hz detrended and filtered (a) power and (b) phase for PRN 29 during 2685-2729 s after 1100UT, 20 Feb 2014 (event B2)

sponding to the interval including the highest σ_Φ values around 1145 UT. Figure 4.10 shows a 44 s time series of detrended, filtered power in decibels and phase in radians at 100 Hz, for each receiver operating that day. It is observed that inter-receiver phase measurements display similar structure and are therefore temporally correlated.

Figure 4.11 shows all pairs of cross-correlations for the phase time series of Figure 4.9(b) with $T = 30$ s. The peak cross-correlation value and the time lag at which it occurs is labeled for each correlation curve. One can refer to Figure 2.9 for the connection between spatial and temporal correlation given the proximity of the receivers.

4.4.1 Sensitivity of SAGA estimates to correlation cut-off. To test the lowest correlation values that could be realistically used, estimates $v, \theta, AR, \Psi_a, v_c/v$

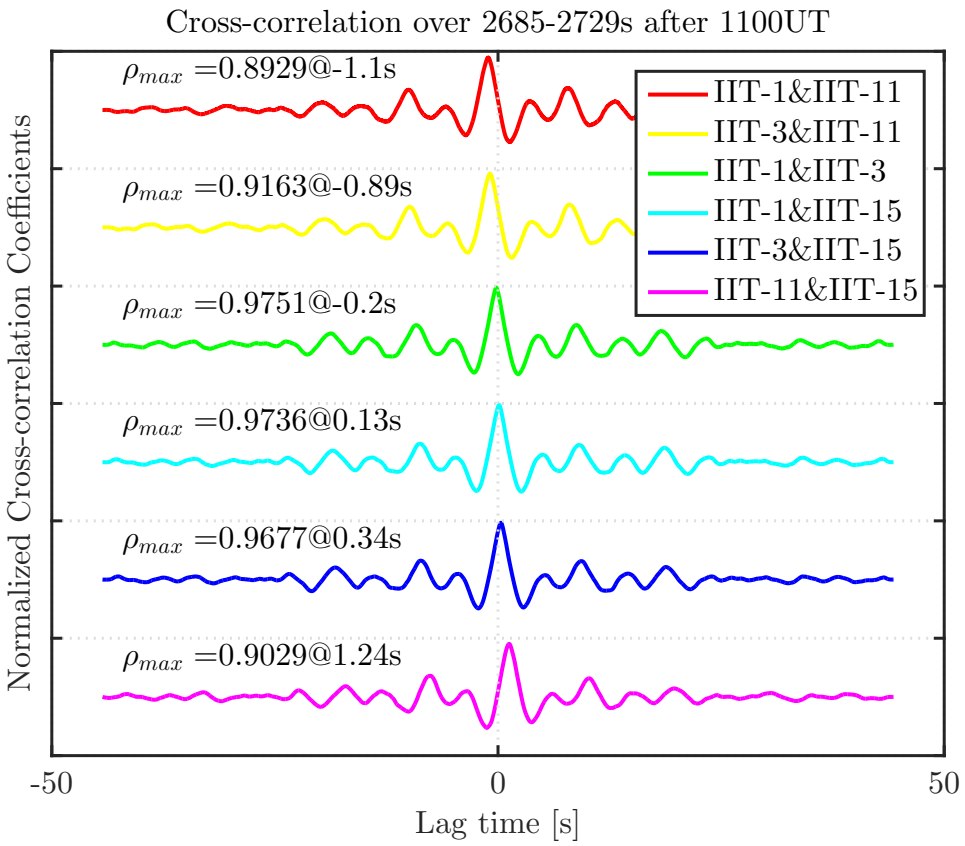

Figure 4.11. Pairwise cross-correlations in phase from PRN 29 during 2685-2729 s after 1100 UT, 20 Feb 2014 (event B2).

as a function of correlation cut-offs ρ_{cutoff} are examined. The sensitivity of drift estimates to cut-off ρ_{cutoff} is discussed as follows, shown in Figure 4.12. Drift and anisotropy estimates are made for event B2 in Figure 4.10. Cross-correlation values $\rho_{ij}(\tau)$ below the cut-off are discarded.

It can observed that spaced receiver estimates cannot be expressed as a monotonic function of cut-off ρ_{cutoff}. Furthermore, the relationship between estimates and the threshold varies from one time segment of estimation (event B2) to another (not shown). Drifts from highly correlated data might interpret the motion of the ground pattern more precisely. Although a higher cut-off removes less-correlated measurements, it considers fewer available information from cross-correlation. A balance is desirable between the correlation threshold and number of measurements. Since it is

hard to quantify this balance, an universal threshold is applied for every continuous time period.

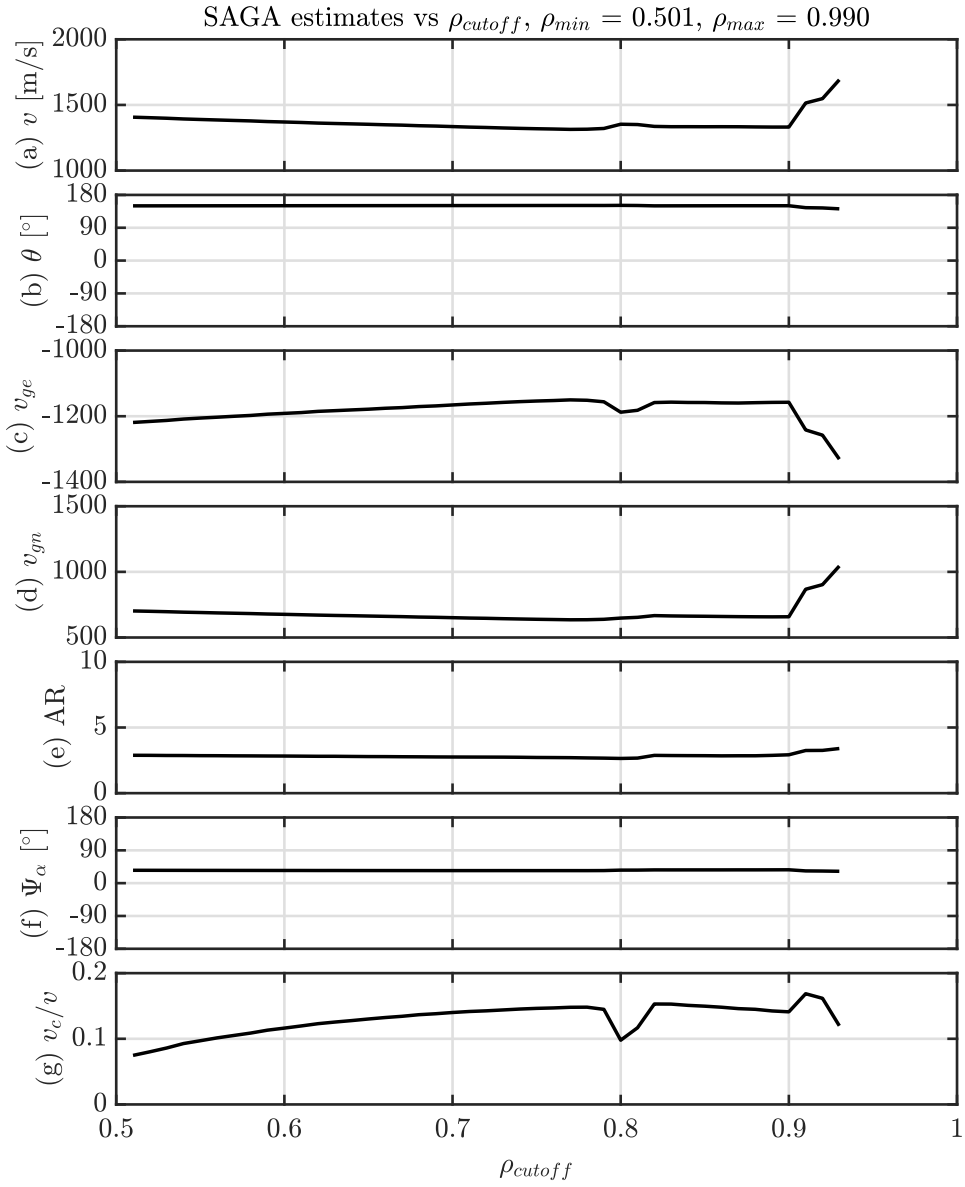

Figure 4.12. SAGA estimates as function of ρ_{cutoff} for event B2.

The correlation peaks in Figure 4.11 are sufficiently high; analysis detailed in Section 4.3 are applied, using the main peak of the cross-correlation curves down to $\rho_{\text{cutoff}} = 0.65$. The over-determined system described in Sect. 4.3 is constructed with time delay measurements taken from correlation functions. Least-squares estimations

are performed to solve for the coefficients a, b, f, g, h and thus axial ratio, orientation, speed, and direction as given in Eqs. (4.15) and (4.16)-(4.18). For event B2, a horizontal drift of $v \approx 1400$ m/s and $\theta \approx -50°$ (southeastward) is estimated. Although not shown, the method could be repeated for the SAGA phase observations of PRN 29 for the whole 37-minute long event B1 in Figure 4.9. The time series data are segmented according to Eq (4.27), to estimate drift speed and correlation anisotropy for the two-dimensional ground phase screen.

4.5 Automated Drift and Anisotropy Estimation

The automated detection routine in Chapter 3 selects scintillation index σ_Φ measured by SAGA from December 2013 through November 2014 to generate a list of top 20 active days in Table 3.1, as determined by the WSN metric in Eq. (3.1).

The dynamic threshold th_{dyn} used for detection on that day is given as daily mean σ_Φ. These columns correspond to Stage 1 of automated scintillation detection. There is generally significant geomagnetic activity, and the mean σ_Φ values on these dates, ranging from 0.3 to 0.5 rad exceed the annual mean of 0.22 rad.

The columns PRN, t_0, and Δt correspond to the results of Stage 2 scintillation detection. For each day, only the satellite with the largest average σ_Φ is listed. For example, only PRN 29 with a mean of 0.93 rad is shown for DOY 051 (not PRNs 31, 24 and 12, which were also scintillating as seen on Figs. 2.12-2.13). The start time t_0 of the continuous scintillation interval detected and the duration Δt for that PRN are listed.

Just as the 44 s event B2 in Section 4.4 is discussed and then extended for longer event event B1 on the same day, spaced-receiver analysis are applied to all the active days listed in Table 3.1.Since estimates may sometimes contain nonphysical outliers during the time interval, we use the median value to summarize the results.

Table 4.1 shows median horizontal drifts, $\tilde{v}, \tilde{\theta}$ during the scintillation of the given satellite. It also lists the median ratio of characteristic velocity v_c to v, the axial ratio $\tilde{AR}$, and the ellipse orientation angle $\tilde{\Psi}_a$. Note that only the most significant single-satellite event is chosen from each of these active days for demonstration.

"N/A" is listed when an estimate could not be made, because: there were no intervals of at least 30 s duration in which all the receivers had continuous 100 Hz data; the correlation peak was lower than the correlation cutoff ρ_{cutoff}; or the estimates of a, b, h violated the assumption of an ellipsoid. The "N/A" entries tend to happen for short detected time intervals of only 2-3 minutes. "NaN" is listed for the characteristic to true velocity ratio when the ratio exceeds 1, i.e. $v_c > v$.

The table shows that speeds tend to range from 0 to 2500 m/s, which may be realistic drift speeds, although there are a couple of speeds much higher that are clearly not realistic. For DOY 291, the speed of 11517 m/s is likely nonphysical. Drift directions are measured in all but the southwestward quadrant direction ($\theta < -90°$). This may be because the receivers are sited with one baseline oriented northwest-to-southeast much longer than the others, so there is less observability of motion perpendicular to the baseline. Characteristic velocities range from smaller-than to comparable-to the drift velocity. According to theory, v_c should be significantly less than v for the frozen-in irregularity model to hold. In the case of $v_c > v$, the frozen-in assumption is likely violated, so the drift estimate may be suspect.

Axial ratios tend to be ≤ 6 with a couple of exceptions. Possible ellipse orientation angles range from 0 to 180°, and the measured values are about 20° to 160° spanning almost this entire range. In this case, the ellipse orientation does not appear to be sensitive to receiver baselines.

4.6 Summary

Table 4.1. Top 20 active days December 2013 to December 2014, and SAGA estimates of horizontal drift velocity, characteristic velocity, and correlation ellipse shape and orientation. For each day, only the PRN with most significant scintillation is shown.

YEAR	DOY	WSN	th_{dyn} [rad]	max Kp	max AE [nT]	PRN	t_0 UT [hhmm]	Δt [min]	$\tilde{v}$ [m/s]	$\tilde{\theta}$ [°]	$\tilde{v_c}/v$	$\tilde{AR}$	$\tilde{\Psi}_a$ [°]
2013	**342**	**755**	**0.3667**	**6**	**736**	**23**	**0343**	**34**	**1458**	**125**	**0.28**	**9**	**62**
2014	050	1070	0.4611	6	1198	17	0526	14	1892	148	0.44	8	41
2014	**051**	**875**	**0.4047**	**6**	**1236**	**29**	**1120**	**37**	**952**	**-63**	**0.27**	**4**	**110**
2014	052	802	0.3292	3	552	29	1120	15	1008	-45	0.32	3	164
2014	054	840	0.3818	4	1098	14	1942	15	1908	124	0.36	3	118
2014	058	795	0.3518	5	822	30	2059	74	1754	95	0.30	8	118
2014	102	973	0.4307	5	773	12	0501	49	2407	145	0.28	3	51
2014	120	1118	0.4822	4	1004	12	0400	17	1265	140	0.19	3	25
2014	239	1118	0.5164	4	1075	30	1321	15	978	-35	0.17	3	159
2014	240	801	0.3848	5	861	20	0724	10	7803	119	0.76	4	18
2014	255	759	0.3554	6	1021	2	0923	21	875	-37	0.81	22	53
2014	267	859	0.3685	4	872	8	0839	11	3011	124	0.56	6	64
2014	270	788	0.3381	4	708	8	0928	23	2557	13	0.63	5	58
2014	273	754	0.3210	4	639	13	0930	12	1802	-83	0.75	3	59
2014	282	1012	0.4033	4	645	8	0912	10	1495	-53	0.75	6	116
2014	291	833	0.3348	4	654	8	0829	13	11517	-9	0.64	5	53
2014	293	1057	0.4431	5	1271	6	1602	14	2647	66	0.81	5	61
2014	294	755	0.3193	4	735	9	0857	12	2167	51	0.72	6	41
2014	308	898	0.3875	5	856	24	1346	11	1025	-45	0.54	3	124
2014	314	881	0.4911	4	714	28	1020	10	1220	-75	0.42	8	65

This chapter presents the theory and implementation for estimating ionospheric drift and anisotropy. Techniques for post-processing high-rate measurements during interesting periods are reviewed. One-dimensional case and two-dimensional case of the spaced-receiver technique has been reviewed. For demonstration, the 1-D case is applied to two receivers at Jicamarca Radio Observatory to estimate the spatial-temporal correlation between scintillating receiver signal power pair. Using a single-satellite case study, two-dimensional case of spaced antenna technique is then applied to SAGA to estimate properties of the diffraction pattern. The sensitivity of correlation cut-off has been discussed. With the automated routine developed in the previous chapter, the estimation analysis is extended to detected scintillation events from a list of scintillating days in 2014.

CHAPTER 5

ERROR ANALYSIS OF IRREGULARITY ESTIMATES

In the previous chapter, it has been demonstrated that the scintillation statistics and properties of diffraction pattern of the irregularities can be automatically monitored and analyzed. However, the uncertainties on ionospheric estimates derived should be examined for further evaluation. Analytic error analysis of space-receiver estimates have been studied in the previous studies [56] but the method is derived with simulated data at lower frequency bands. This chapter takes an alternative approach to quantify uncertainties on the estimates

5.1 Error Analysis of SAGA Estimates

To quantify the uncertainties on the measurements, a Monte Carlo simulation of noise is used for each signal, to provide a covariance matrix of the observations $\mathbf{y}$ in Eq. (4.24). These covariances are then propagated through linear system theory to error covariances on the quantities of interest, specifically in this work, the drift speed v and direction θ.

An ensemble of N sets of noise-added signals received by the array from a single satellite are simulated. To generate the n^{th} ensemble member, random white Gaussian noise ν is introduced to the detrended, filtered receiver signals $s_i(t)$ and $s_j(t)$ from receivers i and j:

$$\tilde{s}_i(t) = s_i(t) + \nu(t) \tag{5.1}$$

$$\tilde{s}_j(t) = s_j(t) + \nu(t) \tag{5.2}$$

$$\tilde{\rho}_{ij}(\tau) = \langle \tilde{s}_i(t)\tilde{s}_j(t+\tau) \rangle \tag{5.3}$$

where $\nu \sim \mathcal{N}(0, \sigma_\nu^2)$.

The observation matrix of the original signal is constructed as defined in Eq. (4.22). A noisy observation $\mathbf{y_n}$ for ensemble member n is constructed using the noisy cross-correlation values $\tilde{\rho}_{ij}$:

$$\mathbf{y_n} = \left[\tilde{\tau}_a(1)^2 - \tau_c(1)^2, \quad \tilde{\tau}_a(2)^2 - \tau_c(2)^2, \quad \ldots, \quad \tilde{\tau}_a(M)^2 - \tau_c(M)^2\right]^{\mathbf{T}} \tag{5.4}$$

Note that τ_c remains the same in both the original and noise-free observations because the noise has been added to signal s, not to the times t. For each ensemble member n, we create an array of these noisy observations $\mathbf{y_n}$, which can be arranged into a column matrix of the form

$$\tilde{\mathbf{Y}} = \left[\mathbf{y_1} \quad \mathbf{y_2} \quad \cdots \quad \mathbf{y_n} \quad \cdots \quad \mathbf{y_N}\right] \tag{5.5}$$

$$= \mathbf{H}\tilde{\mathbf{X}} = \mathbf{H}\left[\mathbf{x_1} \quad \mathbf{x_2} \quad \cdots \quad \mathbf{x_n} \quad \cdots \quad \mathbf{x_N}\right] \tag{5.6}$$

This matrix $\tilde{\mathbf{Y}}$ has dimension $M \times N$, where M is the number of cross-correlation times τ_c whose cross-correlation values exceed the threshold ρ_{cutoff} chosen, and N is the number of ensemble members in the simulation. Each column corresponds to one ensemble member, and each row corresponds to the ensemble of values $\tilde{\tau}_a^2 - \tau_c^2$ for a single τ_c. The columns $\mathbf{x}_n$ of $\tilde{\mathbf{X}}$ are the estimates of the $(a, b, f, g, h)/c$ for each of the simulations, with least-squares solution:

$$\tilde{\mathbf{X}} = (\mathbf{H^T W H})^{-1}\mathbf{H^T W}\tilde{\mathbf{Y}} \tag{5.7}$$

Not every ensemble member solution successfully produces estimates. Data segments may not have a sufficiently high cross-correlation peak to compute the estimation, i.e., $\max(\rho_{ij}) < \rho_{\text{cutoff}}$. Other estimates may be invalidated by coefficients that do not correspond to an ellipse, i.e., $ab - h^2 < 0, a < 0, b < 0$. Such estimates are discarded, leaving a total of $K \leq N$ valid estimates. The ensemble observations

$\mathbf{y}_k$ that produce valid estimates $\mathbf{x}_k$ are arranged as columns in $\hat{\mathbf{Y}}$.

$$\hat{\mathbf{Y}} = \begin{bmatrix} \mathbf{y_1} & \mathbf{y_2} & \cdots & \mathbf{y}_k & \cdots & \mathbf{y}_K \end{bmatrix} \tag{5.8}$$

$$= \begin{bmatrix} \hat{\mathbf{y}}_\mathbf{1} \\ \hat{\mathbf{y}}_\mathbf{2} \\ \vdots \\ \hat{\mathbf{y}}_\mathbf{m} \\ \vdots \\ \hat{\mathbf{y}}_\mathbf{M} \end{bmatrix} \tag{5.9}$$

When $\hat{\mathbf{Y}}$ is written as a matrix of row vectors, each row $\hat{\mathbf{y}}_\mathbf{k}$ corresponds to the ensemble values $\tilde{\tau}_a^2 - \tau_c^2$ for a single τ_c, including only those ensemble members which produce estimates of the state satisfying $ab - h^2 > 0, a > 0, b > 0$. From these ensemble members, we compute the covariance $\mathbf{\Sigma}_{\hat{\mathbf{Y}}}$ whose element σ_{ij}^2 is:

$$\sigma_{ij}^2 = \mathbf{E}[(\hat{\mathbf{y}}_\mathbf{i} - \bar{\hat{\mathbf{y}}}_\mathbf{i})(\hat{\mathbf{y}}_\mathbf{j} - \bar{\hat{\mathbf{y}}}_\mathbf{j})^\mathbf{T}], i, j \leq M \tag{5.10}$$

where the overbar refers to the mean value of that quantity, over all valid ensemble members.

The estimated state $\hat{\mathbf{x}}$ and covariance $\mathbf{\Sigma}_{\hat{\mathbf{x}}}$ is

$$\hat{\mathbf{x}} = \frac{1}{K} \sum_k^K \mathbf{x}_k, K \leq N \tag{5.11}$$

$$\mathbf{\Sigma}_{\hat{\mathbf{x}}} = (\mathbf{H^T W H})^{-1} \mathbf{H^T W} \mathbf{\Sigma}_{\hat{\mathbf{Y}}} \mathbf{W^T H} (\mathbf{H^T W^T H})^{-1} \tag{5.12}$$

To propagate the errors $\mathbf{\Sigma}_{\hat{\mathbf{x}}}$ on $\hat{\mathbf{x}}$ to drift motions, we linearize the equations

(4.17)-(4.18) about the expected state $\hat{x}$, making Jacobian matrix $\mathbf{J_1}$:

$$\begin{bmatrix} {}^{d}v_e^g \\ {}^{d}v_n^g \\ {}^{d}v_c^g \\ AR \\ \Psi_a \end{bmatrix} \approx \underbrace{\begin{bmatrix} \frac{\partial {}^{d}v_e^g}{\partial \hat{a}} & \dots & \frac{\partial {}^{d}v_e^g}{\partial \hat{g}} \\ \vdots & \dots & \vdots \\ \frac{\partial \Psi_a}{\partial \hat{a}} & \dots & \frac{\partial \Psi_a}{\partial \hat{g}} \end{bmatrix}}_{\mathbf{J_1}} \hat{\mathbf{x}} \tag{5.13}$$

$$\mathbf{{}^{d}v^{g}} = \underbrace{\begin{bmatrix} 1 & 0 & 0 & 0 & 0 \\ 0 & 1 & 0 & 0 & 0 \end{bmatrix}}_{\mathbf{G_1}} \mathbf{J_1}\hat{\mathbf{x}} \tag{5.14}$$

$$\mathbf{\Sigma_{{}^{d}v^{g}}} = \begin{bmatrix} ({}^{d}\sigma_n^g)^2 & {}^{d}\sigma_{en}^g \\ {}^{d}\sigma_{en}^g & ({}^{d}\sigma_n^g)^2 \end{bmatrix} = \mathbf{G_1 J_1 \Sigma_{\hat{x}} (G_1 J_1)^T} \tag{5.15}$$

In these arrays, ${}^{d}v_e^g = v_x$ and ${}^{d}v_n^g = v_y$ from Eqs. (4.12)-(4.13), and ${}^{d}v_c^g = v_c$ from Eq. (4.19). $\mathbf{G_1}$ is an element selection matrix. The pre-superscript "d" indicates the diffraction pattern drift, and the post-superscript "g" indicates this is with respect to the ground. Subscripts "e" and "n" indicate local east and north components.

In contrast to spaced receiver studies involving geostationary links, the GNSS satellites are moving with respect to the ground. The estimated satellite motion at the ionospheric pierce point (IPP) with respect to the ground is the horizontal velocity $\mathbf{{}^{ipp}v^{g}} = [{}^{ipp}v_e^g, {}^{ipp}v_n^g]^{\mathbf{T}}$, assuming the altitude of the IPP to be 250 km. The derivation of $\mathbf{{}^{ipp}v^{g}}$ is detailed in Appendix A.

$$\begin{bmatrix} {}^{d}v_e^{ipp} \\ {}^{d}v_n^{ipp} \end{bmatrix} = \underbrace{\begin{bmatrix} 1 & 0 & -1 & 0 \\ 0 & 1 & 0 & -1 \end{bmatrix}}_{\mathbf{D}} \underbrace{\begin{bmatrix} \mathbf{{}^{d}v^{g}} \\ \mathbf{{}^{ipp}v^{g}} \end{bmatrix}}_{\mathbf{v^g}} \tag{5.16}$$

A differencing matrix $\mathbf{D}$ subtracts off the motion of the raypath, to give the drift motion of the irregularities themselves $\mathbf{^{d}v^{ipp}} = [{}^{d}v_e^{ipp}, {}^{d}v_n^{ipp}]^{\mathbf{T}}$ with respect to the frame of the IPP, in which the pierce point motion is 0. Next we take the components of horizontal drift velocity and express them as speed and direction. This will enable comparison to PFISR measurements of drift speed and direction. Again linearizing about the expected value to obtain $\mathbf{J_2}$:

$$\begin{bmatrix} {}^{d}v^{ipp} \\ {}^{d}\theta^{ipp} \end{bmatrix} = \begin{bmatrix} \sqrt{{}^{d}v_e^{ipp\,2} + {}^{d}v_n^{ipp\,2}} \\ \arctan\left(\frac{{}^{d}v_n^{ipp}}{{}^{d}v_e^{ipp}}\right) \end{bmatrix} \tag{5.17}$$

$$\approx \underbrace{\begin{bmatrix} \frac{\partial {}^{d}v^{ipp}}{\partial {}^{d}v_e^{ipp}} & \frac{\partial {}^{d}v^{ipp}}{\partial {}^{d}v_n^{ipp}} \\ \frac{\partial {}^{d}\theta^{ipp}}{\partial {}^{d}v_e^{ipp}} & \frac{\partial {}^{d}\theta^{ipp}}{\partial {}^{d}v_n^{ipp}} \end{bmatrix}}_{\mathbf{J_2}} \begin{bmatrix} {}^{d}v_e^{ipp} \\ {}^{d}v_n^{ipp} \end{bmatrix} \tag{5.18}$$

$$= \mathbf{J_2 D v^g} \tag{5.19}$$

$$\mathbf{\Sigma}_{v,\theta} = \begin{bmatrix} \sigma_v^2 & \sigma_{\theta v} \\ \sigma_{\theta v} & \sigma_\theta^2 \end{bmatrix} = \mathbf{J_2 D} \overbrace{\begin{bmatrix} \mathbf{\Sigma_{d_{vg}}} & 0 \\ 0 & \mathbf{\Sigma_{ipp_{vg}}} \end{bmatrix}}^{\mathbf{\Sigma_{vg}}} (\mathbf{J_2 D})^{\mathbf{T}} \tag{5.20}$$

$$\mathbf{\Sigma_{ipp_{vg}}} = \begin{bmatrix} ({}^{ipp}v_e^g)^2 & \cancelto{0}{({}^{ipp}v_{en}^g)^2} \\ \cancelto{0}{({}^{ipp}v_{en}^g)^2} & ({}^{ipp}v_n^g)^2 \end{bmatrix} \tag{5.21}$$

The covariance matrix $\mathbf{\Sigma_{vg}}$ on the righthand side is assumed to be block diagonal since satellite/IPP motions $\mathbf{\Sigma_{ipp_{vg}}}$ are independent of irregularity drift motion. The cross-correlation values of satellite motion are assumed to be 0 for simplification, since the satellite motions may be computed separately.

Finally, the one-sigma values σ_v, σ_θ are plotted as error bars in measurements of drift speed ${}^{d}v^{ipp}$ and direction ${}^{d}\theta^{ipp}$. Errors on AR, Ψ_a, and v_c are derivable through similar simulation and linearization, but those are not detailed here since they are

not discussed in the results.

5.2 Application to Single-Satellite Event A2

This section investigates an event that took place on December 8, 2013 (refer to Figure 2.15 and Table 3.4), during which there was a geomagnetic storm. The single-satellite study will illustrate the drift estimation and Monte Carlo simulation process.

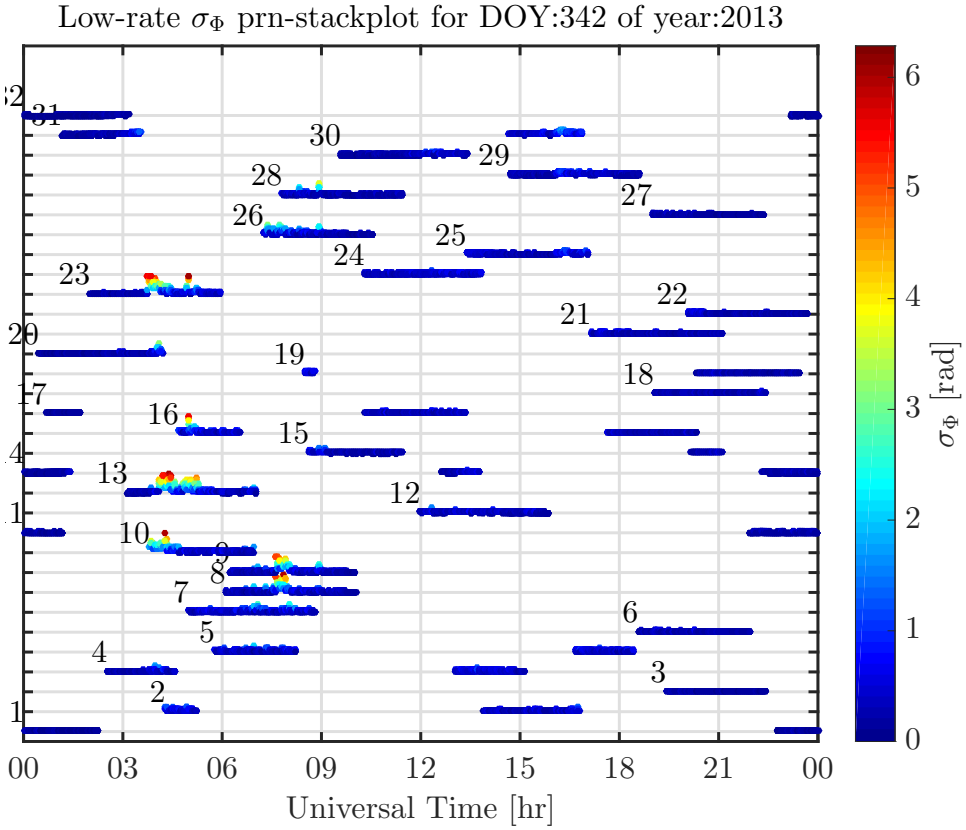

Figure 5.1. Measurements of σ_ϕ from the array of 5 operational SAGA receivers, organized by satellite number, vs. UT hour on 8 December 2013.

5.2.1 Cross-correlation of noisy measurements. The automated detection method identified a 34-minute interval from about 0343-0417 UT on 8 December 2013 (event A1) during which scintillation was occurring on the signal received from GPS satellite PRN 23 (Figure 5.1). Figure 5.2 shows the first 45 s time segment of the original detrended, filtered phase data $s_i(t), i = 1, 2, ..., 5$ (black) during 03:43:35

to 03:44:20 UT (event A2). These data are identical to those shown in Fig 3 in [57]. The largest phase variations of almost ±5 rad during the 34-minute time series are observed during this time interval. For the Monte Carlo simulation, noisy phase data $\tilde{s}_i(t)$ with white Gaussian noise of $\sigma_w^2 = 0.0625$ rad^2 is added for one ensemble member $n = 1$, also shown in Figure 5.2 (green). The noise model chosen is expected to be overly conservative. In practice, the filtering of the phase (6th order Butterworth with cutoff frequency of 0.1 Hz) has reduced much of the noise in the phase data. So we expect the error bars generated by this simulation to be conservative.

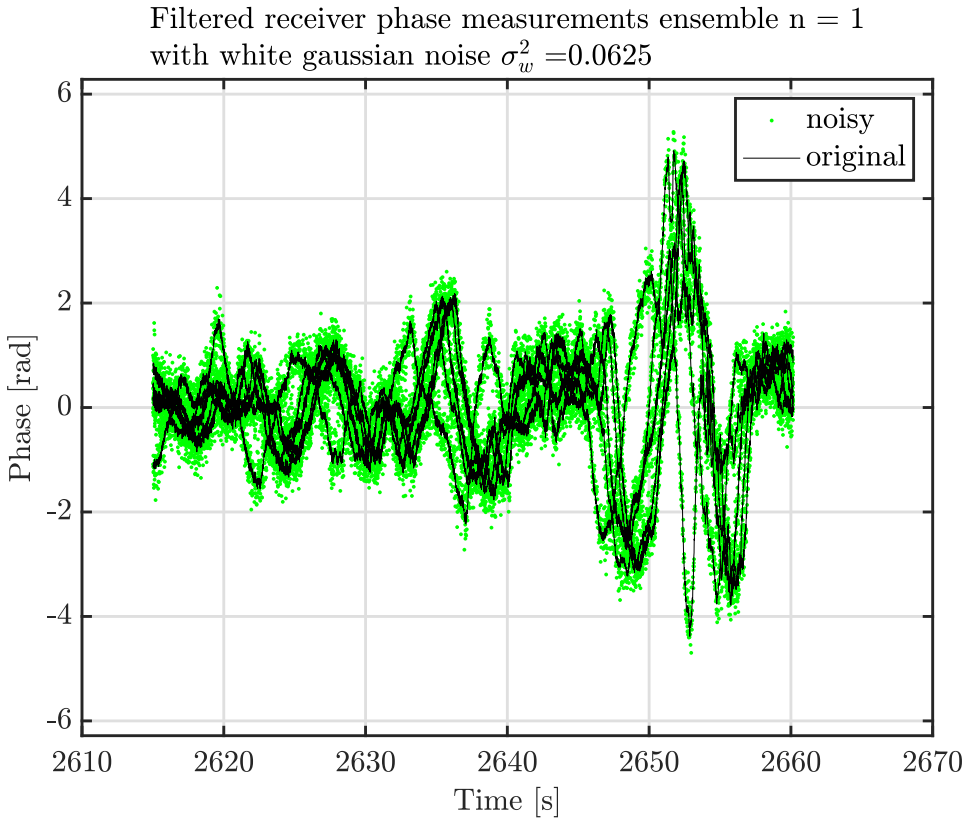

Figure 5.2. Original and noise-added phase observations during 2615-2660 s after 0300 UT, 8 Dec 2013.

Using the cross-correlation lags τ_c and corresponding auto-correlation lags τ_a as measurements in Eq. (4.22), we use the SAGA data during this time interval to make an estimate of the drift speed, direction, axial ratio, and correlation ellipse orientation as defined in Eqs. (4.15) and (4.16)-(4.18). The cross-correlations ρ_{ij} (for

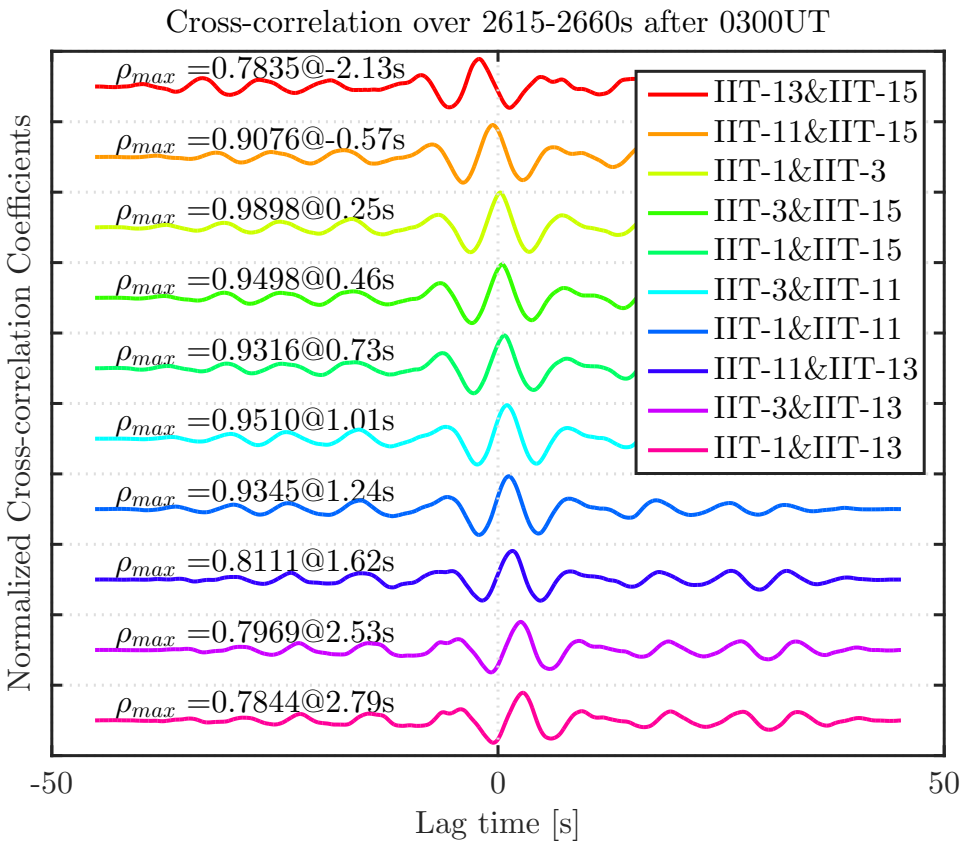

Figure 5.3. Pairwise cross-correlations ρ_{ij} in phase from PRN 23 during event A2, 2615-2660 s after 0300 UT, 8 Dec 2013.

the original "noise-free" signals) between all possible pairs of the five receivers are shown in Figure 5.3(a). The curves are arranged in order of peak time.

A map of the receiver locations centered about site IIT-3 is shown in Figure 5.4. There are two nearly parallel chains of receivers running northwest-southeast: IIT-1, -3, -11, and IIT-13 and -15. The shortest baseline is between IIT-1 and IIT-3, of 360 m. The longest baseline with the same orientation is 2.66 km between IIT-13 and IIT-15. For this example orientation, as listed in Figure 5.3, the IIT-1&IIT-3 pair (yellow-green) has a correlation peak of 0.9898, while IIT-13&IIT-15 (red) have a correlation peak of 0.7835. The correlation peak value falls with increasing distance, i.e., R in Eq. (4.10) is a decreasing function as expected.

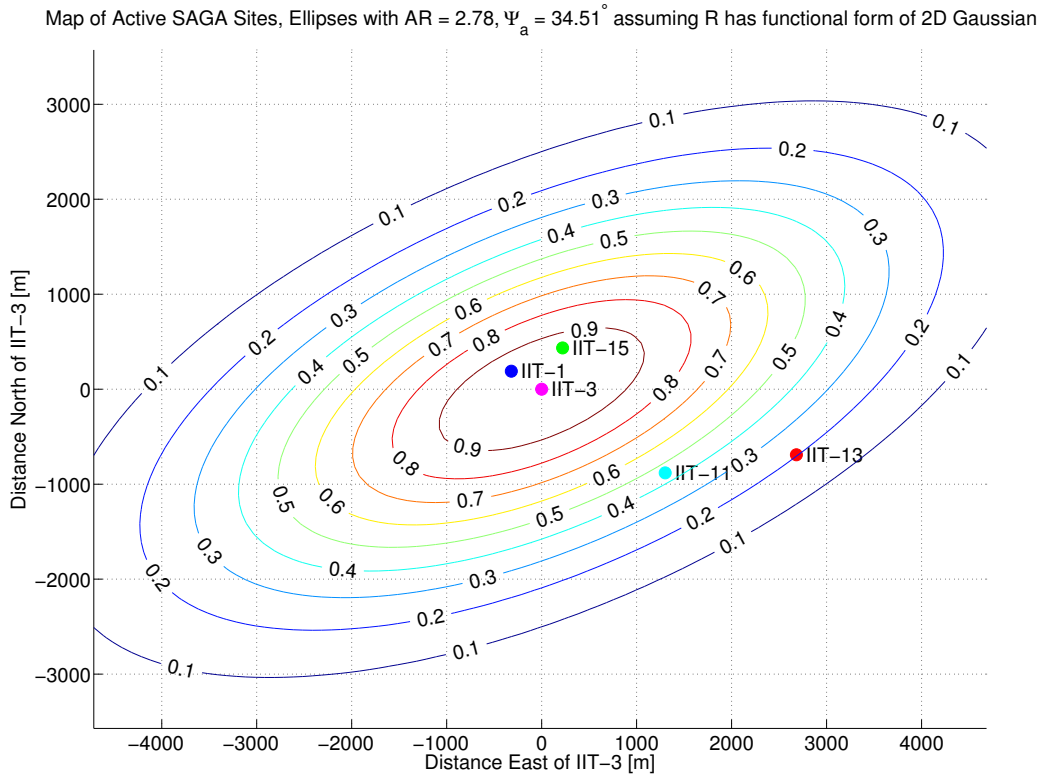

Figure 5.4. Map of active SAGA locations and example ellipses with the estimated $AR = 2.78$ and $\Psi_a = 34.51°$, assuming the functional form of R in Eq. (4.10) were a 2D Gaussian, for illustrative purposes.

In particular, we may examine the correlation values on each curve at $\tau = 0$, and this represents an instantaneous snapshot of the ellipse form given in Eq. (4.10). For illustration, if we suppose the functional form of R in Eq. (4.10) to correspond to a 2D Gaussian, then the contours of constant ρ would be ellipses consistent with our assumption. Example ellipses with the orientation Ψ_a and axial ratio AR corresponding to the estimates made from the cross-correlations in Figure 5.3(a) are shown on the map in Figure 5.3(b). The correlation values fall with increasing distance from IIT-3. This shows that, for a decreasing function R, the phase measurements are

really only correlated over about the baselines of this size array. In fact, the value of $\rho_{3,13}(\tau = 0) = -0.4276$, which is less than the contour level of $\rho = 0.2$ shown. This shows that phase-sensing arrays such as SAGA should not have baselines larger than a few km in order to sense correlated phase measurements.

The correlations shown in Figure 5.3 are noise-free. The τ_c values in the right half of each cross-correlation peak down to $\rho_{\text{cutoff}} = 0.65$ are mapped to corresponding τ_a values using Eq. (4.22). Correlation is essentially an integration process, which tends to smooth the $\tilde{\rho}_{ii}, \tilde{\rho}_{ij}$ curves, such that they differ by less than 1% from the noise-free counterparts (see Figure 5.5). These are used to assemble the vector of observations $\mathbf{y}$ from Eq. (4.24), shown in black in Figure 5.6. Each continuous segment of elements in $\mathbf{y}$ corresponds to one receiver pair.

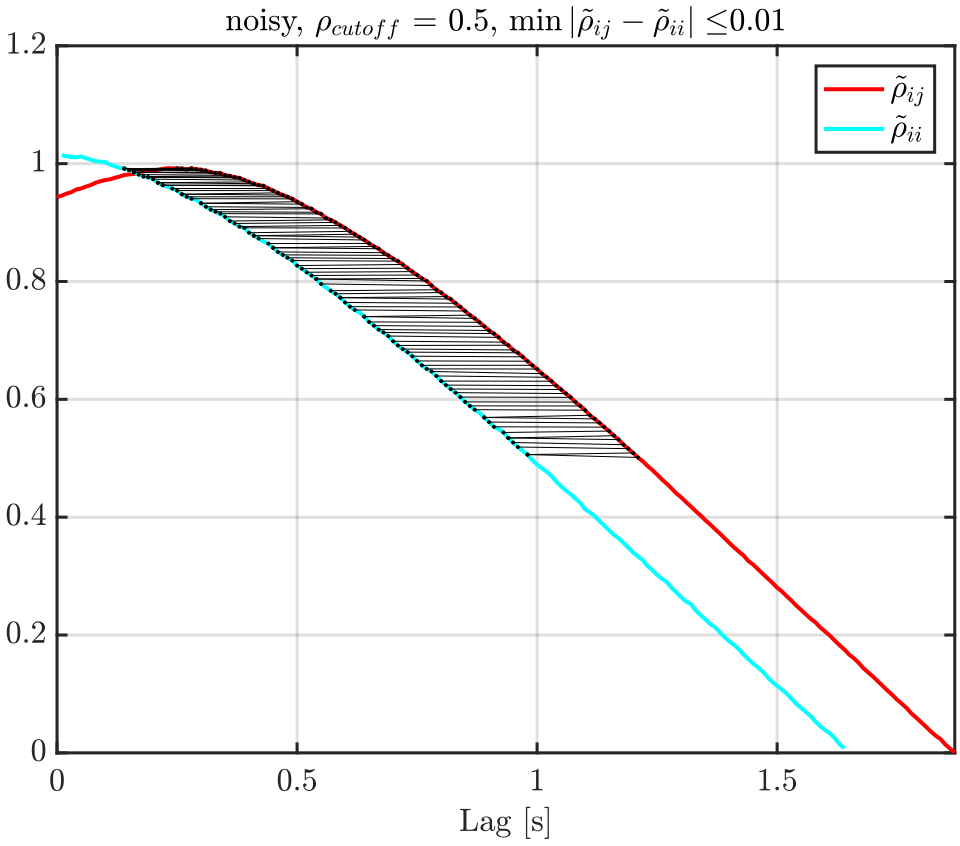

Figure 5.5. Obtaining $\tilde{\tau}_a, \tau_c$ with $\tilde{\rho}_{ij} \approx \tilde{\rho}_{ii}$.

The same cross-correlation process is applied to each noisy ensemble member (not shown). The ensembles are used to construct $\tilde{\mathbf{y}}_n$. These are shown in green for all $N = 1000$ ensemble members in Figure 5.6.

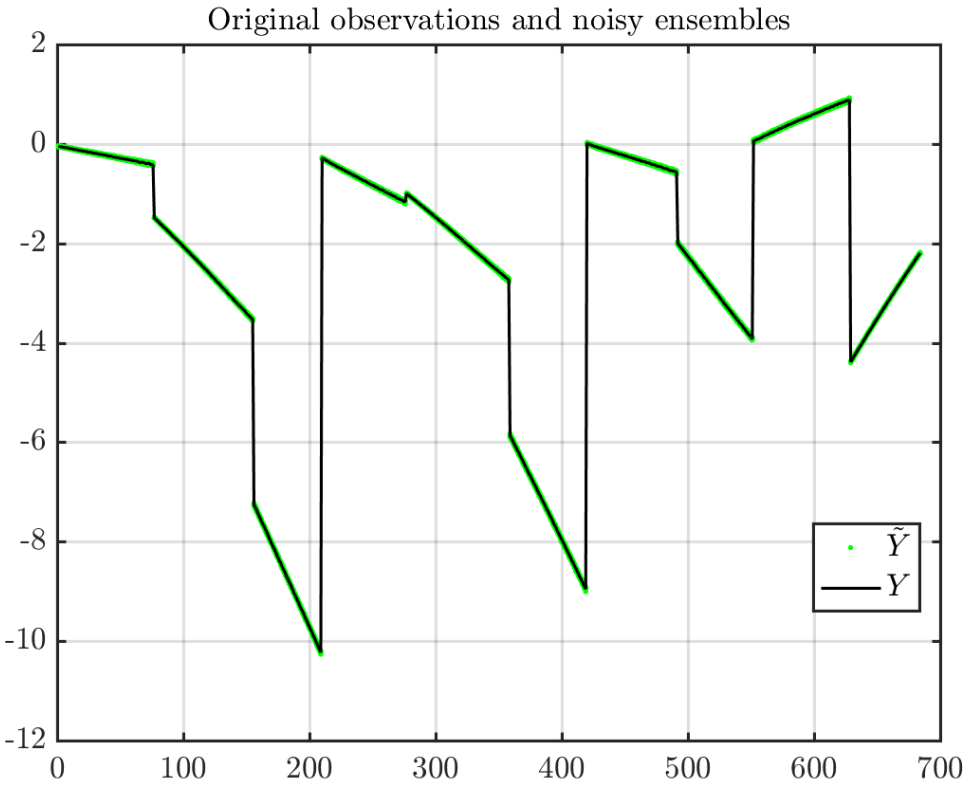

Figure 5.6. Observation array $\mathbf{y}$ defined in Eq. (4.24) based on the original phase data (black) and 1000 simulations $\tilde{\mathbf{Y}}$ of noise-added phase data (green).

The ensemble of noisy observations are each used to estimate the state $\tilde{\mathbf{x}}_n$, and those satisfying $ab-h^2 > 0$ are kept. Those $\hat{\mathbf{Y}}$ which are kept are used to estimate the error covariance $\mathbf{\Sigma}_{\hat{\mathbf{Y}}}$ according to Eqs. (5.9)-(5.10). These are propagated through to errors σ_v, σ_θ in drift magnitude and direction, characteristic velocity v_c and anisotropy estimates AR, Ψ_a. In practice, random noise ν of observations in Eqs. (4.26) are not normally distributed, as shown in Figure 5.7.

5.3 Application to Single-Satellite Event A1

5.3.1 Sensitivity of estimates to interval trigger T. Figure 5.8 shows SAGA

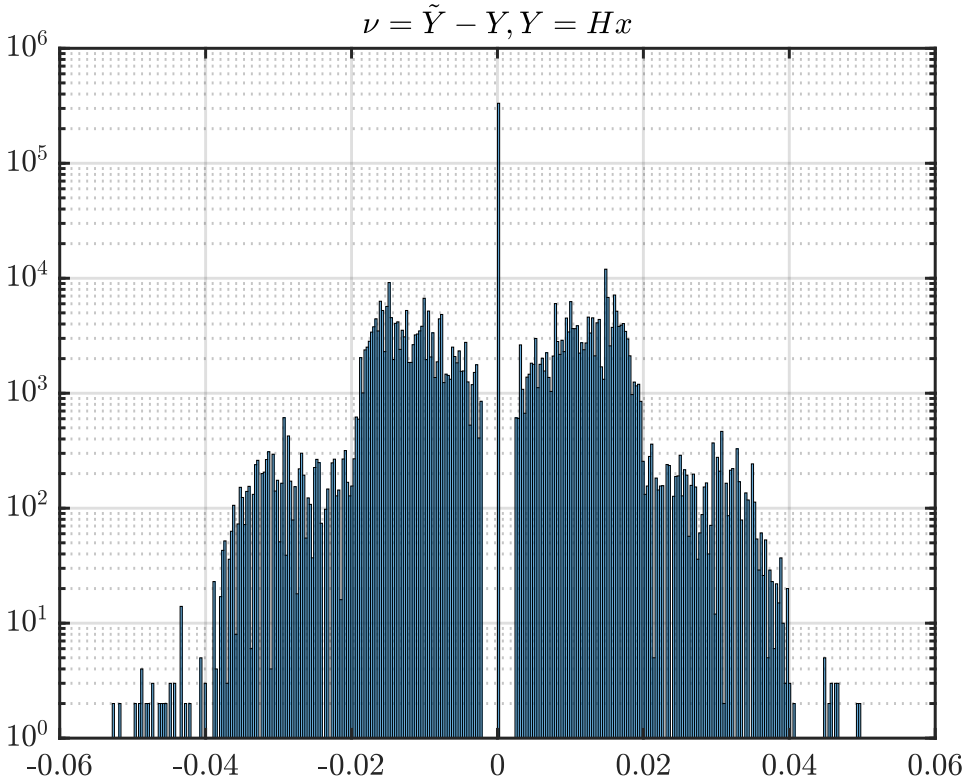

Figure 5.7. Simulated random noise ν on observation array $\mathbf{y}$ using Monte Carlo method.

horizontal drift (a) magnitude ${}^{d}v^{ipp}$ and (b) direction ${}^{d}\theta^{ipp}$ (c) axial ratio AR (d) semi-major axis angle Ψ_a with error bars from event A1 from 0343 to 0417 UT. (e) validity percentage is also shown, indicating the ratio of the number of noisy ensembles that give valid estimates K and the total number of ensembles N. The SAGA estimates of horizontal drift are based on the array-wide correlated 100 Hz phase measured from GPS PRN 23. The light magenta estimates satisfy $v_c/v < 1, v_c \in \mathbb{R}$, and the dark magenta do not. Every estimate is made over a period longer than $T = 30$ s. Estimates in Figure 5.9 are made over periods longer than 10 s, therefore including more estimates. However, to examine quantitatively the sensitivity of various estimates to the length trigger T or to evaluate the averaged variation in SAGA estimates within the complete scintillation period (34 minutes in this case), it is useful to compute normalized root-mean-squared error (RMSE) for

any SAGA estimate $z_s \in \{{}^d v^{ipp}, {}^d\theta^{ipp}, AR, \Psi_a, v_c\}$ and its one-sigma uncertainty σ_s:

$$\epsilon_n = \sqrt{\mathbf{E}\left[\frac{\sigma_s^2}{z_s^2}\right]} \tag{5.22}$$

In Figure 5.8, The 11 speeds estimated by SAGA between 0343 and 0410 UT also start around 1000 m/s and gradually increase. SAGA one-sigma uncertainties on speeds can range up to about 200 m/s but are typically much smaller. There is generally small but abrupt variation in drift orientation over the span of 34 minutes, the majority consistently measuring northwestward motion.

Table 5.1. ϵ_n for PRN23 during event A1 : 0343-0417 UT on December 8, 2013 with $0 < v_c < v, v_c \in \mathbb{R}$

T s	10	30
# good	10	5
# estimation	34	19
ϵ_v[%]	13.78	6.1343
ϵ_θ[%]	11.352	1.8971
ϵ_{AR}[%]	16.858	4.1701
ϵ_{Ψ_α}[%]	0.6881	0.57134
ϵ_{v_c}[%]	21.632	7.3843

The K/N ratio are 100% for all the estimates, indicating that none of the noisy ensembles gives invalid results. The characteristic velocity v_c defined in Eq. (4.19) may become complex valued (not shown). In addition, the assumption of frozen-in drifts for which a drift velocity can be found relies on $(v_c/{}^d v^{ipp}) < 1$. If we eliminate the SAGA estimates for which the characteristic velocities are either imaginary or larger than the drift speed, then only 5 estimates remain (light magenta).

For anisotropy, $AR \leq$ or ≈ 10 for all these time instants while Ψ_a sees shifting from 45 ° to $\approx 90°$. The RMSEs ϵ_n of each estimated quantities for PRN 23 are summarized in Table 5.1, which also provides comparison between Figure 5.8 and 5.9. Interestingly, although a smaller value of T gives more estimates in total, it does not guarantee a proportional increase in the number of "good"" estimates that don't violate the characteristic velocity condition. Furthermore, larger variation in almost every estimation quantity within the same period is observed for T = 10 s.

5.4 Application to Single-Satellite Event B1

Following the same fashion, event B1 for PRN 29 in Feb 20, 2014 discussed in Chapter 4 is revisited for re-evaluation. Estimates for T = 30 and 10 s are shown respectively in Figure 5.10 and 5.11. In comparison to event A1, there are a lot more estimates in total without imposing v_c condition.

Table 5.2. ϵ_n for PRN29 during event B1 : 1120-1157 UT on February 20, 2014 with $0 < v_c < v, v_c \in \mathbb{R}$

T s	10	30
# good	10	8
# estimation	40	27
ϵ_v[%]	6.2237	4.3551
ϵ_θ[%]	2.8342	3.0919
ϵ_{AR}[%]	9.5885	9.3143
ϵ_{Ψ_α}[%]	2.2041	2.0287
ϵ_{v_c}[%]	9.0437	8.8947

The ϵ_n within 37 minutes are summarized in Table 5.2 In this case, percentage

of "good estimates" is again lowered with a smaller T. Only a slight decrease in the variation in most estimate parameters is seen for T = 10 s; drift magnitude is even slightly larger.

5.5 Summary

This chapter presents an error analysis of the SAGA estimates based on Monte Carlo simulation. Event A2 has been studied to demonstrate the implementation of the approach, which is then applied to event A1 for estimation uncertainty on SAGA irregularity estimates. Event examined in Chapter 4 is also revisited for evaluation of sensitivity of estimates to signal duration.

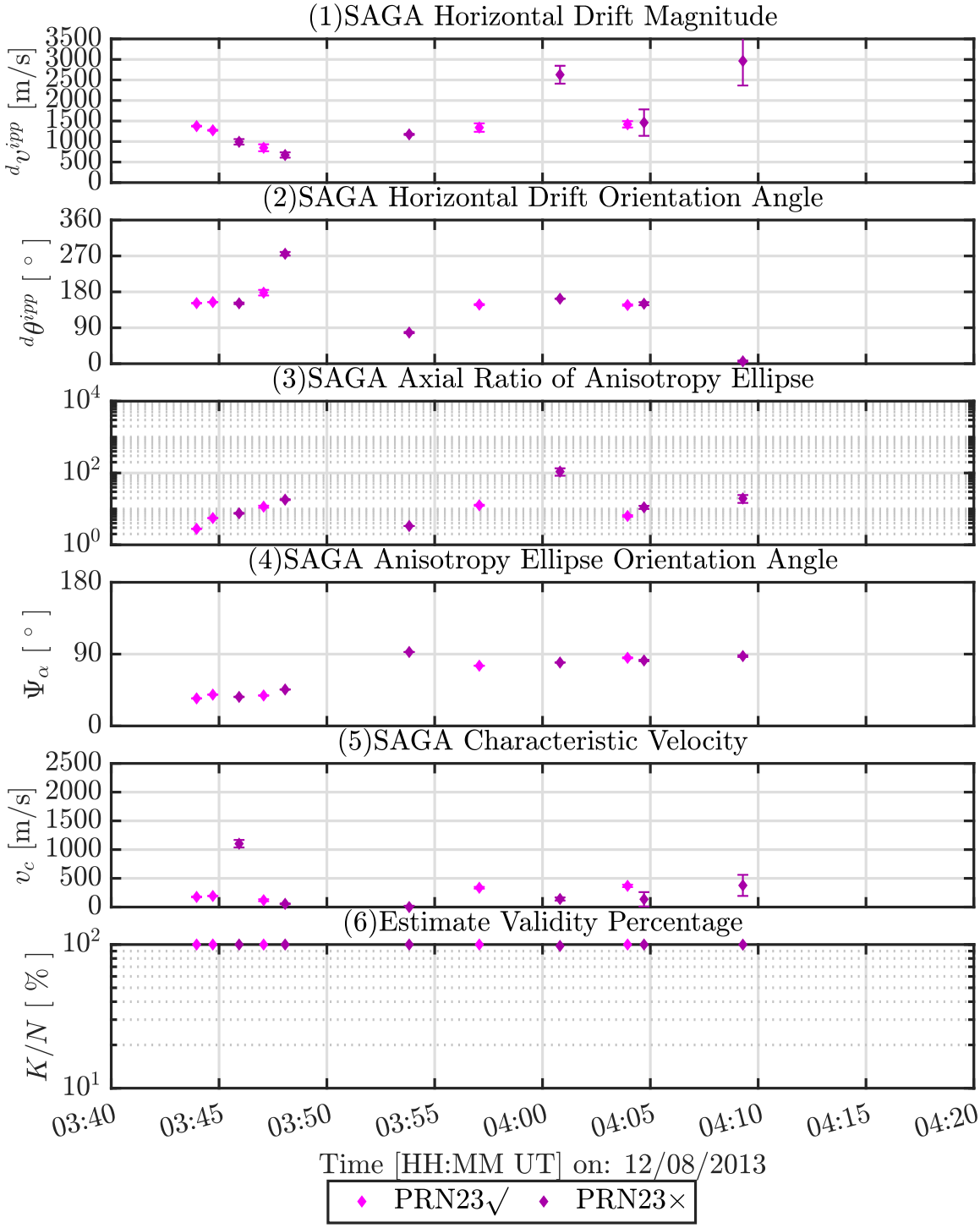

Figure 5.8. Estimates vs time as measured by SAGA from PRN 23 for $T = 30$ s., after subtracting off satellite motion. Light magenta points satisfy $v_c/v < 1, v_c \in \mathbb{R}$, and dark magenta estimates do not.

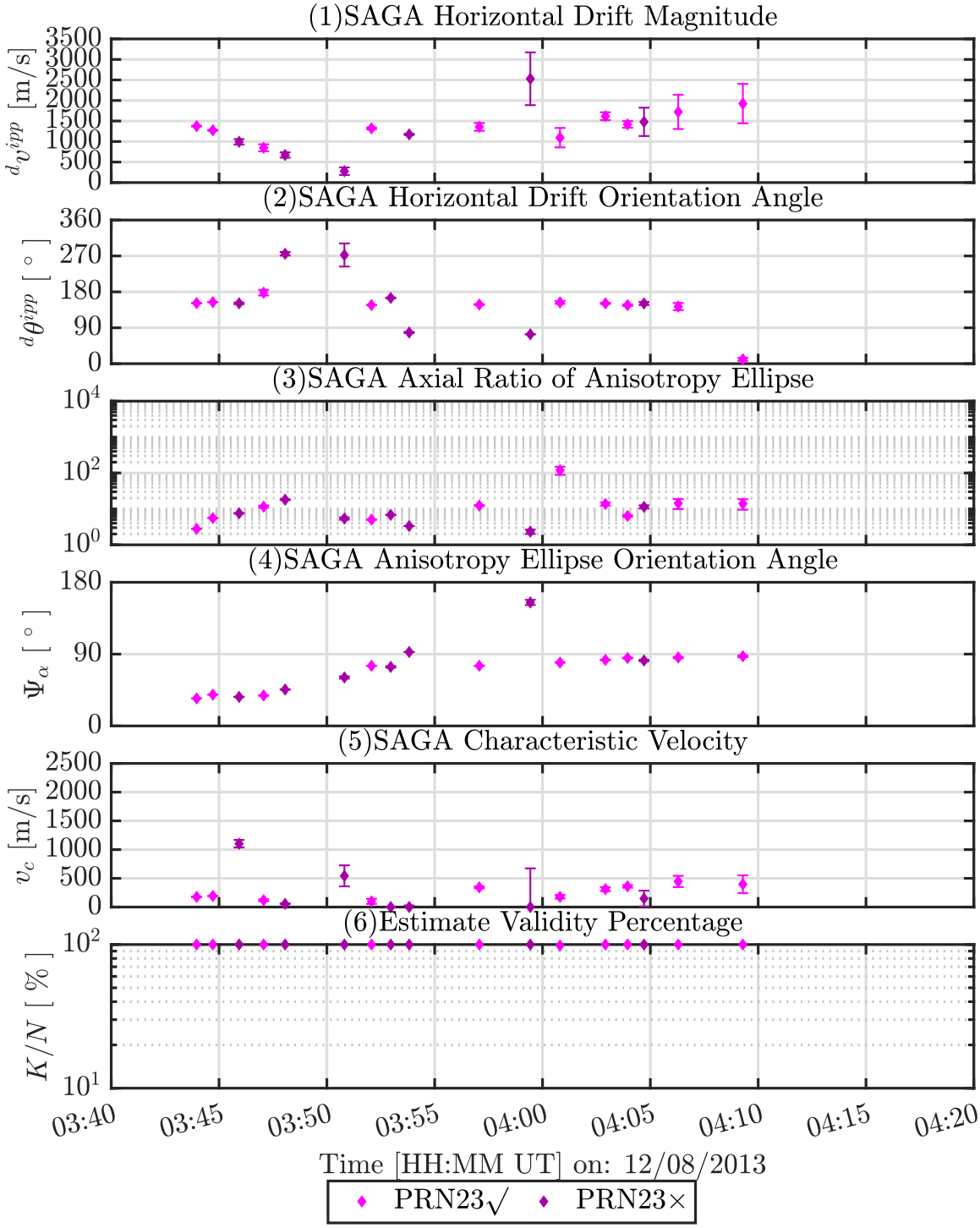

Figure 5.9. Estimates vs time as measured by SAGA from PRN 23 for $T = 10$ s, after subtracting off satellite motion. Light magenta points satisfy $v_c/v < 1, v_c \in \mathbb{R}$, and dark magenta estimates do not.

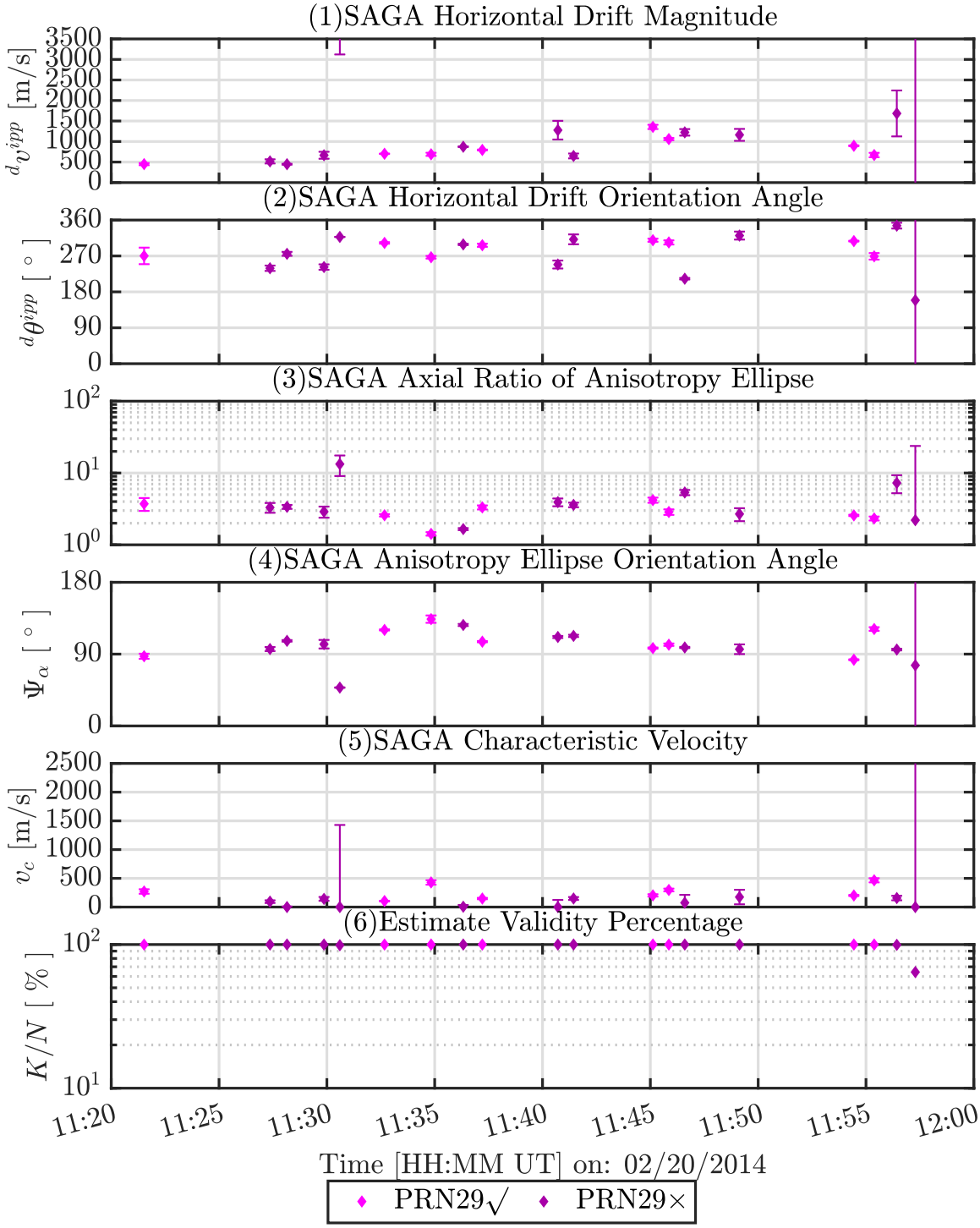

Figure 5.10. Estimates vs time as measured by SAGA from PRN 29 for $T = 30$ s., after subtracting off satellite motion. Light magenta points satisfy $v_c/v < 1, v_c \in \mathbb{R}$, and dark magenta estimates do not.

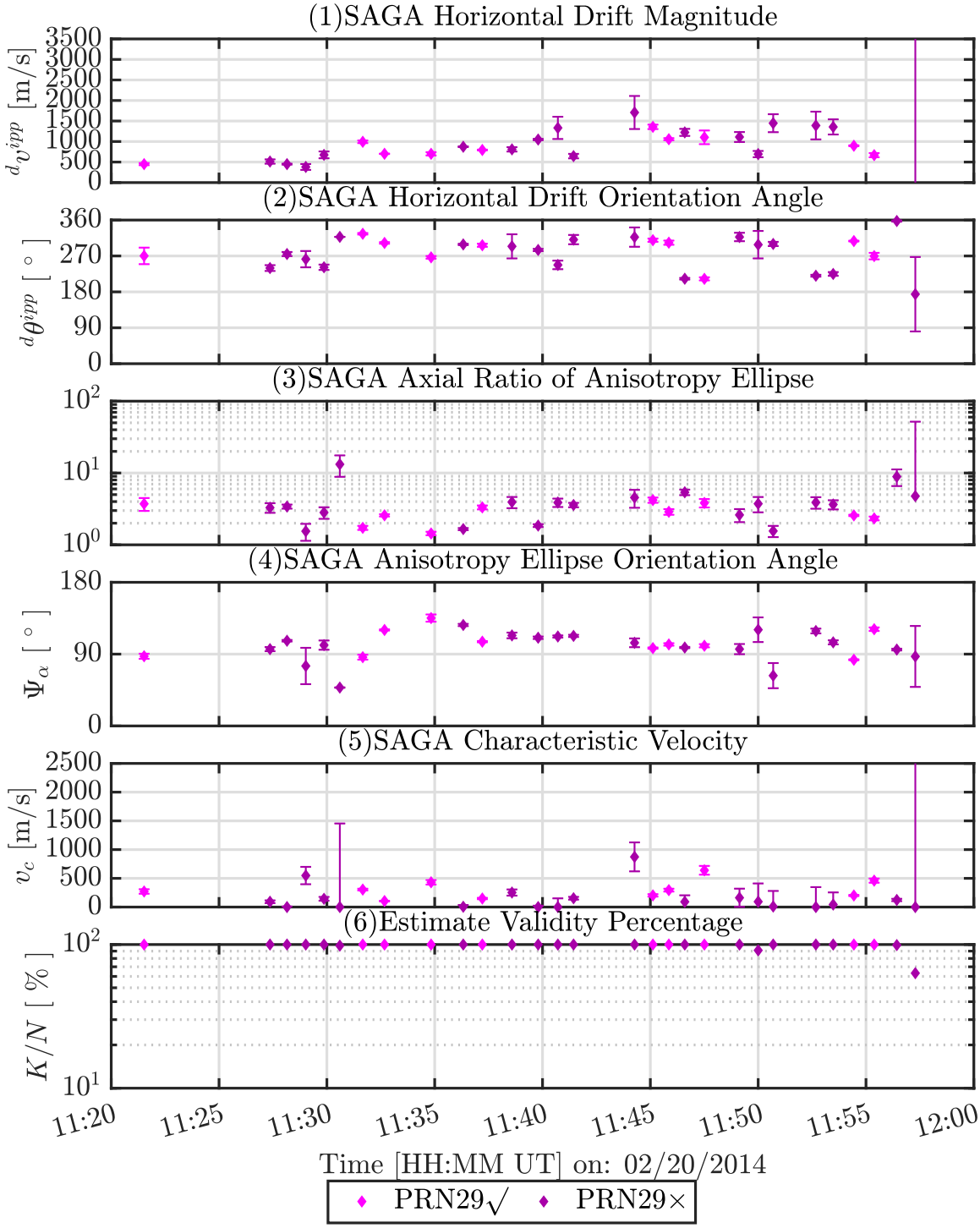

Figure 5.11. Estimates vs time as measured by SAGA from PRN 29 for $T = 10$ s., after subtracting off satellite motion. Light magenta points satisfy $v_c/v < 1, v_c \in \mathbb{R}$, and dark magenta estimates do not.

CHAPTER 6

MULTI-INSTRUMENT STUDY OF THE IONOSPHERE

This chapter will demonstrate how a suitably spaced distributed array like SAGA can also be used in coordination with other existing measuring techniques such as incoherent scatter radar and optical all-sky imagers for multi-instrument studies of irregularities. SAGA speed estimates are compared to drift measurements from Poker Flat Incoherent Scatter Radar (PFISR).

6.1 Propagation of PFISR Uncertainties

The velocities written in geographic and magnetic field coordinates are respectively $\mathbf{v_g}$ and $\mathbf{v_f}$. The rotation matrix ${}^{\mathbf{g}}\mathbf{R}^{\mathbf{f}}$ is dependent on declination and inclination of PFISR, the full expression for which is described in [8]. In this work, it is assumed that errors in PFISR drift components are uncorrelated. In this analysis, the vertical component v_u, its error and covariances are not used, as SAGA only detects horizontal drifts, so matrix $\mathbf{G}$ selects only the horizontal drift components.

$$\underbrace{\begin{bmatrix} v_e \\ \\ v_n \end{bmatrix}}_{\mathbf{v_g}} = \underbrace{\begin{bmatrix} 1 & 0 & 0 \\ \\ 0 & 1 & 0 \end{bmatrix}}_{\mathbf{G}} {}^{\mathbf{g}}\mathbf{R}^{\mathbf{f}} \underbrace{\begin{bmatrix} v_{\perp e} \\ \\ v_{\perp n} \\ \\ v_{anti\parallel} \end{bmatrix}}_{\mathbf{v_f}} \tag{6.1}$$

From Eqs. (4.17) and (4.18) we obtain SAGA horizontal drift magnitude v and angle θ in geographic coordinates. To compare, the uncertainties in horizontal PFISR geographic components σ_e, σ_n and covariance σ_{en} are propagated to v and θ,

two non-linear functions of v_e and v_n.

$$v = \sqrt{{v_e}^2 + {v_n}^2}\ , \theta = \arctan\left(\frac{v_n}{v_e}\right) \tag{6.2}$$

$$\begin{bmatrix} v \\ \theta \end{bmatrix} = \underbrace{\begin{bmatrix} \frac{\partial v}{\partial v_e} & \frac{\partial v}{\partial v_n} \\ \frac{\partial \theta}{\partial v_e} & \frac{\partial \theta}{\partial v_n} \end{bmatrix}}_{\mathbf{J}} \begin{bmatrix} v_e \\ v_n \end{bmatrix} \tag{6.3}$$

Using the derivation by [58], they are linearized to a first-order Taylor series expansion around the expected values and the corresponding Jacobian $\mathbf{J}$ is computed as shown in Eq. (6.3). Eq. (6.4) rotates the covariance matrix for $\mathbf{v_f}$ to that for v, θ to obtain errors in magnitude and angle σ_v, σ_θ for the PFISR measurements.

$$\underbrace{\begin{bmatrix} \sigma_v^2 & \sigma_{\theta v} \\ \sigma_{\theta v} & \sigma_\theta^2 \end{bmatrix}}_{\mathbf{\Sigma}_{v,\theta}^{\mathrm{PFISR}}} = \mathbf{J}\mathbf{G}^{\mathbf{g}}\mathbf{R}^{\mathbf{f}} \underbrace{\begin{bmatrix} \sigma_{\perp e}^2 & 0 & 0 \\ 0 & \sigma_{\perp n}^2 & 0 \\ 0 & 0 & \sigma_{anti\parallel}^2 \end{bmatrix}}_{\mathbf{\Sigma_{vf}}} (\mathbf{J}\mathbf{G}^{\mathbf{g}}\mathbf{R}^{\mathbf{f}})^{\mathbf{T}} \tag{6.4}$$

PFISR estimates made near 65.12 ° N where SAGA is located would provide the most nearly collocated sampling of the ionosphere. Unfortunately, estimates from PFISR at 65.25 ° N (the lowest latitude available) do not have the smallest uncertainties at all times, as shown in Table 6.1. Deriving the normalized root mean square errors ϵ_{pn} of these estimates within a certain time period for each latitude within a certain range of latitudes will help decide which latitude of estimates to use for best comparison to SAGA. Let z_p be the PFISR true values and SAGA estimates z_s

$$\epsilon_{pn} = \sqrt{\mathbf{E}\left[\frac{\sigma_p^2}{z_p^2}\right]} \tag{6.5}$$

$$\epsilon_{sn} = \sqrt{\mathbf{E}\left[\frac{(z_s - z_p)^2}{z_p^2}\right]} \tag{6.6}$$

Table 6.1. ϵ_{pn} during events A3, B1 and C1

	A3		B1		C1	
°N	ϵ_v[%]	ϵ_θ[%]	ϵ_v[%]	ϵ_θ[%]	ϵ_v[%]	ϵ_θ[%]
65.25	86.95	142.33	455.03	107.35	N/A	N/A
65.50	86.95	142.33	455.03	107.35	N/A	N/A
65.75	894.34	811.84	1283.74	1172.33	11188.22	1232.11
66.00	5.90	2.47	533.87	501.09	20.08	3.81
66.25	3.58	2.02	547.98	1199.17	26.20	3.92
66.50	2.72	1.57	245.86	58.76	19.19	4.42
66.75	2.68	1.48	111.51	40.02	25.05	4.88
67.00	3.52	1.60	76.85	16.77	169.77	34.77
67.25	3.91	1.48	332.55	97.63	571.18	358.67
67.50	4.55	1.52	457.94	153.60	200.56	396.95
67.75	6.36	1.77	104.10	42.10	227.79	351.63
68.00	9.61	2.86	758.36	318.33	180.36	66.65

6.2 Application to Multi-Satellite Event A3

The automated detection routine is also used to identify periods when multiple satellites are scintillating simultaneously. Within the time interval during which PRN 23 scintillates, during 0403 to 0417 UT, PRNs 10 and 13 also scintillate. Figure 6.1, 6.2,6.3 respectively shows the 100 Hz power and phase observations received from the five operational receivers from (a) PRN 10, (b) PRN 13, and (c) PRN 23 from 0403 UT to 0417 UT. The 100 Hz I and Q power and phase data from these satellites during these periods are processed by techniques detailed in [49] to obtain the detrended and filtered high-rate amplitude/phase observations shown here. A second study will be conducted on the 0403 to 0417 UT time interval for each of the three satellites' phase data shown in Figure 6.3.

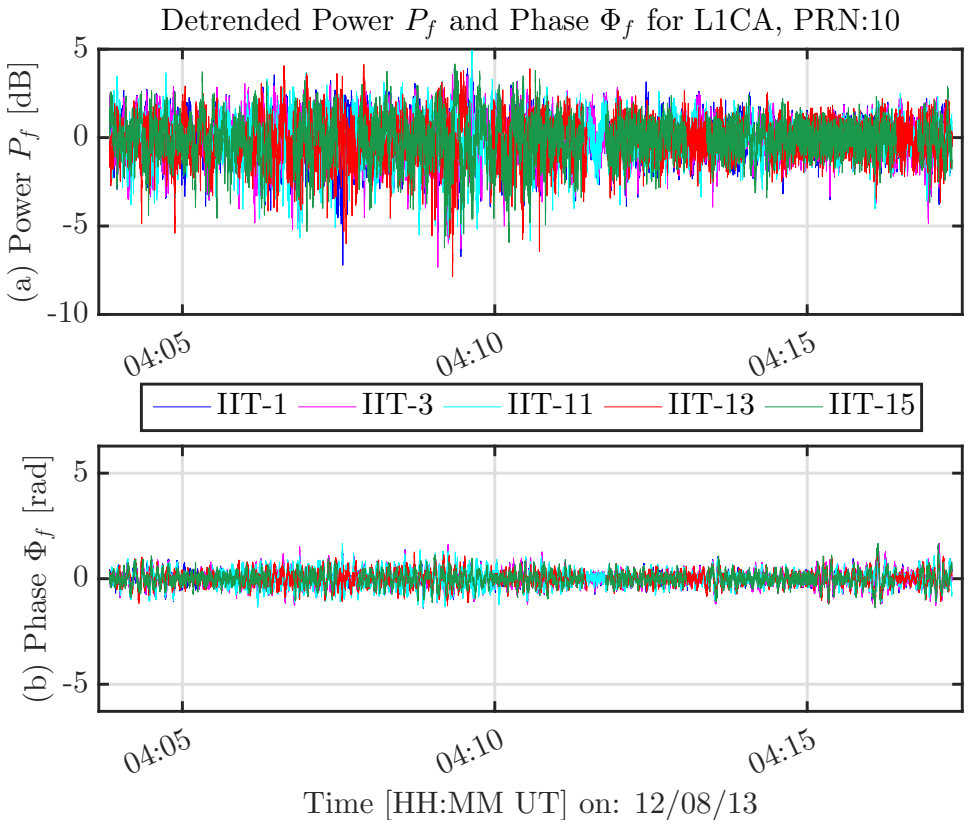

Figure 6.1. 100 Hz detrended and filtered power phase for (a) PRN 10 at 0403-0417 UT on 8 Dec 2013.

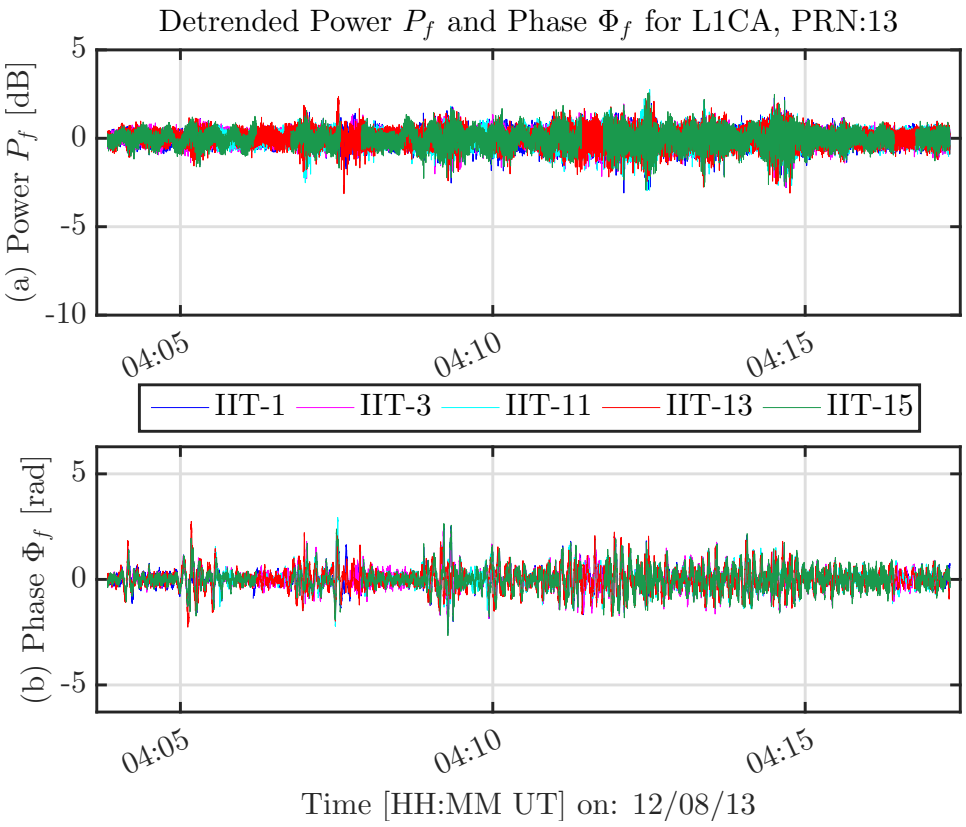

Figure 6.2. 100 Hz detrended and filtered power phase for (b) PRN 13 at 0403-0417 UT on 8 Dec 2013.

With the processed phase data from SAGA such as shown in Figure 6.3, spaced-receiver techniques in Section 4.3 are applied for drift and anisotropy estimation. A Monte Carlo simulation of noise as described in Section 5.1 is used to estimate uncertainties, with an ensemble of $N = 1000$ members.

The resulting estimates and uncertainties are compared to independent measurements from the Poker Flat incoherent scatter radar (PFISR), also located at Poker Flat Research Range. Note that while PFISR is sited nearby (within 1 km) at Poker Flat Research Range, most of the beams are far from the scintillating PRNs. PFISR does not measure characteristic velocity, axial ratio, or orientation of the correlation ellipse, so those quantities are not compared.

Figure 6.4 is a skyplot (zenith at the center) showing the location of each of

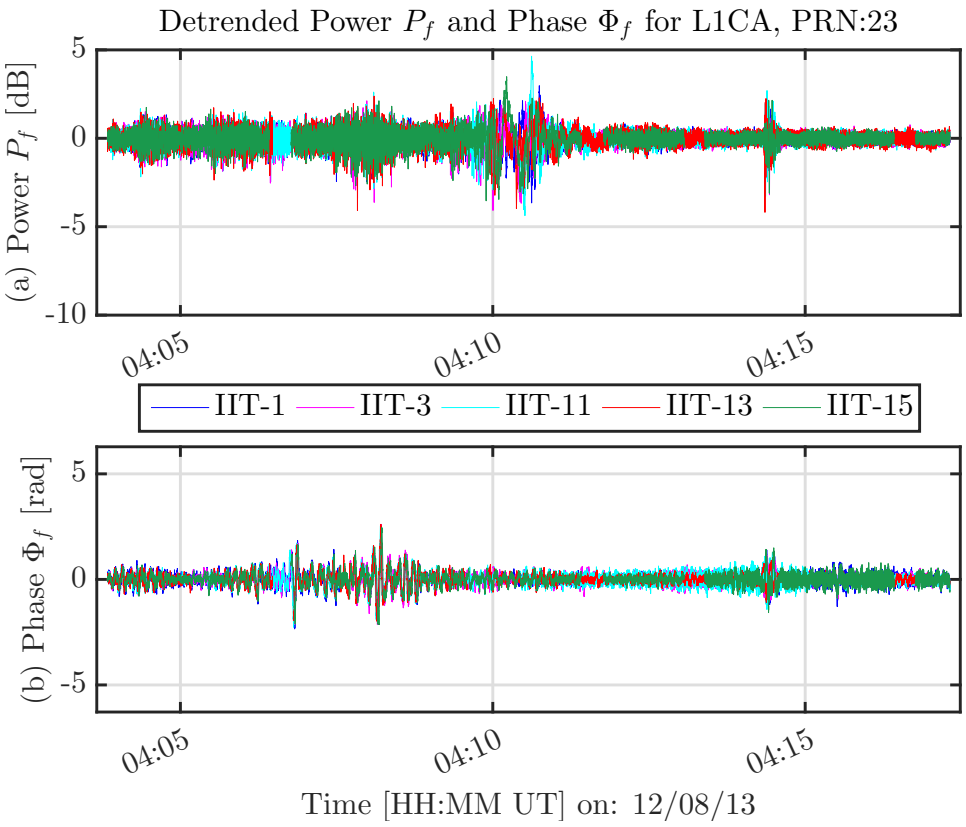

Figure 6.3. 100 Hz detrended and filtered power phase for (c) PRN 23 at 0403-0417 UT on 8 Dec 2013.

the PRNs in the sky during the scintillating time period. PFISR beams are marked with squares. Also on this plot are intensities of the 630.0 nm redline auroral emission taken by a colocated camera at PFRR. All of the satellites' IPPs being in the vicinity of the auroral arc indicates that the scintillation activity observed by SAGA is likely to be correlated with it. PRN 10 is at relatively low elevation to the west, and far from the PFISR beam locations. PRN 13 is at about 60° elevation, west of the southernmost PFISR beam, which points anti-parallel to the magnetic field. PRN 23 is at high elevation in the sky, and a bit east of the southernmost PFISR beam.

PFISR was operating during 0343-0417 UT on 8 December 2013, and the 180-s resolution measured velocities may be used for comparison to the SAGA-based drift estimates. From Table 6.1, the best measurement candidate for comparison is those

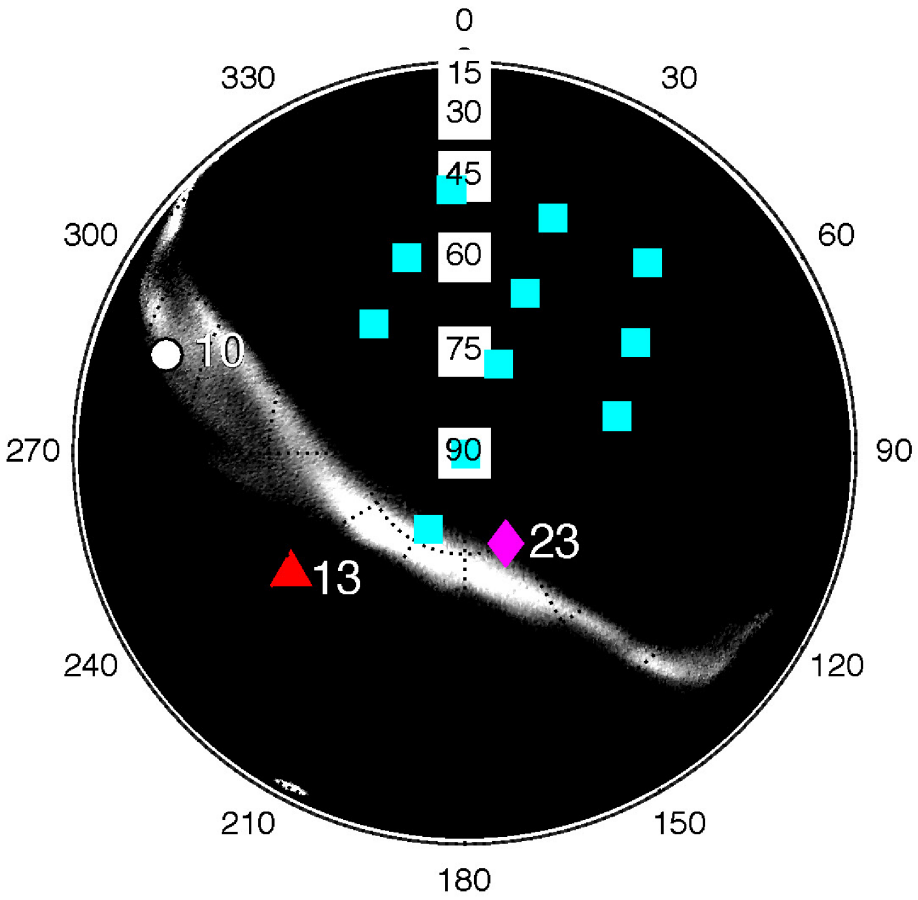

Figure 6.4. Skyplot of satellite locations and PFISR radar beams (cyan) at 0403–0417 UT for PRNs 10, 13, and 23.

made at the nearest latitude 66° N with $\epsilon_{pn} \leq 100\%$ for both drift magnitude and direction over this period.

To compare PFISR measurements with SAGA estimates in geographic east-north-up (ENU) coordinates, PFISR drift velocity data $\mathbf{v_f}$ whose covariance matrix is $\mathbf{\Sigma_{vf}}$, are rotated from magnetic field-oriented coordinates. The rotation and propagation of uncertainties provided on the PFISR measurements are described in 6.1.

Since PFISR and SAGA do not make measurements simultaneously, to quantify deviations of SAGA from PFISR measurements, the PFISR measurements are

linearly interpolated in time using the nearest prior and subsequent PFISR data to the SAGA measurement time. Then the root-mean-squared normalized error ϵ_{sn} between SAGA measured quantity $z_s = \{{}^d v^{ipp}, {}^d\theta^{ipp}\}$ and corresponding PFISR measurements z_p (where z may be either the drift speed or direction) is computed according to Eqs. (6.6). Using the estimation and error analysis methods illustrated respectively in Section 4 and 5, we analyze the time interval during which multiple satellites are scintillating. Figure 6.5 shows the SAGA measurements of drift speed and direction using PRNs 10, 13, and 23 from 0343 to 0417 UT meeting the characteristic velocity requirements $v_c/v < 1, v_c \in \mathbb{R}$. The PRN 23 measurements are the same data as the light magenta data in Figure 5.8. The measurements made using PRN 13 (red triangles) and PRN 10 (black circles) occur between 0405 and 0417 UT. The PFISR measurements at 66° N latitude are plotted in blue with error bars, and the time-interpolated values are blue squares.

The PFISR drifts are approximately 1000 m/s gradually increasing to 2200 m/s northwestwards. The 11 speeds estimated by SAGA between 0343 and 0410 UT, also starting around 1000 m/s and gradually increasing. SAGA one-sigma uncertainties on speeds can range up to about 200 m/s but are typically much smaller. There is general consistency between SAGA measurements and PFISR, particularly at 0343 0345 UT, which includes the segment whose cross-correlation was shown in Figure 5.3. There is a fair agreement in drift orientation among the two sets of estimates, the majority consistently measuring northwestward motion. Applying the assumption of frozen-in drifts for which a drift velocity can be found relies on $v_c/{}^d v^{ipp} < 1$, only 5 estimates remain. The valid estimates have $\epsilon_v \approx 10\%, \epsilon_\theta \approx 10\%$.

There were initially seven measurements made using PRN 10, a majority with unrealistically high speeds exceeding 10 km/s. Requiring $v_c/v < 1, v_c \in \mathbb{R}$ eliminates all the measurements. PRN 10 is the lowest elevation satellite and the farthest from

any of the PFISR radar beams.

With PRN 13, six measurements of drift were initially made between 0407 and 0417 UT. Enforcing the requirements $v_c/v < 1, v_c \in \mathbb{R}$, eliminates the largest outliers in direction estimation. A total of three measurements remain, two of which have small uncertainties, but are outside of the PFISR data error bars. Interestingly the measurement with the largest uncertainty happens to estimate the speed right within the PFISR error bars. Comparing to PFISR measurements interpolated to those times gives $\epsilon_v \approx 25\%, \epsilon_\theta \approx 15\%$.

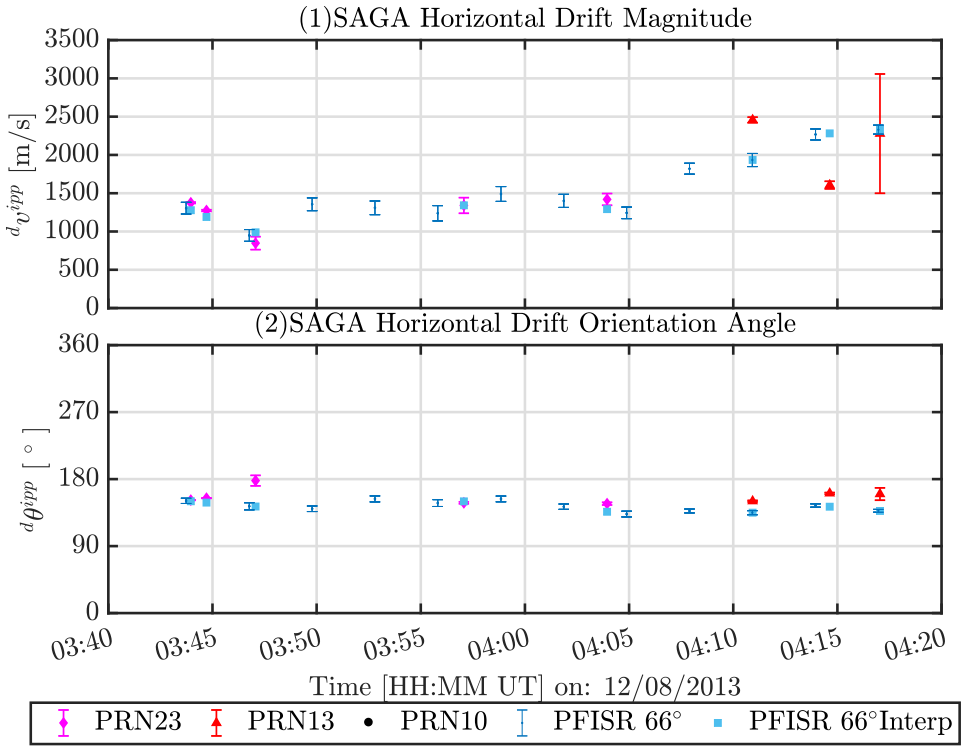

Figure 6.5. Estimates of drift speed and direction vs time as measured by signals from PRNs 10, 13, and 23, after subtracting off satellite motion. Estimates are made over periods longer than $T = 30$ s. Each color curve corresponds to one PRN. PFISR measurements during this interval are also shown.

One important consideration to bear in mind in this comparison is that the PFISR and SAGA measurements are not collocated. Even though drift measurements are published for a lower latitude nearer to the SAGA IPPs (65.25 ° N), the

Table 6.2. ϵ_{sn} with $0 < v_c < v, v_c \in \mathbb{R}$, compared to 66 ° N, for event A3.

PRN	# good	# estimation	ϵ_v[%]	ϵ_θ[%]
23	5	19	9.0421	11.602
13	3	9	23.153	13.707
10	0	9	NaN	NaN

measurement errors on the PFISR data themselves are significantly higher. The measurements made at the lower latitude are based on data from the southernmost beam. Although the southernmost PFISR beam is nearest to both PRNs 23 and 13 in the multi-satellite study, because the radar beam points upward anti-parallel to the magnetic field line at Poker Flat, it is less sensitive to field-perpendicular (i.e., primarily horizontal) drift velocities, and thus has higher uncertainty. In addition PFISR measurements are made by integrating over a longer time interval of 180 s. Also, operating at lower frequencies, PFISR is capturing bulk motion of larger scale ionospheric structure, within which it is possible that L-band sized irregularities may be moving. Despite these factors, there is a consistency between the two sets of estimates, after eliminating those not satisfying the conditions on v_c, of speeds of about 1000-2000 m/s in a northwestward direction.

Table 6.2 summarizes and compares errors of SAGA estimates for this event.

6.3 Application to Multi-Satellite Event C1

This multi-satellite study discusses 30 minutes data from 3 satellites from March 17, 2015, another geomagnetic storm day due to coronal mass ejection [53]. This was one of the largest geomagnetic storms in the most recent solar cycle, and one during which SAGA was operating.

In a same fashion, Figure 6.6 shows the SAGA measurements of drift speed and direction using PRNs 18, 22, and 27 from 1302 to 1325 UT meeting the characteristic velocity requirements $v_c/v < 1, v_c \in \mathbb{R}$. The measurements made using PRN 27(magenta diamond) 22 (red triangles) and PRN 18 (black circles) occur between 1302 and 1325 UT. The PFISR measurements at 66° N latitude are plotted in blue with error bars, and the time-interpolated values are blue squares.

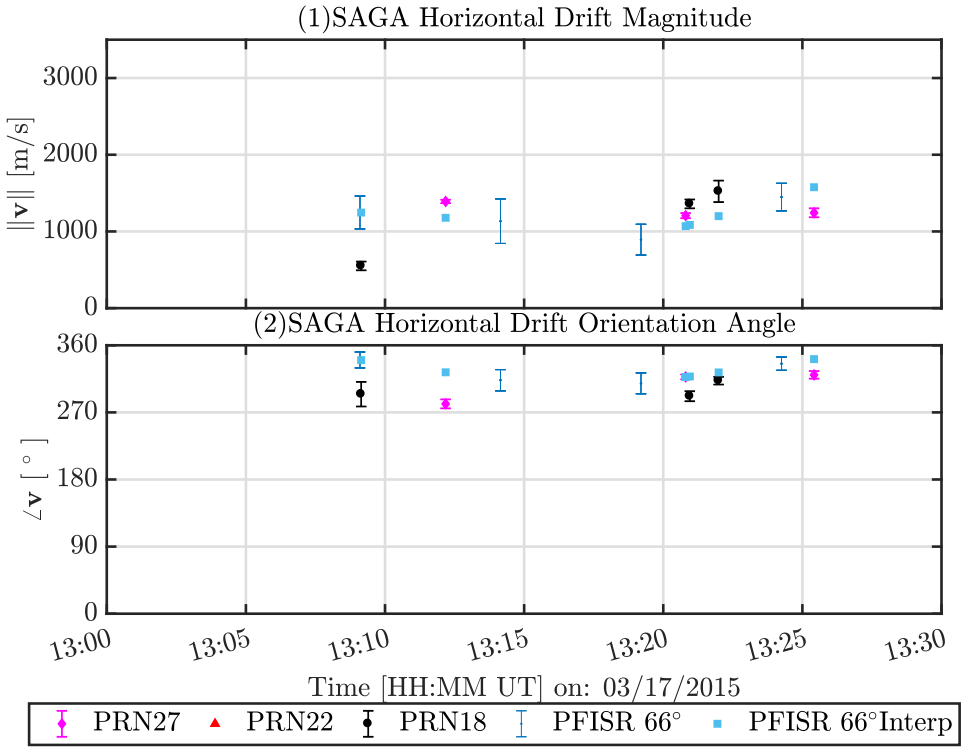

Figure 6.6. Estimates of drift speed and direction vs time as measured by signals from PRNs 18, 22, and 27, after subtracting off satellite motion. Estimates are made over periods longer than $T = 30$ s. Each color curve corresponds to one PRN. PFISR measurements during this interval are also shown.

There were initially 16 measurements made using PRN 22, a majority with unrealistically high speeds exceeding 10 km/s. Requiring $v_c/v < 1, v_c \in \mathbb{R}$ eliminates all the measurements. PRN 22 is the lowest elevation satellite and the farthest from any of the PFISR radar beams.

With PRN 18, 15 measurements of drift were initially made between 1305 and

1325 UT. Enforcing the requirements $v_c/v < 1, v_c \in \mathbb{R}$, eliminates the largest outliers in direction estimation. A total of 3 measurements with small uncertainties remain, but all of them are either outside of the PFISR data error bars. Comparing to PFISR measurements interpolated to those times gives $\epsilon_v \approx 40\%, \epsilon_\theta \approx 15\%$.

With PRN 27, 16 measurements of drift were initially made between 1305 and 1325 UT. Again imposing the v_c requirements gives a total of 3 measurements with small uncertainties. Although only interpolated estimates are available at those times, good agreement is found between the two instruments, giving $\epsilon_v \approx 20\%, \epsilon_\theta \approx 10\%$.

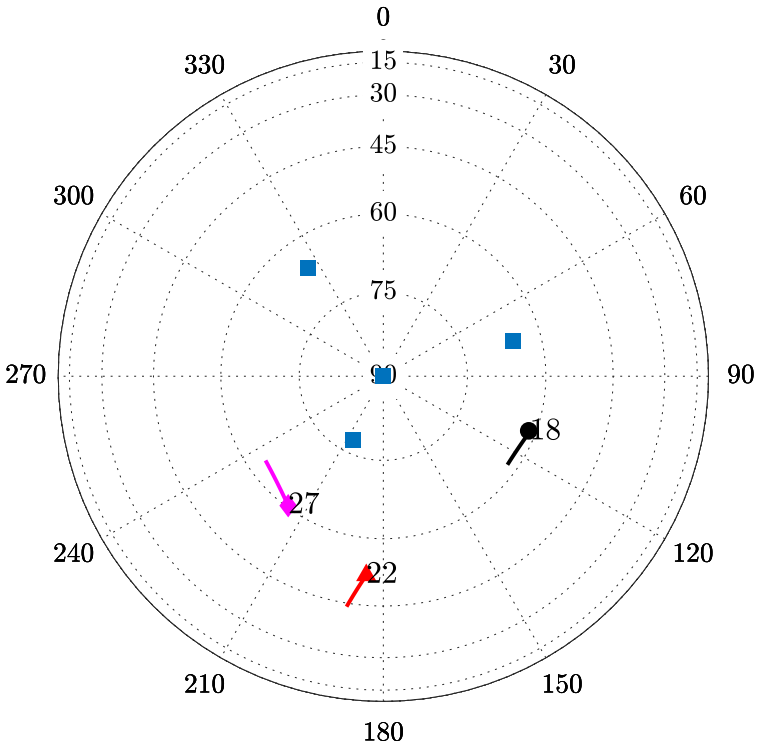

Figure 6.7. Sky plot of PFISR beams and GPS PRN 18 & 22 & 27 location during 1300-1330 UT, March 17 2015.

Compared to event A3, there were only 4 beams operational during this event according to Figure 6.7. Table 6.3 summarizes and compares errors of SAGA estimates for this event. Note although PRN 22 gives no estimates after eliminating

those not satisfying the conditions on v_c, but is also the furthermost satellite from any of the beams, similar to PRN 10 from event A3. The measurements made by SAGA using PRNs 27 and 18 are not collocated with each other either. Despite these factors, there is a consistency between the two sets of estimates.

Table 6.3. ϵ_{sn} with $0 < v_c < v, v_c \in \mathbb{R}$, compared to 66 ° N, for event C1.

PRN	# good	# estimation	ϵ_v[%]	ϵ_θ[%]
27	3	16	17.677	8.3553
22	0	16	NaN	NaN
18	3	15	38.64	9.3356

6.4 Summary

This section presents two multi-instrument studies of the ionosphere. Using two case studies of multi-satellite scintillation events on geomagnetic active days in 2013 and 2015, SAGA drift estimates and their uncertainties are then evaluated with all sky imager data and compared to existing ion drift measurements from PFISR. The similarity in results of the two events are also discussed.

CHAPTER 7

CONCLUSION

This dissertation has presented an automated and systematic data collection, processing, analysis methods for studying the spatial-temporal properties of Global Navigation Satellite Systems (GNSS) scintillations produced by F-region ionospheric irregularities at high latitudes using a closely spaced multi-receiver array deployed in the northern auroral zone. This research demonstrated the use of a distributed GNSS scintillation receiver array as a single sensing instrument to measure the auroral zone drift and correlation ellipse parameters during periods of scintillation. The main contributions include 1) automated scintillation monitoring, 2) estimation of drift and anisotropy of the ground diffraction pattern irregularities, 3) error analysis of ionospheric estimates, 4) multi-instrument study of the ionosphere.

7.1 Summary and Discussions

Chapter 3 developed an automated detection routine as a statistical approach for long term scintillation monitoring. Two scintillation statistics surveys had been conducted respectively for auroral and equatorial regions. For the high-latitude survey, it was found that there is no strong evidence of seasonal dependence of scintillation. Elevated phase scintillation were observed mostly during night time when northern lights are seen. For the low-latitude survey, recurring amplitude scintillation events had been identified during night time when equatorial bubbles develop. The two surveys are helpful for verifying correlation between daily scintillation pattern and irregularities.

A two-stage scintillation detection routine was proposed. Days in question with elevated phase variation were selected by evaluating a single day metric. For each

day of interest, an algorithm was then established to determine potential scintillation events common to each operational receiver for each visible satellites after screening of low-rate scintillation phase indices. The developed routine demonstrates the ability to monitor and even forecast scintillation long term.

Chapter 4 applied a variation of the spaced-receiver technique to processed inter-receiver high-rate GPS phase measurements during select events. The diffraction pattern was solved to estimate drift velocity and anisotropy in shape of ionospheric irregularities. A sensitivity study followed to examine the impact of cross-correlation parameters on velocity estimates. A table of the estimated quantities for the top 20 most significant days of scintillation was provided. Overall results indicate that spaced receiver technique works well with the recently introduced GPS receivers and show the possibility of routinely quantifying ionospheric irregularities by drifts and anisotropy. The SAGA data have the potential to provide an unprecedented high-resolution view of the effects of auroral processes on GPS phase measurements.

Chapter 5 proposed an error analysis of SAGA estimates that can be applied on a routine basis. Using one sub-minute case study as demonstration of the implementation of the array data, estimates of the uncertainty were generated through Monte Carlo simulation on both drifts and anisotropy. This method should be considered as conservative since the errors were added onto post-processed filtered signals, from which most of the errors or biases are already eliminated. Two case studies both showed that the normalized variations of these estimates are small averaged over the whole event periods. In practice, noises in high-rate power/phase measurements are carried over to correlation time delays. Quantization errors are also introduced and propagated to observations due to the nature of the spaced-receiver method. Errors are then transmitted over to parameters that quantify drift velocities and anisotropy ellipses.

Chapter 6 further evaluated the SAGA drift estimates by comparing to horizontal speeds computed from PFISR measurements during 2 multi-satellite scintillation events. Corresponding auroral events recorded from the all sky imager had also been studied. For the two case studies, power fluctuations were simultaneously occurring with the phase fluctuations. All of the events lasted for about 30 minutes, apparently collocated with an auroral arc. Although the measurement methods for PFISR and SAGA differ in signal frequency and sensing geometry, a good agreement was found between the instruments' drift estimates after eliminating cases for which the characteristic velocity was estimated to be imaginary or larger than the drift speed of the irregularities. SAGA uncertainties were generally comparable to PFISR uncertainties in magnitude. PFISR and SAGA sampled different locations in the ionosphere. Nonetheless, the SAGA drift directions were within 20% and speeds within 25% of PFISR's. It was also observed that in both multi-satellite cases, the transmitting satellite at highest elevation gave the best estimates and was the nearest to but not collocated with the anti-field-aligned PFISR beam. Satellites that were further away from any of the PFISR beams tended to give worse estimates. This effort indicated that a kilometer-spaced GNSS receiver array collecting phase data can be used for investigating ionospheric dynamics.

7.2 Future Work

7.2.1 Further study of the ionosphere. Inter-comparisons of precise TEC from a closely spaced array has not been undertaken but precise estimation of TEC, possibly using geodetic algorithms, may be used to compare to the scintillation drift and anisotropy properties. Not only can high-resolution power and phase data be used in space-receiver technique, but also in spectral analysis based on inverse scatter theory for estimating other ionospheric properties such as thickness, top height, spectral

index and eventually electron density estimates[10, 59].

7.2.2 Multi-latitude application. While the research focus of this dissertation has been on the auroral zone, future ionospheric investigations with GNSS arrays could be conducted at lower latitudes.

7.2.3 Multi-instrumental observation. On the other hand, while SAGA can measure axial ratio and correlation ellipse orientation in addition to drift speeds, PFISR measures other ionospheric features such as electron densities and temperatures. The distributed GNSS receiver array can be used in coordination with incoherent scatter radar (ISR) data and optical imaging for multi-instrument studies of ionospheric phenomena. Since a GNSS spaced array is sensitive to the horizontal motion, rather than the line-of-sight motion (as in an ISR), it may also serve as a supplement to ISR data in directions of reduced observability or sensitivity. Alternatively, in areas where siting or powering equipment such as ISR is not feasible, a GNSS scintillation array may be a relatively inexpensive alternative. For this type of application software receivers can be particularly convenient, and the wider availability of software radios has enabled the proliferation of receivers with scintillation monitoring capabilities.

7.2.4 Multi-frequency estimation. The analysis shown in this work was carried out for GPS L1 frequency, the technique should be applicable to other GNSS frequencies and other GNSS constellations as well. Inter-receiver comparisons for each frequency would increase redundancy in the estimation process. [60] show that, in equatorial regions, L2C and L5 are more susceptible to scintillation. For a receiver able to track through these instances of scintillation, there would possibly be more events with which to apply the spaced receiver measurement method. However, at present any greater susceptibility of L2C and L5 is countered by the fact that fewer satellites broadcast at those frequencies than at L1. [18] show that in the auroral

zone, L2 is much more susceptible than L1, due to the semi-codeless tracking of the P(Y) code. The spaced-receiver technique is not applicable for inter-frequency correlations since different wavelengths will undergo different scattering through the ionosphere, which tends to result in non-simultaneous scintillation on the different frequencies [61]. This property is expected to be helpful in a scintillation array since additional estimates may be made possible by the additional frequencies. Likewise, multi-constellation GNSS provides broader coverage of the sky, so estimates of drift and anisotropy may be made for different, and possibly multiple, regions of the sky.

APPENDIX A

DERIVATION OF SATELLITE MOTION

Since the receivers in the SAGA array are not geostationary, the motion of the signals (satellites) also contribute to the drift motion of the diffraction pattern, as shown in Figure A.1 Their relationship is given by:

$$\mathbf{{}^{d}V^{g}} = \mathbf{{}^{d}V^{ipp}} + \mathbf{{}^{ipp}V^{g}} \tag{A.1}$$

where

- $\mathbf{{}^{ipp}V^{g}}$: the satellite or signal motion measured at the ionospheric pierce point (IPP) with respect to the ground.
- $\mathbf{{}^{d}V^{g}}$: drift velocity of the diffraction pattern with respect to the ground.
- $\mathbf{{}^{d}V^{ipp}}$: drift velocity of the diffraction pattern with respect to the IPP frame where the signal/satellite has zero motion.

To compute the satellite motion relative to the ground, one must first obtain the location of the ionospheric pierce point (IPP) of the GNSS satellite signal, as shown in Figure A.1. The latitude and longitude $\lambda_{ipp}, \phi_{ipp}$ of the IPP can be calculated given the azimuth, elevation angles of the satellite, the geodetic location of a geostationary reference point usually on the ground and an assumed shell height, the altitude of the IPP z. The geodetic coordinates $[\lambda, \phi, z]_{ipp}$ are then converted to position ${}^{ipp}\vec{\mathbf{r}}$ with respect to a point on the ground with local east-north-up coordinates, which is normally a two-stage process: first from geodetic to Earth-Centered, Earth-Fixed (ECEF), then from ECEF to local:

$$\begin{bmatrix} r_e \\ r_n \\ r_u \end{bmatrix} = {}^{l}\mathbf{R}^{e}\ {}^{e}\mathbf{R}^{g} \begin{bmatrix} \lambda \\ \phi \\ z \end{bmatrix}_{ipp} \tag{A.2}$$

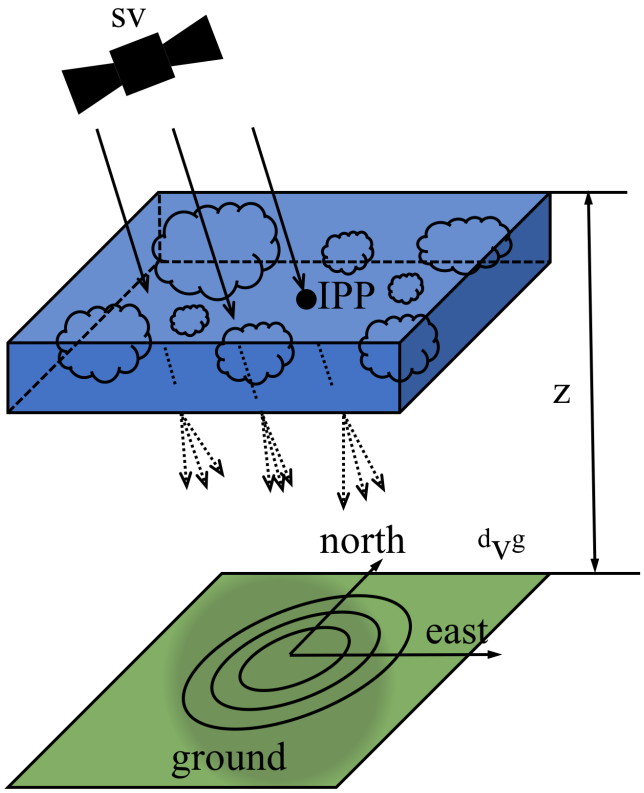

Figure A.1. Satellite motion related to the ground measured at the ionospheric pierce point (IPP) also contributes to the irregularity drift of the ground pattern.

Finite differencing the horizontal components of the position vector as seen from the ground frame g gives horizontal IPP velocities relative to the ground ${}^{ipp}v_e^g, {}^{ipp}v_n^g$:

$$ {}^{ipp}\vec{\mathbf{v}}^g = \dot{\vec{\mathbf{r}}}^g = \frac{\vec{\mathbf{r}}(t+\Delta t) - \vec{\mathbf{r}}(t)}{\Delta t} \tag{A.3} $$

Considering the satellite motion is usually small compared to irregularity drifts (${}^{ipp}\vec{\mathbf{v}}^g \approx 50 - 100$ m/s), this paper evaluates IPP velocity estimates and their uncertainties by taking average and one-sigma over a certain estimation period. For more accurate error estimation that is beyond the scope of this dissertation, one might estimate the IPP altitude separately using spectral methods [59, 10] or assume it to be randomly distributed, e.g. $z_{ipp} \sim \mathcal{N}(\bar{z}, \sigma_z^2)$, and then propagate that to the error in satellite motion.

BIBLIOGRAPHY

[1] P. M. Kintner, B. M. Ledvina, and E. R. de Paula, "Gps and ionospheric scintillations," *Space Weather*, vol. 5, no. 9, pp. n/a–n/a, 2007, s09003. [Online]. Available: http://dx.doi.org/10.1029/2006SW000260

[2] P. M. Kintner, B. M. Ledvina, E. R. de Paula, and I. J. Kantor, "Size, shape, orientation, speed, and duration of gps equatorial anomaly scintillations," *Radio Science*, vol. 39, no. 2, pp. n/a–n/a, 2004, rS2012. [Online]. Available: http://dx.doi.org/10.1029/2003RS002878

[3] A. M. Smith, C. N. Mitchell, R. J. Watson, R. W. Meggs, P. M. Kintner, K. Kauristie, and F. Honary, "Gps scintillation in the high arctic associated with an auroral arc," *Space Weather*, vol. 6, no. 3, pp. n/a–n/a, 2008, s03D01. [Online]. Available: http://dx.doi.org/10.1029/2007SW000349

[4] J. Aarons, "Global positioning system phase fluctuations at auroral latitudes," *Journal of Geophysical Research: Space Physics*, vol. 102, no. A8, pp. 17 219–17 231, 1997. [Online]. Available: http://dx.doi.org/10.1029/97JA01118

[5] G. S. Bust, S. Datta-Barua, K. Deshpande, S. Bourand, S. Skone, and Y. Su, "Correlation properties of a 2-d array of high latitude scintillation receivers," in *Proceedings of the 26th International Technical Meeting of The Satellite Division of the Institute of Navigation (ION GNSS+ 2013), Nashville, TN*, Sep. 2013, pp. 2470–2479.

[6] M. A. Kelly, J. M. Comberiate, E. S. Miller, and L. J. Paxton, "Progress toward forecasting of space weather effects on uhf satcom after operation anaconda," *Space Weather*, vol. 12, no. 10, pp. 601–611, 2014, 2014SW001081. [Online]. Available: http://dx.doi.org/10.1002/2014SW001081

[7] M. Zettergren, K. Lynch, D. Hampton, M. Nicolls, B. Wright, M. Conde, J. Moen, M. Lessard, R. Miceli, and S. Powell, "Auroral ionospheric f region density cavity formation and evolution: Mica campaign results," *Journal of Geophysical Research: Space Physics*, vol. 119, no. 4, pp. 3162–3178, 2014. [Online]. Available: http://dx.doi.org/10.1002/2013JA019583

[8] C. J. Heinselman and M. J. Nicolls, "A bayesian approach to electric field and e-region neutral wind estimation with the poker flat advanced modular incoherent scatter radar," *Radio Science*, vol. 43, no. 5, pp. n/a–n/a, 2008, rS5013. [Online]. Available: http://dx.doi.org/10.1029/2007RS003805

[9] M. Hernández-Pajares, J. M. Juan, J. Sanz, R. Orus, A. Garcia-Rigo, J. Feltens, A. Komjathy, S. C. Schaer, and A. Krankowski, "The igs vtec maps: a reliable source of ionospheric information since 1998," *Journal of Geodesy*, vol. 83, no. 3, pp. 263–275, 2009. [Online]. Available: http://dx.doi.org/10.1007/s00190-008-0266-1

[10] K. C. Yeh and C.-H. Liu, "Radio wave scintillations in the ionosphere," *Proceedings of the IEEE*, vol. 70, no. 4, pp. 324–360, April 1982.

[11] R. T. Tsunoda, "High-latitude f region irregularities: A review and synthesis," *Reviews of Geophysics*, vol. 26, no. 4, pp. 719–760, 1988. [Online]. Available: http://dx.doi.org/10.1029/RG026i004p00719

[12] J. Aarons, "Global morphology of ionospheric scintillations," *Proceedings of the IEEE*, vol. 70, no. 4, pp. 360–378, April 1982.

[13] X. Pi, A. J. Mannucci, U. J. Lindqwister, and C. M. Ho, "Monitoring of global ionospheric irregularities using the worldwide gps network," *Geophysical Research Letters*, vol. 24, no. 18, pp. 2283–2286, 1997. [Online]. Available: http://dx.doi.org/10.1029/97GL02273

[14] I. Cherniak, I. Zakharenkova, and A. Krankowski, "Approaches for modeling ionosphere irregularities based on the tec rate index," *Earth, Planets and Space*, vol. 66, no. 1, pp. 1–5, 2014. [Online]. Available: http://dx.doi.org/10.1186/s40623-014-0165-z

[15] S. Priyadarshi, "A review of ionospheric scintillation models," *Surveys in Geophysics*, vol. 36, no. 2, pp. 295–324, 2015. [Online]. Available: http://dx.doi.org/10.1007/s10712-015-9319-1

[16] S. Skone, K. Knudsen, and M. de Jong, "Limitations in {GPS} receiver tracking performance under ionospheric scintillation conditions," *Physics and Chemistry of the Earth, Part A: Solid Earth and Geodesy*, vol. 26, no. 68, pp. 613 – 621, 2001, proceedings of the First {COST} Action 716 Workshop Towards Operational {GPS} Meteorology and the Second Network Workshop of the International {GPS} Service (IGS). [Online]. Available: http://www.sciencedirect.com/science/article/pii/S1464189501001107

[17] J. Seo, T. Walter, T.-Y. Chiou, and P. Enge, "Characteristics of deep gps signal fading due to ionospheric scintillation for aviation receiver design," *Radio Science*, vol. 44, no. 1, pp. n/a–n/a, 2009, rS0A16. [Online]. Available: http://dx.doi.org/10.1029/2008RS004077

[18] Y. Jiao, Y. T. Morton, S. Taylor, and W. Pelgrum, "Characterization of high-latitude ionospheric scintillation of gps signals," *Radio Science*, vol. 48, no. 6, pp. 698–708, 2013, 2013RS005259. [Online]. Available: http://dx.doi.org/10.1002/2013RS005259

[19] P. Prikryl, P. T. Jayachandran, S. C. Mushini, and I. G. Richardson, "High-latitude GPS phase scintillation and cycle slips during high-speed solar wind streams and interplanetary coronal mass ejections: a superposed epoch analysis," *Earth, Planets, and Space*, vol. 66, p. 62, Dec. 2014.

[20] R. Ghoddousi-Fard, L. Nikitina, D. Danskin, P. Prikryl, and F. Lahaye, "Analysis of {GPS} phase rate variations in response to geomagnetic field perturbations over the canadian auroral region," *Advances in Space Research*, vol. 55, no. 5, pp. 1372 – 1381, 2015. [Online]. Available: http://www.sciencedirect.com/science/article/pii/S0273117714007972

[21] P. Prikryl, L. Spogli, P. T. Jayachandran, J. Kinrade, C. N. Mitchell, B. Ning, G. Li, P. J. Cilliers, M. Terkildsen, D. W. Danskin, E. Spanswick, E. Donovan, A. T. Weatherwax, W. A. Bristow, L. Alfonsi, G. De Franceschi, V. Romano, C. M. Ngwira, and B. D. L. Opperman, "Interhemispheric comparison of gps phase scintillation at high latitudes during the magnetic-cloud-induced geomagnetic storm of 57 april 2010," *Annales Geophysicae*, vol. 29, no. 12, pp. 2287–2304, 2011. [Online]. Available: http://www.ann-geophys.net/29/2287/2011/

[22] J. Kinrade, C. N. Mitchell, P. Yin, N. Smith, M. J. Jarvis, D. J. Maxfield, M. C. Rose, G. S. Bust, and A. T. Weatherwax, "Ionospheric scintillation over antarctica during the storm of 56 april 2010," *Journal of Geophysical Research: Space Physics*, vol. 117, no. A5, pp. n/a–n/a, 2012, a05304. [Online]. Available: http://dx.doi.org/10.1029/2011JA017073

[23] Y. Jin, J. I. Moen, and W. J. Miloch, "GPS scintillation effects associated with polar cap patches and substorm auroral activity: direct comparison," *Journal of Space Weather and Space Climate*, vol. 4, no. 27, p. A23, Aug. 2014.

[24] C. van der Meeren, K. Oksavik, D. Lorentzen, J. I. Moen, and V. Romano, "Gps scintillation and irregularities at the front of an ionization tongue in the nightside polar ionosphere," *Journal of Geophysical Research: Space Physics*, vol. 119, no. 10, pp. 8624–8636, 2014. [Online]. Available: http://dx.doi.org/10.1002/2014JA020114

[25] B. H. Briggs, G. J. Phillips, and D. H. Shinn, "The analysis of observations on spaced receivers of the fading of radio signals," *Proceedings of the Physical Society. Section B*, vol. 63, no. 2, p. 106, 1950. [Online]. Available: http://stacks.iop.org/0370-1301/63/i=2/a=305

[26] R. C. Livingston, C. L. Rino, J. Owen, and R. T. Tsunoda, "The anisotropy of high-latitude nighttime f region irregularities," *Journal of Geophysical Research: Space Physics*, vol. 87, no. A12, pp. 10 519–10 526, 1982. [Online]. Available: http://dx.doi.org/10.1029/JA087iA12p10519

[27] C. L. Rino, R. C. Livingston, R. T. Tsunoda, R. M. Robinson, J. F. Vickrey, C. Senior, M. D. Cousins, J. Owen, and J. A. Klobuchar, "Recent studies of the structure and morphology of auroral zone f region irregularities," *Radio Science*, vol. 18, no. 6, pp. 1167–1180, 1983. [Online]. Available: http://dx.doi.org/10.1029/RS018i006p01167

[28] J. W. Armstrong and W. A. Coles, "Analysis of three-station interplanetary scintillation," *Journal of Geophysical Research*, vol. 77, no. 25, pp. 4602–4610, 1972. [Online]. Available: http://dx.doi.org/10.1029/JA077i025p04602

[29] E. Costa, P. F. Fougere, and S. Basu, "Cross-correlation analysis and interpretation of spaced-receiver measurements," *Radio Science*, vol. 23, no. 2, pp. 141–162, 1988. [Online]. Available: http://dx.doi.org/10.1029/RS023i002p00141

[30] L. S. Fedor, "A statistical approach to the determination of three-dimensional ionospheric drifts," *Journal of Geophysical Research*, vol. 72, no. 21, pp. 5401–5415, 1967. [Online]. Available: http://dx.doi.org/10.1029/JZ072i021p05401

[31] S. Basu, S. Basu, E. Costa, C. Bryant, C. E. Valladares, and R. C. Livingston, "Interplanetary magnetic field control of drifts and anisotropy of high-latitude irregularities," *Radio Science*, vol. 26, no. 4, pp. 1079–1103, 1991. [Online]. Available: http://dx.doi.org/10.1029/91RS00586

[32] S. Basu, E. Costa, R. C. Livingston, K. M. Groves, H. C. Carlson, P. K. Chaturvedi, and P. Stubbe, "Evolution of subkilometer scale ionospheric irregularities generated by high-power hf waves," *Journal of Geophysical Research: Space Physics*, vol. 102, no. A4, pp. 7469–7475, 1997. [Online]. Available: http://dx.doi.org/10.1029/96JA03340

[33] G. Zhang, R. J. Doviak, J. Vivekanandan, W. O. J. Brown, and S. A. Cohn, "Cross-correlation ratio method to estimate cross-beam wind and comparison with a full correlation analysis," *Radio Science*, vol. 38, no. 3, pp. n/a–n/a, 2003, 8052. [Online]. Available: http://dx.doi.org/10.1029/2002RS002682

[34] R. J. Doviak, G. Zhang, S. A. Cohn, and W. O. J. Brown, "Comparison of spaced-antenna baseline wind estimators: Theoretical and simulated results," *Radio Science*, vol. 39, no. 1, pp. n/a–n/a, 2004, rS1006. [Online]. Available: http://dx.doi.org/10.1029/2003RS002931

[35] J. Wang and Y. J. Morton, "Spaced receiver array for ionospheric irregularity drift velocity estimation using multi-band gnss signals," in *Proceedings of the 28th International Technical Meeting of The Satellite Division of the Institute of Navigation (ION GNSS+ 2015), Tampa, Florida*, Sep. 2015, pp. 3449–3458.

[36] E. Costa, S. Basu, and S. Basu, "Application of three cross-correlation techniques to spaced-receiver data," *Journal of Atmospheric and Terrestrial Physics*, vol. 54, no. 10, pp. 1257 – 1263, 1992, wave and turbulence analysis techniques. [Online]. Available: http://www.sciencedirect.com/science/article/pii/002191699290034I

[37] N. R. Council, *Plasma Physics of the Local Cosmos*. Washington, DC: The National Academies Press, 2004. [Online]. Available: https://www.nap.edu/catalog/10993/plasma-physics-of-the-local-cosmos

[38] Windows to the Universe. (2010, dec) Basic Facts About Ionospheric Scintillations. [Online]. Available: https://www.windows2universe.org/spaceweather/scintillations_facts.html

[39] State of New South Wales, Department of Education and Training. (2008, dec) The Earths magnetic field. [Online]. Available: http://lrrpublic.cli.det.nsw.edu.au/lrrSecure/Sites/Web/Forces_and_fields_creative_commons/7306/other/earths_magnetic_field.htm

[40] Ian Tresman. (2007, dec) Charged particle drifts in a homogeneous magnetic field. [Online]. Available: https://commons.wikimedia.org/wiki/File%3ACharged-particle-drifts.svg

[41] Space Weather Prediction Center. (2013, dec) Kp index. [Online]. Available: ftp://ftp.swpc.noaa.gov/pub/warehouse/2013/2013_plots/kp/

[42] World Data Center for Geomagnetism, Kyoto. (2016, mar) Provisional (Quicklook) AE index. [Online]. Available: KyotoUniv.,Kyoto,Japan.[Availableathttp://wdc.kugi.kyoto-u.ac.jp/ae_provisional/index.html,accessed28Feb2016]

[43] Jicamarca Radio Observatory. (2016) ESF. [Online]. Available: http://jro-db.igp.gob.pe/

[44] SRI International ISR Database. (2013) Beam PLot. [Online]. Available: http://amisr.com/database/dbase_site_media/PFISR/ExperimentTypes/PINOT_Daytime31/PINOT_Daytime31.jpg

[45] T. Humphreys, M. Psiaki, B. Ledvina, A. Cerruti, and P. Kintner, "Data-driven testbed for evaluating gps carrier tracking loops in ionospheric scintillation," *Aerospace and Electronic Systems, IEEE Transactions on*, vol. 46, no. 4, pp. 1609–1623, Oct 2010.

[46] G. Crowley, G. S. Bust, A. Reynolds, I. Azeem, R. Wilder, B. W. O'Hanlon, M. L. Psiaki, S. Powell, T. E. Humphreyes, and J. A. Bhatti, "Cases: A novel low-cost ground-based dual-frequency gps software receiver and space weather monitor," in *Proceedings of the 24th International Technical Meeting of The Satellite Division of the Institute of Navigation (ION GNSS 2011)*, 2011, pp. 1437–1446.

[47] A. J. Van Dierendonck and Q. Hua, "Measuring ionospheric scintillation effects from gps signals," in *Proceedings of the 57th Annual Meeting of The Institute of Navigation (2001)*, 2001, pp. 391–396.

[48] A. Van Dierendonck, J. Klobuchar, and Q. Hua, "Ionospheric scintillation monitoring using commercial single frequency c/a code receivers," in *Proceedings of the 6th International Technical Meeting of the Satellite Division of The Institute of Navigation (ION GPS 1993)*, 1993, pp. 1333–1342.

[49] K. B. Deshpande, G. S. Bust, C. R. Clauer, H. Kim, J. E. Macon, T. E. Humphreys, J. A. Bhatti, S. B. Musko, G. Crowley, and A. T. Weatherwax, "Initial gps scintillation results from cases receiver at south pole, antarctica," *Radio Science*, vol. 47, no. 5, pp. n/a–n/a, 2012, rS5009. [Online]. Available: http://dx.doi.org/10.1029/2012RS005061

[50] X. Li, M. Ge, H. Zhang, and J. Wickert, "A method for improving uncalibrated phase delay estimation and ambiguity-fixing in real-time precise point positioning," *Journal of Geodesy*, vol. 87, no. 5, pp. 405–416, 2013. [Online]. Available: http://dx.doi.org/10.1007/s00190-013-0611-x

[51] Space Weather Prediction Center, "SWPC PRF 1997 09 December 2013," ftp.swpc.noaa.gov/warehouse/2013/WeeklyPDF/prf1997.pdf, dec 2013.

[52] ——, "SWPC PRF 2008 24 Feburary 2014," ftp.swpc.noaa.gov/warehouse/2014/WeeklyPDF/prf2008.pdf, feb 2014.

[53] ——, "SWPC PRF 2064 23 March 2015," ftp.swpc.noaa.gov/warehouse/2015/WeeklyPDF/prf2064.pdf, mar 2015.

[54] E. Costa, S. Basu, R. C. Livingston, and P. Stubbe, "Multiple baseline measurements of ionospheric scintillation induced by high-power hf waves," *Radio Science*, vol. 32, no. 1, pp. 191–197, 1997. [Online]. Available: http://dx.doi.org/10.1029/96RS02027

[55] G. Kent and J. Koster, "Some studies of nighttime f-layer irregularities at the equator using very- high-frequency signals radiated from earth satellites." *Ann. Geophys., 22: 405-17(July-Sept. 1966).*, Jan 1966.

[56] P. May, "Statistical errors in the determination of wind velocities by the spaced antenna technique," *Journal of Atmospheric and Terrestrial Physics*, vol. 50, no. 1, pp. 21 – 32, 1988. [Online]. Available: http://www.sciencedirect.com/science/article/pii/0021916988900049

[57] S. Datta-Barua, Y. Su, K. Deshpande, D. Miladinovich, G. S. Bust, D. Hampton, and G. Crowley, "First light from a kilometer-baseline scintillation auroral gps array," *Geophysical Research Letters*, vol. 42, no. 10, pp. 3639–3646, 2015, 2015GL063556. [Online]. Available: http://dx.doi.org/10.1002/2015GL063556

[58] K. O. Arras, "An introduction to error propagation: Derivation, meaning and examples of equation $C_Y = F_X C_X F_X^T$," Swiss Federal Institute of Technology Lausanne (EPFL), Tech. Rep., 1998.

[59] L. S. Taylor, "Effects of layered turbulence on oblique waves," *Radio Science*, vol. 10, no. 1, pp. 121–128, 1975. [Online]. Available: http://dx.doi.org/10.1029/RS010i001p00121

[60] E. R. de Paula, O. F. Jonah, A. O. Moraes, E. A. Kherani, B. G. Fejer, M. A. Abdu, M. T. A. H. Muella, I. S. Batista, S. L. G. Dutra, and R. R. Paes, "Low-latitude scintillation weakening during sudden stratospheric warming events," *Journal of Geophysical Research: Space Physics*, vol. 120, no. 3, pp. 2212–2221, 2015, 2014JA020731. [Online]. Available: http://dx.doi.org/10.1002/2014JA020731

[61] J. Seo and T. Walter, "Future dual-frequency gps navigation system for intelligent air transportation under strong ionospheric scintillation," *IEEE Transactions on Intelligent Transportation Systems*, vol. 15, no. 5, pp. 2224–2236, Oct 2014.